

1 **An empirical algorithm to map perennial firn aquifers ~~and~~, ice ~~slabs~~, ~~and~~**  
2 **~~perched firn aquifers~~ within the Greenland Ice Sheet**  
3 **using satellite L-band microwave radiometry**  
4  
5  
6

7 Julie Z. Miller<sup>1,2</sup>, Riley Culberg<sup>3</sup>, David G. Long<sup>4</sup>, Christopher A. Shuman<sup>5</sup>,

8 ~~Dustin M. Schroeder~~<sup>3,6,7</sup>, Mary J. Brodzik<sup>1,7</sup>  
9

10  
11  
12 <sup>1</sup>Cooperative Institute for Research in Environmental Sciences, University of Colorado, Boulder, Colorado, USA

13 <sup>2</sup>Earth Science and Observation Center, University of Colorado, Boulder, Colorado, USA

14 <sup>3</sup>Department of Electrical Engineering, Stanford University, Stanford, California, USA

15 <sup>4</sup>Department of Electrical and Computer Engineering, Brigham Young University, Provo, Utah, USA

16 <sup>5</sup>University of Maryland, Baltimore County, Joint Center for Earth Systems Technology at Code 615,

17 Cryospheric Sciences Laboratory NASA Goddard Space Flight Center, Greenbelt, Maryland, USA

18 <sup>6</sup>Department of Geophysics, Stanford University, Stanford, CA, USA

19 <sup>7</sup>National Snow and Ice Data Center, University of Colorado, Boulder, Colorado, USA

20 Correspondence to: jzmiller.research@gmail.com

21 **Abstract**

22 Perennial firn aquifers are subsurface meltwater reservoirs ~~consisting of a meters-thick~~~~formed from~~  
23 ~~a water-saturated firn layer~~ ~~that can form on spatial scales as large as tens of kilometers~~. They have  
24 been observed within the percolation facies of glaciated regions experiencing intense seasonal  
25 surface melting and high snow accumulation. Widespread perennial firn aquifers have been  
26 identified within the Greenland Ice Sheet (GrIS) via field expeditions, airborne ice-penetrating radar  
27 surveys, and satellite microwave sensors. In contrast, ice slabs are nearly-continuous ice layers  
28 that ~~can also~~ form on spatial scales ~~as large as tens~~ of kilometers as a result of surface and  
29 subsurface water-saturated snow and firn layers sequentially refreezing following multiple melting  
30 seasons. They have been observed within the percolation facies of glaciated regions experiencing  
31 intense seasonal surface melting, but in areas where snow accumulation is at least ~25% lower as  
32 compared to perennial firn aquifer areas. Widespread ice slabs have recently been identified within  
33 the GrIS via field expeditions and airborne ice-penetrating radar surveys, specifically in areas where  
34 perennial firn aquifers typically do not form. However, ice slabs have yet to be ~~inferred-identified~~  
35 from space. Together, these two ice sheet features represent distinct, but related, sub-facies within  
36 the broader percolation facies of the GrIS that can be defined primarily by differences in snow  
37 accumulation, which influences the englacial hydrology and thermal characteristics of firn layers  
38 at depth.

39 Here, for the first time, we ~~use~~ ~~use~~-enhanced-resolution vertically-polarized L-band  
40 brightness temperature ( $T_V^{\text{p}}$ ) imagery (2015-2019) generated using observations collected over the  
41 GrIS by NASA's Soil Moisture Active Passive (SMAP) satellite to map ~~both~~ perennial firn aquifer and

ice slab areas ~~together~~ as a continuous ~~englacial hydrological~~ system over the percolation facies. We also map 'perched' firn aquifer areas, which we define as areas where shallow water-saturated firn layers transiently form on top of buried ice slabs, or other semi-impermeable layers within the snow and firn. We use an empirical algorithm previously developed to map the extent of Greenland's perennial firn aquifers via fitting exponentially decreasing temporal L-band signatures to a set of sigmoidal curves. ~~This~~ ~~is~~ ~~algorithm~~ ~~is~~ recalibrated to also map the extent of ice slab and perched firn aquifer areas using airborne ice-penetrating radar surveys collected by NASA's Operation Ice Bridge (OIB) campaigns (2010-2017). Our SMAP-derived maps show that between 2015 and 2019, perennial firn aquifer areas extended over 6464,000 km<sup>2</sup>, and ice slab areas extended over 76,000 km<sup>2</sup>, and perched firn aquifer areas extended over 37,000 km<sup>2</sup>. Combined together, these ~~three~~ sub-facies are the equivalent of 2424% of the percolation facies of the GrIS. As Greenland's climate continues to warm, and seasonal surface melting will increase in extent, intensity, and duration, Quantifying the possible rapid expansion of each of these sub-facies using current and forthcoming satellite L-band microwave radiometry and synthetic aperture radar missions has significant implications for understanding ice sheet-wide variability in englacial firn hydrology resulting in meltwater-induced hydrofracturing and accelerated ice flow as well as high-elevation meltwater run-off that can impact the mass balance and stability of the GrIS.

## 1 Introduction

The recent launches of several satellite L-band microwave radiometry missions by NASA (Aquarius mission, Levine, et al., 2007; Soil Moisture Active Passive (SMAP) mission, Entekhabi et al., 2010) and ESA (Soil Moisture and Ocean Salinity (SMOS), Kerr et al., 2010) have provided a new Earth-observation tool capable of detecting stored meltwater storage approximately tens of meters to kilometers beneath the surface of ice sheets ice sheet surface. Jezek et al. (2015) recently demonstrated that in the high-elevation (~3500 m a.s.l.) dry snow facies of the Antarctic Ice Sheet, meltwater stored in subglacial Lake Vostok can be detected as deep as ~4000-4 km beneath the ice sheet surface. Subglacial lakes represent radiometrically cold subsurface meltwater reservoirs. Upwelling L-band emissions from the radiometrically warm bedrock underlying the subglacial lakes are effectively blocked by high reflectivity and attenuation at the interface between the bedrock and the overlying lake bottom. This results in a lower observed microwave brightness temperature ( $T^B$ ) at the ice sheet surface as compared to other dry snow facies areas where bedrock contributes to L-band emission depth-integrated over the entire ice sheet thickness.

Similar to subglacial lakes, perennial firn aquifers also represent radiometrically cold subsurface meltwater reservoirs (Miller et al., 2020) consisting of a 4-25 m thick water-saturated firn layer (Koenig et al., 2014; Montgomery et al., 2017; Chu et al., 2018) that can form on spatial scales as large as tens of kilometers (Forster et al., 2014). Perennial firn aquifers formed from a 4 m-25 m thick water-saturated firn

Formatted: Not Highlight

78 layer (Koenig et al., 2014; Montgomery et al., 2017; Chu et al., 2018). They have been ~~observed-identified~~  
79 ~~via field expeditions~~ (Forster et al., 2014), ~~airborne ice-penetrating radar surveys~~ (Miège et al., 2016), and  
80 ~~satellite microwave sensors~~ (Brangers et al., 2020; Miller et al., 2020) ~~via field expeditions and airborne ice-~~  
81 ~~penetrating radar surveys~~ in the lower-elevation (< -2000 m<sub>a.s.l.</sub>) percolation facies of the Greenland Ice  
82 Sheet (GIS) ~~at depths from between -1 m and 40 m beneath the ice sheet surface.~~ ~~They exist in areas~~  
83 ~~that experience intense seasonal surface melting and rain (> -650 mm w.e. yr<sup>-1</sup>) during the melting season~~  
84 ~~and high snow accumulation (> -800 mm w.e. yr<sup>-1</sup>) during the freezing season~~ (Forster et al., 2014), ~~at~~  
85 ~~depths from between -1 m and 40 m beneath the ice sheet surface~~ (Miège et al., 2016), ~~and in areas that~~  
86 ~~experience intense seasonal surface melting (>650 mm yr<sup>-1</sup>) during the melting season and high snow~~  
87 ~~accumulation (>800 mm yr<sup>-1</sup>) during the freezing season~~ (Forster et al., 2014). High snow accumulation in  
88 perennial firn aquifer areas thermally insulates water-saturated firn layers from the cold atmosphere  
89 allowing seasonal meltwater to be stored in liquid form year-round if the overlying seasonal snow layer is  
90 sufficiently thick (Kuipers Munneke et al., 2014). Koenig et al. (2014) estimated that the volumetric fraction  
91 of meltwater stored within the pore space of Greenland's perennial firn aquifers just prior to melt onset  
92 ranges from between -10% and 25%, which limits the upward propagation of electromagnetic energy from  
93 greater depths within the ice sheet. Large volumetric fractions of meltwater within the firn pore space results  
94 in high reflectivity and attenuation at the interface between water-saturated firn layers and the overlying  
95 refrozen firn layers, and between glacial ice or an n semi-impermeable layer and the overlying water-  
96 saturated firn layers. Upwelling L-band emission s-from deeper glacial ice and the underlying bedrock are  
97 is effectively blocked.

98 While perennial firn aquifers are radiometrically cold, the slow refreezing of deeper firn layers  
99 saturated with large volumetric fractions of meltwater represents a significant source of latent heat that is  
100 continuously released throughout the freezing season. Refreezing of seasonal meltwater by the descending  
101 winter cold wave (Pfeffer et al., 1991), and the subsequent formation of embedded ice structures (i.e.,  
102 horizontally-oriented ice layers and ice lenses, and vertically-oriented ice pipes; Benson et al., 1960;  
103 Humphrey et al., 2012; Harper et al., 2012) within the upper snow and firn layers represents a secondary  
104 source of latent heat. These heat sources help maintain meltwater at depth. Perennial firn aquifer areas  
105 are radiometrically warmer than other percolation facies areas where the single source of latent heat is via  
106 refreezing of seasonal meltwater. This results in a higher observed  $T^B$  at the ice sheet surface during the  
107 freezing season as compared to other percolation facies areas where seasonal meltwater is fully refrozen  
108 and stored exclusively as embedded ice.

109 ~~Many open questions remain about Greenland's perennial firn aquifers, regarding initial~~  
110 ~~formation, extent, depth, flow characteristics, timescale of refreezing and/or englacial drainage, and~~  
111 ~~connections to the subglacial hydrological system. Seasonal surface melting over the GIS has increased~~  
112 ~~in extent, intensity, and duration since the beginning of the satellite era~~ (Steffen et al., 2004; Tedesco et al.,  
113 2008; Tedesco et al., 2011; Nghiem et al., 2012; Tedesco et al., 2016; Tedesco and Fettweis, 2020;  
114 Cullather et al., 2020). If this trend continues (Franco et al., 2013; Noël et al., 2021), subsequent increases

115 in the volume of meltwater stored within Greenland's perennial firn aquifers will increase the possibility of  
116 crevasse deepening via meltwater-induced hydrofracturing (Alley et al., 2005; van der Veen, 2007),  
117 especially if crevasse fields laterally expand into perennial firn aquifer areas as a result of accelerated ice  
118 flow (Colgan et al., 2016). Meltwater induced hydrofracturing is an important component of supraglacial  
119 lake drainage during the melting season (Das et al., 2009; Stevens et al., 2015) leading to at least temporary  
120 accelerated flow velocities (Zwally et al., 2002; Joughin et al., 2013; Moon et al., 2014) and mass balance  
121 changes (Joughin et al., 2008). Greenland's firn perennial aquifers may also support meltwater-induced  
122 hydrofracturing, even during the freezing season (Poinar et al., 2017; 2019).

123 [Recently, mapping the extent of Greenland's perennial firn aquifers from space was demonstrated using](#)  
124 [satellite L-band microwave radiometry \(Miller et al., 2020\). Exponentially decreasing temporal L-band](#)  
125 [signatures observed in enhanced-resolution vertically-polarized L-band brightness temperature \( \$T^B\$ \)](#)  
126 [imagery \(2015-2016\) generated using observations collected over the GrIS by the microwave radiometer](#)  
127 [on NASA's SMAP satellite \(Long et al., 2019\) were correlated with a single year of perennial firn aquifer](#)  
128 [detections \(Miège et al. 2016\). These detections were](#) identified via the Center for Remote Sensing of Ice  
129 Sheets (CRE SIS) Multi-Channel Coherent Radar Depth Sounder (MCoRDS) flown by NASA's Operation  
130 Ice Bridge (OIB) campaigns (Miège et al. 2016; Rodriguez-Morales et al, 2014). An empirical algorithm to  
131 map extent was developed by fitting temporal L-band signatures to a set of sigmoidal curves derived from  
132 the continuous logistic model.

133 The relationship between the radiometric, and thus the physical, temperature of perennial firn  
134 aquifer areas, as compared to other percolation facies areas, forms the basis of the empirical algorithm.  
135 Miller et al. (2020) hypothesized that the dominant control on the relatively slow exponential rate of  $T^B$   
136 decrease over perennial firn aquifer areas is physical temperature versus depth. L-band emissions from  
137 the radiometrically warm upper snow and firn layers decrease during the freezing season as embedded  
138 ice structures slowly refreeze at increased depths below the ice sheet surface. In the percolation facies,  
139 refreezing of seasonal meltwater results in the formation of an intricate network of embedded ice structures  
140 that are large (1-40-100 cm long, ~10-20 cm wide; Jezek et al., 1994) relative to the L-band wavelength  
141 (~21 cm). Embedded ice structures induce strong volume scattering (Rignot et al., 1993; Rignot 1995) that  
142 decreases  $T^B$  (Zwally, 1977; Swift et al. 1985; Jezek et al., 2018).

143  
144 Ice slabs are ~1-16 m thick nearly-continuous ice layers that [that can form on spatial scales as](#)  
145 [large as tens of kilometers form on spatial scales of kilometers](#) as a result of surface and subsurface water-  
146 saturated snow and firn layers sequentially refreezing following multiple melting seasons (Machguth et al.,  
147 2016; [MacFerrinMacFerrin](#) et al., 2019). Over time, they become dense low-permeability solid-ice layers  
148 overlying deeper permeable firn layers. [Similar to perennial firn aquifers, ice slabs ice slabs](#) have been  
149 [observed-identified](#) via field expeditions and [airborne ice-penetrating radar surveys ice-penetrating airborne](#)  
150 [radar surveys](#) in the lower-elevation (<-2000 m.a.s.l.) percolation facies of the GrIS. [They form](#) at depths  
151 from between ~1-20 m and 20 m beneath the ice sheet surface ([MacFerrin et al., 2019](#)). [They exist in in](#)

Formatted: Indent: First line: 0"

152 areas that experience intense seasonal surface melting and rain ( $\sim 266\text{--}573$  mm w.e.  $\text{mm yr}^{-1}$ ) during the  
153 melting season, and lower snow accumulation ( $< -572 \pm 32$  mm w.e.  $\text{yr}^{-1}$ ) during the freezing season as  
154 compared to perennial firn aquifer areas (MacFerrin et al., 2019). Particularly in areas that experience  
155 intense seasonal surface melting ( $> 600$  mm  $\text{yr}^{-1}$ ) during the melting season, and lower snow accumulation  
156 ( $< 600$  mm  $\text{yr}^{-1}$ ) during the freezing season as compared to perennial firn aquifer areas (MacFerrin et al.,  
157 2019). Lower snow accumulation in ice slab areas results in a seasonal snow layer that is insufficiently thick  
158 to thermally insulate water-saturated firn layers and seasonal meltwater is instead stored as embedded ice.  
159 Refreezing of seasonal meltwater by the descending winter cold wave, and the subsequent formation of  
160 ice slabs as well as other embedded ice structures within the upper snow and firn layers is the single source  
161 of latent heat in ice slab areas. While ice slab areas are radiometrically warmer than other percolation facies  
162 areas with a lower volumetric fraction of embedded ice, they are radiometrically colder than perennial firn  
163 aquifer areas. This results in typically higher observed  $T^B$  at the ice sheet surface during the freezing  
164 season in ice slab areas, as compared to other percolation facies areas, however, typically lower observed  
165  $T^B$  as compared to perennial firn aquifer areas. Similar to temporal L-band signatures over perennial firn  
166 aquifer areas, temporal L-band signatures over ice slab areas are exponentially decreasing during the  
167 freezing season, however, the rate of  $T^B$  decrease is slightly more rapid. Lower snow accumulation in ice  
168 slab areas results in a seasonal snow layer that is insufficiently thick to thermally insulate water-saturated  
169 firn layers and seasonal meltwater is instead stored as embedded ice. Refreezing of seasonal meltwater  
170 by the descending winter cold wave, and the subsequent formation of ice slabs as well as other embedded  
171 ice structures within the upper snow and firn layers is the single source of latent heat in ice slab areas.  
172 While ice slab areas are radiometrically warmer than other percolation facies areas with a lower volumetric  
173 fraction of embedded ice, they are radiometrically colder than perennial firn aquifer areas. This results in a  
174 lower observed  $T^B$  at the ice sheet surface during the freezing season.

175 ~~In this study, we exploit the observed sensitivity of L-band emission to differences in the depth- and~~  
176 ~~time-integrated dielectric and geophysical properties of the percolation facies of the GrIS to map perennial~~  
177 ~~firn aquifer and ice slab areas together as a continuous englacial firn hydrological system using satellite L-~~  
178 ~~band microwave radiometry~~

179 ~~In this study, we exploit the observed sensitivity of L-band emissions to differences in the depth-~~  
180 ~~and time-integrated dielectric and geophysical properties of the percolation facies of the GrIS to map~~  
181 ~~perennial firn aquifer and ice slab areas together as a continuous englacial firn hydrological system using~~  
182 ~~satellite L-band microwave radiometry.~~

## 183 **2 Methods**

184  
185 ~~Consistent with recent seasonal surface melting trends, meltwater run-off has accelerated to~~  
186 ~~become the dominant mass loss mechanism over the GrIS (van den Broeke et al., 2016). However,~~  
187 ~~significant uncertainty remains in meltwater run-off estimates in the percolation facies as a result of the lack~~  
188 ~~of knowledge of heterogeneous infiltration processes within the snow and firn layers (Pfeffer and Humphrey,~~

189 1996), the depths to which meltwater can descend beneath the ice sheet surface (Humphrey et al., 2012),  
190 and the formation of englacial firn hydrological features (Benson et al., 1960; Humphrey et al., 2012; Forster  
191 et al., 2014), especially ice layers and ice slabs (Machguth et al., 2016; McFerrin et al., 2019; Culborg et  
192 al., 2021). A notable example of this lack of knowledge is the identification by Forster et al., (2014) of  
193 widespread perennial firn aquifers within the percolation facies of the GrIS via airborne ice penetrating radar  
194 surveys collected by NASA's OIB campaigns (2010-2014; Rodriguez-Morales et al., 2014) that store large  
195 volumes (~140 Gt; Koenig et al., 2014) of meltwater that was previously unknown. The mapped extent  
196 (2010-2014) shown in Forster et al., (2014) can be distinctly observed in 1978 enhanced resolution Ku-  
197 band radar backscatter imagery (Long and Drinkwater, 1994) collected by the radar scatterometer on  
198 NASA's first Earth observing satellite—the Seasat A mission (Jones et al., 1982). This suggests that  
199 Greenland's perennial firn aquifers have likely existed undetected in the deeper firn layers of the percolation  
200 facies for decades. Meltwater storage in both solid (i.e., embedded ice structures) and liquid (i.e., perennial  
201 firn and perched firn aquifers) form can buffer meltwater run-off in the percolation facies (Harper et al.,  
202 2012). However, the formation of near surface ice layers and ice slabs reduces the pore space within the  
203 upper snow and firn layers and facilitates lateral meltwater flow with minimum vertical percolation into the  
204 deeper firn layers, thus enhancing meltwater run-off downslope towards the periphery. Lateral meltwater  
205 flow across ice layers overlying deeper permeable firn layers was first postulated by Müller (1962). The  
206 theory was then further developed by Pfoffer et al., (1991) as an end member case for meltwater run-off,  
207 with the other end member case being lateral meltwater flow across superimposed ice in the wet snow  
208 facies and/or across glacial ice in the ablation facies. McFerrin et al., (2019) recently identified widespread  
209 near surface ice slabs within the percolation facies of the GrIS via airborne ice penetrating radar surveys  
210 collected by NASA's OIB campaigns (2010-2014; Rodriguez-Morales et al., 2014). Lateral meltwater flow  
211 and high-elevation (~1850 m.a.s.l.) meltwater run-off across the identified ice slabs was also observed in  
212 visible satellite imagery collected by the NASA-USGS Landsat 7 mission (e.g. Coward et al., 2001). This  
213 was also observed during the anomalous 2012 melting season (McFerrin et al., 2019) during which  
214 seasonal surface melting extended over ~99% of the GrIS (Nghiem et al., 2012)

215 ——— In this study, we use enhanced-resolution L-band  $T_V^B$  imagery (2015-2019) generated using  
216 observations collected over the GrIS by the microwave radiometer on the SMAP satellite (Brodzik et al.,  
217 2019) to map ice sheet-wide englacial firn hydrological features within the percolation facies. First, we  
218 adapt our previously developed empirical algorithm to map the extent of Greenland's perennial firn aquifers  
219 (Miller et al., 2020) using a multi-year calibration technique. We use enhanced-resolution L-band  $T_V^B$   
220 imagery (2015-2019) generated using observations collected over the GrIS by the microwave radiometer  
221 on NASA's SMAP satellite (Long et al., 2019) and airborne ice-penetrating radar surveys collected by  
222 NASA's OIB campaigns (Rodriguez-Morales et al., 2014). First, we correlate: (1) a 'firn saturation'  
223 parameter derived from a simple correlate two-layer L-band brightness temperature model (Miller et al.,  
224 2021, in press), (2) maximum and (3) minimum  $T_V^B$  values, and (4) exponentially decreasing temporal L-  
225 band signatures—with five years of perennial firn aquifer detections (2010-2014) identified via the CReSIS

226 Accumulation Radar (AR) ~~flown by NASA's OIB campaigns~~ (Miège et al. 2016), and three years of  
227 additional detections (2015-2017) more recently identified via MCoRDS (Miller et al., 2020). Next, we  
228 extend our empirical algorithm to ~~also~~ map the extent of ice slab ~~and perched firn aquifer~~ areas. ~~We identify~~  
229 ~~distinct temporal L-band signatures in  $T_{\nu}^{\beta}$  time series over ice slab detections (2010-2014) recently identified~~  
230 ~~via AR (McFerrin et al., 2019). Similar to temporal L-band signatures over perennial firn aquifer areas,~~  
231 ~~temporal L-band signatures over ice slab areas are exponentially decreasing during the freezing season,~~  
232 ~~however, the rate of  $T_{\nu}^{\beta}$  decrease is slightly more rapid. We correlate the SMAP-derived parameters these  
233 ~~relatively rapidly exponentially decreasing temporal L-band signatures~~ with five years of ice slab detections  
234 ~~(2010-2014) recently identified via AR (MacFerrin et al., 2019 AR-derived ice slab detection)s.~~ Additionally,  
235 ~~we correlate exponentially decreasing temporal L-band signatures with AR and MCoRDS derived~~  
236 ~~detections where perennial firn aquifer and ice slab areas overlap. We identify these transitional areas as~~  
237 ~~perched firn aquifer areas. We infer that, in these areas, shallow water saturated firn layers transiently form~~  
238 ~~on top of buried ice slabs or other semi-impermeable layers, such as spatially coherent melt layers that~~  
239 ~~form in the higher elevations ( $> 2000$  m.a.s.l.) of the percolation facies and the dry snow facies that were~~  
240 ~~recently identified via AR (Culberg et al., 2021). Perched firn aquifers likely form during some melting~~  
241 ~~seasons as a result of interannual variability in surface melting and snow accumulation, and the formation~~  
242 ~~of englacial firn hydrological features. Finally, we re-calibrate our empirical model ~~re-calibrate the~~  
243 ~~sigmoidal curves~~ to map the extent of perennial firn aquifer ~~and~~ ice slab, ~~and perched firn aquifer~~ areas  
244 over the percolation facies. Interannual variability in extent is not resolved in this study, however, it will be  
245 explored further in future work.~~~~

Formatted: Not Highlight

Formatted: Not Highlight

248 -facies of the GrIS

## 249

## 250 **2 — Methods**

### 251 **2.1 — The Soil Moisture Active Passive (SMAP) Mission**

252 The key science objectives of NASA's SMAP mission ( ) are to map terrestrial soil moisture and freeze/thaw  
253 state over Earth's land surfaces from space. However, the global L-band  $T^B$  observations collected by the  
254 SMAP satellite also have many cryospheric applications. Mapping ice sheet-wide englacial firn hydrological  
255 features over Earth's polar ice sheets represents an interesting analog and an innovative extension of the  
256 science objectives. Measurements of moisture (i.e., defined in this study in terms of the volumetric fraction  
257 of meltwater within the upper snow and firn layers of the percolation facies) and freeze-thaw state (i.e.,  
258 defined in this study in terms of the firn saturation parameter (see Section 2.4.3) and the refreezing rate  
259 parameter (see Section 2.4.4)) are critical to understanding the hydrospheric state over Earth's polar ice  
260 sheets. Perennial firn aquifers, ice slabs, and perched firn aquifers represent recently identified components  
261 of the hydrosphere that are capable of storing large volumes of meltwater in both solid and liquid form that  
262 can initiate meltwater-induced hydrofracturing and accelerated ice flow as well as high-elevation run-off,  
263 and impact the mass balance and stability of the GrIS. Critically, the majority of meltwater is stored at depths  
264 that only L-band satellite microwave sensors (i.e., radiometers, radar scatterometers, and synthetic  
265 aperture radars) are capable of detecting.

266 — Previous and current satellite microwave radiometer, radar scatterometer, and synthetic aperture  
267 radar missions that operate in the frequency range between 37 GHz (Ka-band) and 5.3 GHz (C-band) have  
268 provided a multi-decadal (1978-present) record of multi-frequency  $T^B$  and radar backscatter observations  
269 over Earth's polar ice sheets since the beginning of the satellite era. The most common geophysical  
270 parameter mapped over ice sheets using these observations is the extent of seasonal surface melting. The  
271 key difference between L-band and higher frequency satellite microwave sensors is penetration depth.  
272 When the snow and firn layers are saturated with meltwater during the melting season, the penetration  
273 depth of both L-band and higher frequency satellite microwave sensors is less than ~a meter. When surface  
274 and subsurface water-saturated snow and firn layers and embedded ice structures subsequently refreeze,  
275 the penetration depth of higher frequency satellite microwave sensors ranges from between ~centimeters  
276 and meters. During the freezing season, water-saturated snow and firn layers either completely refreeze  
277 (i.e., ice layers, ice slabs, spatially coherent melt layers) or underlay the refrozen upper snow and firn layers  
278 of the percolation facies and descend to depths ranging from between ~1 m and 40 m (Miège et al., 2016)  
279 beneath the ice sheet surface (i.e., perennial and perched firn aquifers). While the upper surface of stored  
280 meltwater in some perennial and perched firn aquifers may remain at depths that are shallow enough to be  
281 directly detected by C-band satellite microwave sensors, the mean depth just prior to melt onset (~22 m;



Miège et al., 2016) is too deep to be detected at this wavelength. L-band satellite microwave sensors can detect perennial firn aquifers from as much as an order of magnitude deeper than can be observed by C-band satellite microwave radiometers. Deep enough to directly detect the upper surface of stored meltwater over the entire depth range mapped by airborne ice-penetrating radar surveys over the GrIS.

## 2.1 SMAP Enhanced-Resolution L-band $T^B$ Imagery

The key science objectives of NASA's SMAP mission (<https://smap.jpl.nasa.gov/>) are to map terrestrial soil moisture and freeze/thaw state over Earth's land surfaces from space. However, the global L-band  $T^B$  observations collected by the SMAP satellite also have cryospheric applications. Mapping perennial firn aquifer and ice slab areas over Earth's polar ice sheets represents an interesting analog and an innovative extension of the science objectives. NASA's The SMAP satellite was launched 31 January 2015 and carries a microwave radiometer that operates at an L-band frequency of 1.41 GHz (L-band) (Enkentabi et al., 2010). It is currently collecting observations of vertically and horizontally-polarized  $T^B$  over Greenland. The surface incidence angle is  $\sim 40^\circ$ , and the radiometric accuracy is approximately  $\sim 1.3$  K (Piepmeier et al., 2017).

The Scatterometer Image Reconstruction (SIR) algorithm was originally developed to reconstruct coarse resolution satellite radar scatterometry imagery on a higher spatial resolution grid (Long et al., 1993; Early and Long, 2001). The SIR algorithm has been adapted for coarse resolution satellite microwave radiometry imagery (Long and Daum, 1998; Long and Brodzik, 2016; Long et al., 2019). The microwave radiometer form of the SIR algorithm (rSIR) exploits/uses the measurement response function (MRF) for each observation, which is a smeared version of the antenna pattern. Using the overlapping MRFs, the rSIR algorithm reconstructs  $T^B$  from the spatially filtered low-resolution sampling provided by the observations. In effect, it generates an MRF-deconvolved  $T^B$  image. Combining multiple multiple-orbital passes increases the sampling density, which improves both the accuracy and resolution of the SMAP enhanced-resolution  $T^B$  imagery (Long et al., 2019).

Over Greenland, the rSIR algorithm combines satellite orbital passes that occur between 8 a.m. and 4 p.m. local time-of-day to reconstruct SMAP enhanced-resolution  $T^B$  imagery twice-daily (i.e., morning and evening orbital pass interval, respectively).  $T^B$  imagery is projected on a Northern Hemisphere (NH) Equal-Area Scalable Earth Grid (EASE-Grid 2.0; Brodzik et al., 2012) at a 3.125 km rSIR grid cell spacing (e.g., Fig. 1). The effective resolution for each grid cell is dependent on the number of observations used in the rSIR reconstruction and is coarser than the rSIR grid cell spacing. While the effective resolution of conventionally processed SMAP  $T^B$  imagery posted on a 25 km grid is approximately  $\sim 30$  km (e.g., Fig. 1a), the effective resolution of SMAP enhanced-resolution  $T^B$  imagery posted on a 3.125 km grid is approximately  $\sim 18$  km (e.g., Fig. 1b), an improvement of  $\sim 60\%$  (Figs. 1; 2) (Long et al., 2020).

As previously noted, for our analysis of the percolation facies, we use SMAP enhanced-resolution

- Formatted: Font: 10 pt
- Formatted: Font: 10 pt
- Formatted: Font: 10 pt
- Formatted: Font: 10 pt
- Formatted: Space Before: 5 pt, After: 5 pt
- Formatted: Font: 10 pt
- Formatted: Font: 10 pt
- Formatted: Font: 10 pt
- Formatted: Not Highlight
- Formatted: Not Highlight
- Formatted: Not Highlight
- Formatted: Not Highlight
- Formatted: Space Before: 0 pt
- Formatted: Not Highlight
- Formatted: Not Highlight
- Formatted: Not Highlight
- Formatted: No widow/orphan control
- Formatted: Not Highlight

318  $T_V^B$  imagery over the GrIS. Compared to the horizontally-polarized channel, the vertically-polarized channel  
319 exhibits decreased sensitivity to variability in the volumetric fraction of meltwater, which is attributed to  
320 reflection coefficient [differences between channels](#) (Miller et al., 2020). [Using the vertically polarized](#)  
321 [channel also results in a reduced chi-squared error statistic when fitting  \$T\_V^B\$  time series to the sigmoid](#)  
322 [function \(see Section 2.34.45\)](#). We construct  $T_V^B$  imagery that alternate morning and evening orbital pass  
323 observations annually, beginning and ending just prior to melt onset. The Greenland Ice Mapping Project  
324 (GIMP) Land Ice and Ocean Classification Mask and Digital Elevation Model (Howat et al., 2014) are  
325 ~~differences between channels (Miller et al., 2020). Using the vertically polarized channel also results in a~~  
326 ~~reduced chi-squared error statistic when fitting  $T_V^B$  time series to the sigmoid function (see Section 2.4.5).~~  
327 ~~We construct  $T_V^B$  imagery that alternate morning and evening orbital pass observations annually, beginning~~  
328 ~~and ending just prior to melt onset. The Greenland Ice Mapping Project (GIMP) Land Ice and Ocean~~  
329 ~~Classification Mask and Digital Elevation Model (Howat et al., 2014) are projected on a NH EASE-Grid 2.0~~  
330 ~~at a 3.125 km rSIR grid cell spacing.  $T_V^B$  imagery between 1 April 2015 and 31 March 2019 are ice sheet~~  
331 ~~masked, and an elevation for each rSIR grid cell is calculated.~~

Formatted: Not Highlight

Formatted: Pattern: Clear

## 333 2.2 — Airborne Ice Penetrating Radar Surveys

Formatted: Justified, No widow/orphan control

334 Miller et al., (2020) calibrated the empirical algorithm to map the extent of Greenland's perennial firn  
335 aquifers by correlating a single year of exponentially decreasing temporal L-band signatures (2015-2016)  
336 with coincident perennial firn aquifer detections (2016) identified via MCoRDS. Here, we extend and expand  
337 the calibration of our adapted empirical algorithm to include four years of exponentially decreasing temporal  
338 L-band signatures (2015-2019) correlated with eight years of perennial firn aquifer detections (2010-2017)  
339 and five years of ice slab detections (2010-2014) identified via AR and MCoRDS (Fig. 1c). Our multi-year  
340 calibration technique projects perennial firn aquifer and ice slab detections on three separate NH EASE-  
341 Grids 2.0 at an rSIR grid cell spacing of 3.125 km, consistent with the rSIR grid cell spacing of the SMAP  
342 enhanced-resolution L-band  $T_V^B$  imagery. Interannual variability is not resolved in this study, however, it will  
343 be explored further in future work.

Formatted: No widow/orphan control, Tab stops: Not at 0.75"

344 — An advantage of the multi-year calibration technique as compared to the single coincident year  
345 calibration technique (Miller et al., 2020) is that it increases the number of rSIR grid cells that can be  
346 accessed. It also provides repeat targets that can account for variability in the dielectric and geophysical  
347 properties that seasonally influence the radiometric temperature and temporal L-band signatures in stable  
348 perennial firn aquifer, ice slab, and perched firn aquifer areas. Uncertainty is introduced by correlating  
349 exponentially decreasing temporal L-band signatures with AR and MCoRDS derived detections that are  
350 not coincident in time. The multi-year calibration technique assumes the extent of each area remains stable,  
351 which is not necessarily the case as climate extremes (Cullather et al., 2020) can influence each of these  
352 sub-facies. The assumption of stability neglects boundary transitions in the extent of perennial firn aquifer  
353 areas associated with refreezing of shallow water saturated firn layers, englacial drainage of meltwater into  
354 crevasses at the periphery (Poinar et al., 2017; Poinar et al., 2019), and transient upslope expansion

Formatted: No widow/orphan control

355 ~~(Montgomery et al., 2017). Once formed, ice slabs are essentially permanent features within the upper~~  
356 ~~snow and firn layers of the percolation facies until they are compressed into glacial ice. However, they may~~  
357 ~~transition into superimposed ice at the lower boundary of ice slab areas or rapidly expand upslope,~~  
358 ~~particularly following extreme melting seasons (McFerrin et al., 2019). By our definition, perched firn~~  
359 ~~aquifers are transient features. Thus, we simply consider our mapped extent a high probability area for the~~  
360 ~~preferential formation of each of these sub facies within the broader percolation facies, with continued~~  
361 ~~presence dependent on seasonal surface melting and snow accumulation in subsequent years.~~

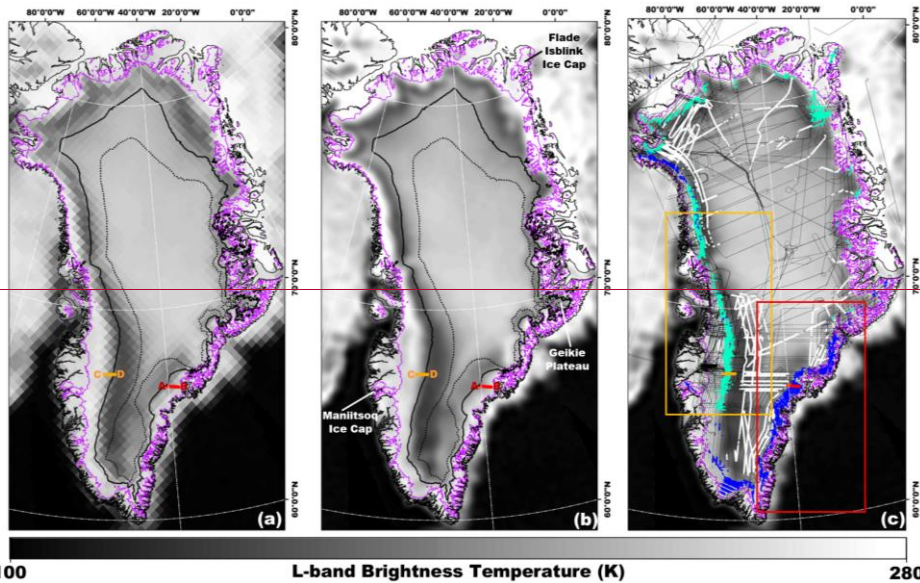


**Figure 1**

(a) Gridded (25 km), and (b) enhanced-resolution (3.125 km) L-band  $T_{\text{L}}^{\text{B}}$  imagery generated using observations collected 15 April 2016 by the microwave radiometer on the SMAP satellite during the evening orbital pass interval over Greenland (Brodzik et al., 2019). The solid black line is the 2000 m.a.s.l. contour, and the black dotted line is the 2500 m.a.s.l. contour (Howat et al., 2014). The purple line is the ice sheet extent (Howat et al., 2014). The black peripheral line is the coast of Greenland and adjacent Ellesmere Island (Wessel and Smith, 1996). The whiter regions of higher  $T_{\text{L}}^{\text{B}}$  over the high elevation ( $> 2500$  m.a.s.l.) interior are the dry snow facies. The darker grey regions of lower  $T_{\text{L}}^{\text{B}}$  are the percolation facies, including ice slabs and perched firn aquifer areas. The whiter regions of higher  $T_{\text{L}}^{\text{B}}$  over the coastal areas, peripheral ice caps (e.g., Maniitsoq and Flade Isblink) and nearby islands are perennial firn aquifers, superimposed or glacial ice, land, or spatially integrated L-band emissions. The whiter regions of higher  $T_{\text{L}}^{\text{B}}$  outside the ice sheet extent are sea ice. (c) The SMAP enhanced-resolution L-band  $T_{\text{L}}^{\text{B}}$  imagery is overlaid with AR- and MCoRDS-derived 2010-2017 perennial firn aquifer (blue shading; Miège et al., 2016), 2010-2014 ice slab (cyan shading; McFerrinMacFerrin et al., 2019), and 2012 spatially coherent melt layer (white shading; Culberg et al., 2021) detections along OIB flight lines (black lines). Overlapping perennial firn aquifer and ice slab detections are interpreted as perched firn aquifer areas. The red and orange boxes in (c) are zoom areas over south-eastern Greenland (Fig. 2a), and south-western Greenland (Fig. 2b), respectively. The red line is AR-radargram profile along perennial firn aquifer transect A-B (Fig. 3a). The orange line is AR

Formatted: Space Before: 0 pt, No widow/orphan control

Formatted: Strikethrough

Formatted: Strikethrough

Formatted: Strikethrough

Formatted: Strikethrough

Formatted: Strikethrough

Formatted: Strikethrough

Formatted: Strikethrough

Formatted: Strikethrough

Formatted: Strikethrough

Formatted: Strikethrough

Formatted: Strikethrough

Formatted: Strikethrough

Formatted: Strikethrough

Formatted: Strikethrough

Formatted: Strikethrough

Formatted: Strikethrough

Formatted: Strikethrough

Formatted: Strikethrough

382 *radargram profile along ice slab transect C-D (Fig. 3b).*

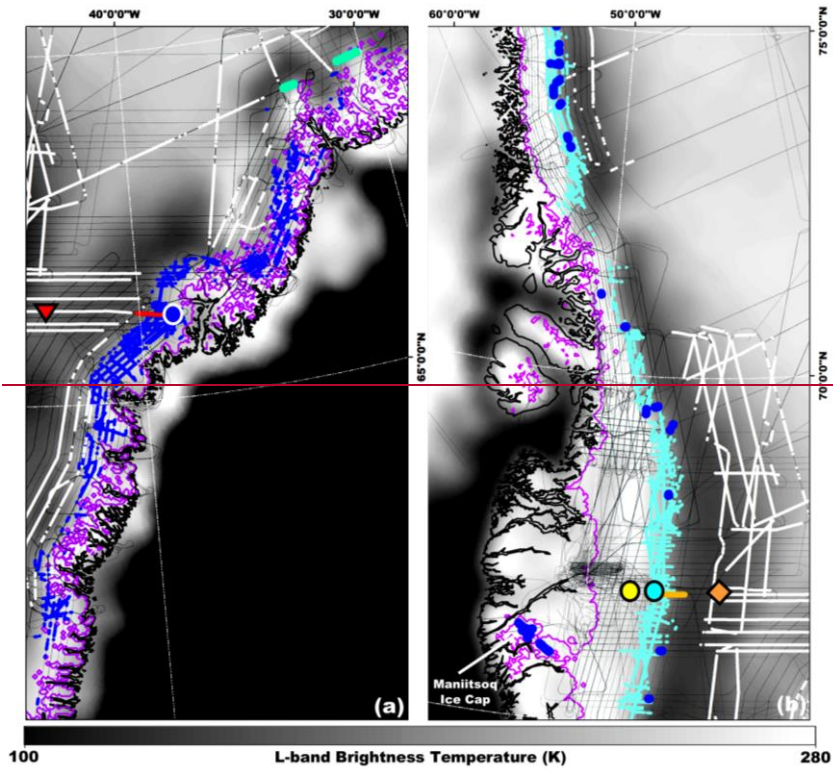


**Figure 2**

Enhanced-resolution (3.125 km) L-band  $T_v$  imagery generated using observations collected 15 April 2016 by the microwave radiometer on the SMAP satellite during the evening orbital pass interval over (a) south eastern Greenland (Fig. 1c; zoom area in red box), and (b) south western Greenland (Fig. 1c; zoom area in orange box) (Brodzik et al., 2019). The purple line is the ice sheet or ice cap extent (Howat et al., 2014). The black peripheral line is the coast (Wessel and Smith, 1996). (c) The SMAP-enhanced-resolution L-band  $T_v$  imagery is overlaid with AR- and MCoRDS-derived 2010-2017 perennial firn aquifer (blue shading; Miège et al., 2016), 2010-2014 ice slab (cyan shading; McFerrinMacFerrin et al., 2019), and 2012 spatially coherent melt layer (white shading; Culberg et al., 2021) detections along OIB flight lines (black lines). Overlapping perennial firn aquifer and ice slab detections are interpreted as perched firn aquifer areas. The red line is AR-radargram profile along perennial firn aquifer transect A-B (Figs. 1; 3a). The orange line is AR-radargram profile along ice slab transect C-D (Figs. 1; 3b). The blue circle is a perennial firn aquifer area (Figs. 3a; 4a). The cyan circle is a perched firn aquifer area (Figs. 3b; 4b). The orange diamond is a percolation facies area (Fig. 4c). The red triangle is a high-elevation (~2500 m.a.s.l.) percolation facies area

Perennial Firn Aquifers & Ice Slabs, Perched Firn Aquifers

Formatted: No widow/orphan control

Formatted: Space Before: 0 pt, No widow/orphan control

398 (Fig. 4d). The yellow circle is a superimposed ice area (Fig. 4e).

399 projected on thea NH EASE-Grid 2.0 at a 3.125 km rSIR grid cell spacing.  $T_v^P$  imagery between 1 April 2015  
400 and 31 March 2019 are ice sheet-masked, and an elevation for each rSIR grid cell is calculated.

## 401 2.2 Airborne Ice-Penetrating Radar Surveys

402 Miller et al., (2020) calibrated the empirical algorithm to map the extent of Greenland's perennial firn  
403 aquifers by correlating a single year of exponentially decreasing temporal L-band signatures (2015-2016)  
404 with coincident perennial firn aquifer detections (2016) identified via MCoRDS. Here, we extend and  
405 expand the calibration of our adapted empirical algorithm to include four years of exponentially  
406 decreasing temporal L-band signatures (2015-2019) correlated with eight years of perennial firn aquifer  
407 detections (2010-2017) and five years of ice slab detections (2010-2014) identified via AR and MCoRDS  
408 (Fig. 1c).

409 Our multi-year calibration technique projects perennial firn aquifer and ice slab detections on three separate  
410 NH EASE-Grids 2.0 at an rSIR grid cell spacing of 3.125 km, consistent with the rSIR grid cell spacing of  
411 the SMAP enhanced-resolution L-band  $T_v^P$  imagery. Interannual variability is not resolved in this study,  
412 however, it will be explored further in future work.

413 \_\_\_\_\_ An advantage of the multi-year calibration technique as compared to the single-coincident year  
414 calibration technique (Miller et al., 2020) is that it increases the number of rSIR grid cells that can be  
415 assessed. It also provides repeat targets that can account for variability in the dielectric and geophysical  
416 properties that seasonally influence the radiometric temperature and temporal L-band signatures in stable  
417 perennial firn aquifer, ice slab, and perched firn aquifer areas. Uncertainty is introduced by correlating  
418 exponentially decreasing temporal L-band signatures with AR- and MCoRDS-derived detections that are  
419 not coincident in time. The multi-year calibration technique assumes the extent of each area remains  
420 stable, which is not necessarily the case as climate extremes (Cullather et al., 2020) can influence each  
421 of these sub-facies. The assumption of stability neglects boundary transitions in the extent of perennial  
422 firn aquifer areas associated with refreezing of shallow water-saturated firn layers, englacial drainage of  
423 meltwater into crevasses at the periphery (Poinar et al., 2017; Poinar et al., 2019), and transient upslope  
424 expansion (Montgomery et al., 2017). Once formed, ice slabs are essentially permanent features within  
425 the upper snow and firn layers of the percolation facies until they are compressed into glacial ice.  
426 However, they may transition into superimposed ice at the lower boundary of ice slab areas or rapidly  
427 expand upslope, particularly following extreme melting seasons (McFerrin, MacFerrin et al., 2019). By our  
428 definition, perched firn aquifers are transient features. Thus, we simply consider our mapped extent a  
429 high-probability area for the preferential formation of each of these sub-facies within the broader  
430 percolation facies, with continued presence dependent on seasonal surface melting and snow  
431 accumulation in subsequent years \_\_\_\_\_ Annual perennial firn aquifer and ice slab detections that may  
432 introduce significant uncertainty into the multi-year calibration technique include those following the 2010  
433 melting season, which was exceptionally long (Tedesco et al., 2010), the anomalous 2012 melting season  
434 (Nghiem et al., 2012), and the 2015 melting season which was especially intense in western and northern  
435 Greenland (Tedesco et al., 2016). Following these extreme melting seasons, significant changes in the  
436 dielectric and geophysical properties likely occurred across large portions of the GRS, including perennial  
437 firn aquifer recharging resulting in increases in meltwater volume and decreases in the depth to the upper  
438 surface of stored meltwater. The formation of expansive near-surface ice slabs (McFerrin, MacFerrin et al.,  
439 2019) likely resulted in the formation of more extensive perched firn aquifers during subsequent melting  
440 seasons. The upper snow and firn layers of the dry snow facies and percolation facies were also  
441 saturated with relatively large volumetric fractions of meltwater as compared to the negligible to limited

Formatted: Font: 10 pt

Formatted: Font: 10 pt

Formatted: Font: 10 pt

Formatted: Font: 10 pt

Formatted: Space Before: 5 pt, After: 5 pt

Formatted: Font: 10 pt

Formatted: Left, Space Before: 5 pt, After: 5 pt, Tab stops: Not at 0.75"

Formatted: Font: 10 pt

Formatted: Normal, Left, Line spacing: single



442 volumetric fractions of meltwater that percolates during more typical seasonal surface melting on the  
443 GrIS. Seasonal meltwater was refrozen into spatially coherent melt layers following the 2010 and 2012  
444 melting seasons (Culberg et al., 2021) as well as following the 2015 and 2018 melting seasons (i.e.,  
445 identified as part of the temporal L-band signature analysis in this study; see Section 2.4.2).  
446 ~~As compared to ice slabs, which are dense low permeability solid ice layers, spatially coherent melt~~  
447 ~~layers are a network of embedded ice structures primarily consisting of discontinuous horizontally-oriented~~  
448 ~~ice layers and ice lenses sparsely connected via vertical-oriented ice pipes (Culberg et al., 2021). Ice slabs~~  
449 ~~are relatively thick (~1 m – 16 m) and form in the high-elevation percolation facies (~2100 m.a.s.l.) at depths~~  
450 ~~of between ~1 m and 20 m beneath the ice sheet surface following intense seasonal surface melting over~~  
451 ~~multiple melting seasons (McFerrinMacFerrin et al., 2019). Spatially coherent melt layers are relatively thin~~  
452 ~~(~0.02 cm – 2 m) and can rapidly form across the entire high-elevation dry snow facies (~3200 m.a.s.l. ;~~  
453 ~~Nghiem et al., 2012) at depths of less than ~1 m beneath the ice sheet surface following a single extreme~~  
454 ~~melting season. They can further merge together into thicker solid ice layers following multiple extreme~~  
455 ~~melting seasons (Culberg et al., 2021). Similar to ice slabs, the formation of spatially coherent melt layers~~  
456 ~~reduces the pore space within the upper snow and firn layers and may also facilitate lateral meltwater flow~~  
457 ~~with minimum vertical percolation into the deeper firn layers, thus enhancing meltwater run-off from~~  
458 ~~significantly higher elevations downslope towards the periphery on accelerated time scales. The formation~~  
459 ~~of spatially coherent melt layers overlying deeper perennial firn aquifers (e.g., Fig. 3a) will limit or terminate~~  
460 ~~gravity-driven meltwater drainage and seasonal recharging (Fountain and Walder, 1998), which may~~  
461 ~~eventually completely refreeze stored meltwater into decimeters thick solid ice layers overlying deeper~~  
462 ~~glacial ice. Spatially coherent melt layers are exceptionally bright in AR radargrams (e.g., Fig 3a). The large~~  
463 ~~dielectric contrast between the spatially coherent melt layer and the overlying, underlying, and interior snow~~  
464 ~~and firn layers results in high reflectivity at the interfaces. However, electromagnetic energy still propagates~~  
465 ~~downward through the high reflectivity layer into the deeper firn layers. Culberg et al., 2021) recently~~  
466 ~~demonstrated mapping the extent of the spatially coherent melt layer formed following the anomalous 2012~~  
467 ~~melting season (Nghiem et al., 2012) via AR (Figs. 1c; 2). ~~AR and MCoRDS (Rodriguez-Morales et~~  
468 ~~al. 2014) were flown over the GrIS on a P-3 aircraft in April and May between 2010 and 2017, (Figs. 1c; 2).~~  
469 ~~The AR instrument operates at a center frequency of 750 MHz with a bandwidth of 300 MHz, resulting in a~~  
470 ~~range resolution in firn of 0.53 m (Lewis et al., 2015). The collected data have an along-track resolution of~~  
471 ~~approximately ~30 m with 15 m spacing between traces in the final processed radargrams. At a nominal~~  
472 ~~flight altitude of 500 m above the ice sheet surface, the cross-track resolution varies between 20 m for a~~  
473 ~~smooth surface, to 54 m for a rough surface with no appreciable layover. The MCoRDS instrument operated~~  
474 ~~at three different frequency configurations: (1) a center with a bandwidth of 30 MHz (2010-2014, 2017,~~  
475 ~~2018), (2) a center frequency of 315 MHz with a band width of 270 MHz (2015), and (3) a center frequency~~  
476 ~~of 300 MHz with a bandwidth of 300 MHz (2016). The vertical range resolution in firn for each of these~~  
477 ~~frequency configurations is 5.3 m, 0.59 m, and 0.53m, respectively (CReSIS, 2016). The collected data~~  
478 ~~have an along-track resolution of approximately 25 m with 14 m spacing between traces in the final~~  
479 ~~processed radargrams. At a nominal flight altitude of 500 m, the cross-track resolution varies between 40~~~~

Formatted: Not Highlight

480 m for a smooth surface in the highest bandwidth configuration, to 175 m for a rough surface with no  
481 appreciable layover in the lowest bandwidth configuration.

482 The multi-year calibration technique uses perennial firn aquifer detections previously identified  
483 along OIB flight lines via AR (2010-2014) and MCoRDS (2015-2017) radargram profiles and the  
484 methodology described in Miège et al. (2016). Bright lower reflectors that undulate with the local  
485 topographic gradient underneath which reflectors are absent in the percolation facies are interpreted as the  
486 upper surface of meltwater stored within perennial firn aquifers (e.g., Fig. 3a). The large dielectric contrast  
487 between refrozen and water-saturated firn layers results in high reflectivity at the interface. However, the  
488 presence of meltwater increases attenuation, limiting the downward propagation of electromagnetic energy  
489 through the water-saturated firn layer. The total number of AR derived perennial firn aquifer detections is  
490 325,000, corresponding to a total extent of 98 km<sup>2</sup>. The analysis assumes a smooth surface, which is typical  
491 of much of the percolation facies, and a grid cell size of 15 m x 20 m. The total number of MCoRDS-derived  
492 perennial firn aquifer detections is 142,000, corresponding to a total extent of 80 km<sup>2</sup>. This analysis also  
493 assumes a smooth surface, and a grid cell size of 14 m x 40 m. The combined total number of grid cells  
494 (467,000) and total extent (178 km<sup>2</sup>) is significantly larger than the total number of MCoRDS-derived grid  
495 cells (78,000) and total extent (44 km<sup>2</sup>) calculated for 2016 (Miller et al., 2020). Perennial firn aquifer  
496 detections are mapped in western, southern, and south and central eastern Greenland as well as the  
497 Maniitsoq and Flade Isblink Ice Caps (Figs. 1c; 2a). We project AR- and MCoRDS-derived perennial firn  
498 aquifer detections on the NH EASE-Grid 2.0 at an rSIR grid cell spacing of 3.125 km. Each rSIR grid cell  
499 has an extent of approximately 10 km<sup>2</sup>. The total number of rSIR grid cells with at least one perennial firn  
500 aquifer detection is 800, corresponding to a total extent of 8000 km<sup>2</sup>. However, given the limited AR and  
501 MCoRDS grid cell coverage, less than 1% of the rSIR grid cell extent has airborne ice-penetrating radar  
502 survey coverage. As compared to the total resolution varies between 20 m for a smooth surface, to 54 m  
503 for a rough surface with no appreciable layover. The

Formatted: No widow/orphan control

Formatted: Font: 10 pt

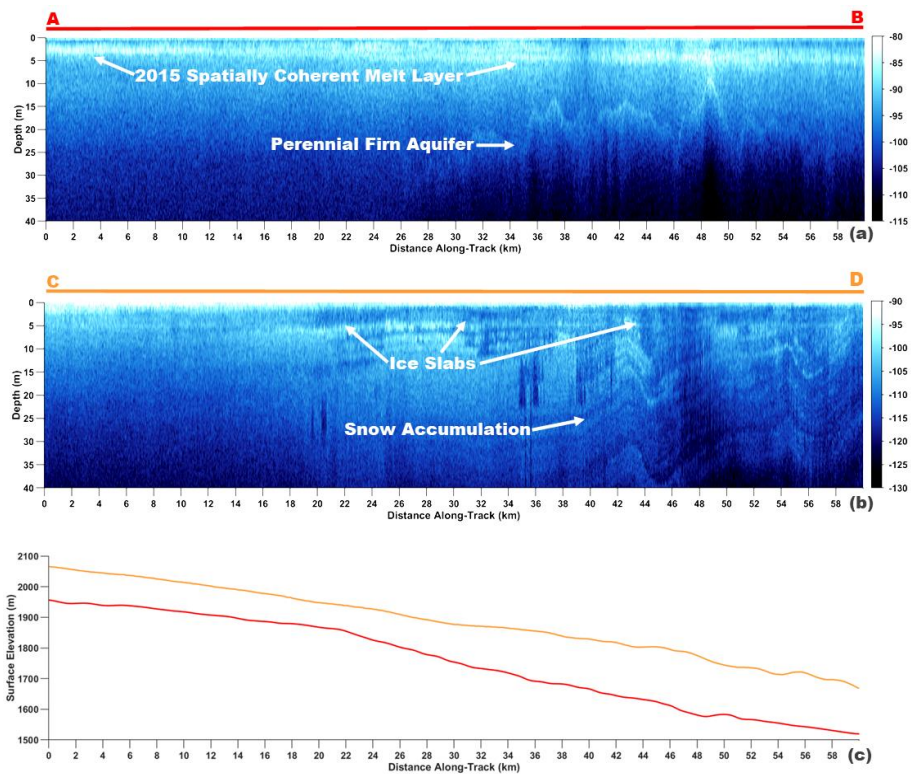


**Figure 3**

AR-radargram profile (Rodríguez-Morales et al., 2014) (a) along perennial firn aquifer transect A-B (red line, Figs. 1; 2a) that was collected on 22 April 2017, and (b) ice slab transect C-D (orange line, Figs. 1; 2b) that was collected on 5 May 2017. (c) The corresponding perennial firn aquifer transect A-B elevation profile (red line), and ice slab transect C-D elevation profile (orange line). The exceptionally bright upper surface-parallel reflector in (a) is interpreted as a spatially coherent melt layer that formed following the 2015 melting season. The bright lower reflector in (a) is interpreted as the upper surface of meltwater stored within a perennial firn aquifer. Thick dark surface-parallel regions of low reflectivity in (b) are interpreted as ice slabs. Alternating sequences of bright and dark surface-parallel reflectors in (b) are interpreted as seasonal snow accumulation layers. A first maximum after maximum gradient re-tracker is used to identify the surface return in each profile. Each profile is flattened so that the depth axis is measured relative to the local elevation. Corresponding elevation profiles in (c) are calculated by subtracting the radar-measured flight clearance over the ice sheet from the aircraft's global positioning system altitude measurements that were coincidentally collected along each transect.

Formatted: Font: 10 pt

Formatted: Space Before: 0 pt

519 ~~AR and MCoRDS (Rodríguez-Morales et al., 2014) were flown over the GrIS on a P-3 aircraft in~~  
520 ~~April and May between 2010 and 2017. The AR instrument operates at a center frequency of 750 MHz with~~  
521 ~~a bandwidth of 300 MHz, resulting in a range resolution in firn of 0.53 m (Lewis et al., 2015). The collected~~  
522 ~~data have an along track resolution of 30 m with 15 m spacing between traces in the final processed~~  
523 ~~radargrams. At a nominal flight altitude of 500 m above the ice sheet surface, the cross track resolution~~  
524 ~~varies between 20 m for a smooth surface, to 54 m for a rough surface with no appreciable layover. The~~  
525 ~~MCoRDS instrument operated at three different frequency configurations: (1) a center frequency of 195~~  
526 ~~MHz with a bandwidth of 30 MHz (2010-2014, 2017, 2018), (2) a center frequency of 315 MHz with a band~~  
527 ~~width of 270 MHz (2015), and (3) a center frequency of 300 MHz with a bandwidth of 300 MHz (2016). The~~  
528 ~~vertical range resolution in firn for each of these frequency configurations is 5.3 m, 0.59 m, and 0.53m,~~  
529 ~~respectively (CReSIS, 2016). The collected data have an along track resolution of ~25 m with 14 m spacing~~  
530 ~~between traces in the final processed radargrams. At the same nominal flight altitude of 500 m, the cross-~~  
531 ~~track resolution varies between 40 m for a smooth surface in the highest bandwidth configuration, to 175~~  
532 ~~m for a rough surface with no appreciable layover in the lowest bandwidth configuration.~~

533 ~~The multi-year calibration technique uses perennial firn aquifer detections previously identified~~  
534 ~~along OIB flight lines via AR (2010-2014) and MCoRDS (2015-2017) radargram profiles and the~~  
535 ~~methodology described in Miège et al. (2016). Bright lower reflectors that undulate with the local~~  
536 ~~topographic gradient underneath which reflectors are absent in the percolation facies are interpreted as the~~  
537 ~~upper surface of meltwater stored within perennial firn aquifers (e.g., Fig. 3a). The large dielectric contrast~~  
538 ~~between refrozen and water-saturated firn layers results in high reflectivity at the interface. However, the~~  
539 ~~presence of meltwater increases attenuation, limiting the downward propagation of electromagnetic energy~~  
540 ~~through the water-saturated firn layer. The total number of AR derived perennial firn aquifer detections is~~  
541 ~~~325,000, corresponding to a total extent of ~98 km<sup>2</sup>. The analysis assumes a smooth surface, which is~~  
542 ~~typical of much of the percolation facies, and a grid cell size of 15 m x 20 m. The total number of MCoRDS-~~  
543 ~~derived perennial firn aquifer detections is ~142,000, corresponding to a total extent of ~80 km<sup>2</sup>. This also~~  
544 ~~assumes a smooth surface, and a grid cell size of 14 m x 40 m. The combined total number of grid cells~~  
545 ~~(~467,000) and total extent (~178 km<sup>2</sup>) is significantly larger than the total number of MCoRDS-derived grid~~  
546 ~~cells (~78,000) and total extent (~44 km<sup>2</sup>) calculated for 2016 (Miller et al., 2020). Perennial firn aquifer~~  
547 ~~detections are mapped in western, southern, and south and central eastern Greenland as well as the~~  
548 ~~Maniitsoq and Flade Isblink Ice Caps (Figs. 1c; 2a). We project AR- and MCoRDS-derived perennial firn~~  
549 ~~aquifer detections on the NH EASE Grid 2.0 at an rSIR grid cell spacing of 3.125 km. Each rSIR grid cell~~  
550 ~~has an extent of ~10 km<sup>2</sup>. The total number of rSIR grid cells with at least one perennial firn aquifer detection~~  
551 ~~is ~800, corresponding to a total extent of ~8000 km<sup>2</sup>. However, given the limited AR and MCoRDS grid~~  
552 ~~cell coverage, less than ~1% of the rSIR grid cell extent has radargram coverage. As compared to the total~~  
553 ~~number of MCoRDS-derived perennial firn aquifer detections (~780) calculated for 2016 (Miller et al., 2020),~~  
554 ~~the total number of rSIR grid cells with at least one detection is only increased by ~20 for the multi-year~~  
555 ~~calibration technique, corresponding to an increased total extent of ~200 km<sup>2</sup>.~~

Formatted: No widow/orphan control

556 We also use ice slab detections previously identified along OIB flight lines via AR (2010-2014)  
557 radargram profiles and the methodology described in [MacFerrin et al. \(2019\)](#) in the multi-year  
558 calibration technique. Thick dark surface-parallel regions of low-reflectivity in the percolation facies are  
559 interpreted as ice slabs (e.g., Fig. 3b). The large dielectric contrast between ice slabs and the overlying and  
560 underlying snow and firn layers results in high reflectivity at the interfaces. However, electromagnetic  
561 energy is not scattered or absorbed within the homogeneous ice slab, it instead propagates downward  
562 through the layer and into the deeper firn layers. The total number of AR-derived ice slab detections is  
563 ~505,000, corresponding to a total extent of ~283 km<sup>2</sup>. Ice slab detections are mapped in western, central  
564 and north eastern, and northern Greenland as well as the Flade Isblink Ice Cap (Figs. 1c; 2b). We project  
565 the AR-derived ice slab detections on the NH EASE-Grid 2.0 at an rSIR grid cell spacing of 3.125 km. The  
566 total number of rSIR grid cells with at least one ice slab detection is ~2000, corresponding to a total extent  
567 of ~20,000 km<sup>2</sup>. However, less than ~2% of the rSIR grid cell extent has airborne ice-penetrating radar  
568 survey radargram coverage.

Formatted: Not Highlight

569 An advantage of the multi-year calibration technique as compared to the single-coincident year  
570 calibration technique (Miller et al., 2020) is that it increases the number of rSIR grid cells that can be  
571 assessed. It also provides repeat targets that can account for variability in the depth- and time-integrated  
572 dielectric and geophysical properties that influence the radiometric temperature in stable perennial firn  
573 aquifer and ice slab areas. Uncertainty is introduced by correlating the SMAP-derived parameters with AR-  
574 and MCoRDS-derived detections that are not coincident in time. The multi-year calibration technique  
575 assumes the extent of each area remains stable, which is not necessarily the case as climate extremes  
576 (Cullather et al., 2020) can influence each of these sub-facies. The assumption of stability neglects  
577 boundary transitions in the extent of perennial firn aquifer areas associated with refreezing of shallow water-  
578 saturated firn layers, englacial drainage of meltwater into crevasses at the periphery (Poinar et al., 2017;  
579 Poinar et al, 2019), and transient upslope expansion (Montgomery et al., 2017). Once formed, ice slabs are  
580 essentially permanent features within the upper snow and firn layers of the percolation facies until they are  
581 compressed into glacial ice. However, they may transition into superimposed ice at the lower boundary of  
582 ice slab areas or rapidly expand upslope, particularly following extreme melting seasons (MacFerrin et al.,  
583 2019). Thus, we simply consider our mapped extent a high-probability area for the preferential formation of  
584 each of these sub-facies, with continued presence dependent on seasonal surface melting and snow  
585 accumulation in subsequent years.

Formatted: Not Highlight

Formatted: Tab stops: 0.5", Left + Not at 0.75"

586 Annual perennial firn aquifer and ice slab detections that may introduce significant uncertainty into  
587 the multi-year calibration technique include those following the 2010 melting season, which was  
588 exceptionally long (Tedesco et al., 2010), the anomalous 2012 melting season, during which seasonal  
589 surface melting extended across 99% of the GrIS (Nghiem et al., 2012), and the 2015 melting season,  
590 which was especially intense in western and northern Greenland (Tedesco et al., 2016). Following these  
591 extreme melting seasons, significant changes in the dielectric and geophysical properties likely occurred  
592 across large portions of the GrIS, including perennial firn aquifer recharging resulting in increases in

Formatted: Not Highlight

593 meltwater volume and decreases in the depth to the upper surface of stored meltwater. The upper snow  
594 and firn layers of the dry snow facies and percolation facies were also saturated with relatively large  
595 volumetric fractions of meltwater as compared to the negligible to limited volumetric fractions of meltwater  
596 that percolates during more typical seasonal surface melting on the GrlS.

597 Seasonal meltwater was refrozen into spatially coherent melt layers following the 2010 and 2012  
598 melting seasons (Culberg et al., 2021) as well as more recently following the 2015, and 2018 melting  
599 seasons identified as part of the temporal L-band signature analysis in this study, (Section 2.3.1). As  
600 compared to ice slabs, which are dense low-permeability solid-ice layers, spatially coherent melt layers are  
601 a network of embedded ice structures primarily consisting of discontinuous horizontally-oriented ice layers  
602 and ice lenses sparsely connected via vertical-oriented ice pipes (Culberg et al., 2021). Spatially coherent  
603 melt layers are relatively thin (0.02 cm-2 m) and can rapidly form across the high-elevation (up to 3200 m  
604 a.s.l.) dry snow facies, at depths of less than 1 m beneath the ice sheet surface following a single extreme  
605 melting season. They can further merge together into thicker solid-ice layers following multiple extreme  
606 melting seasons. Spatially coherent melt layers are exceptionally bright in AR radargrams (e.g., Fig 3a).  
607 The large dielectric contrast between the spatially coherent melt layer and the overlying, underlying, and  
608 interior snow and firn layers results in high reflectivity at the interfaces. However, electromagnetic energy  
609 still propagates downward through the high reflectivity layer into the deeper firn layers. Culberg et al., (2021)  
610 recently demonstrated mapping the extent of spatially coherent melt layers formed following the 2012  
611 melting season (Nghiem et al., 2012) via AR (Figs. 1c; 2).

612  
613 We detect perched firn aquifer areas by comparing the AR- and MCoRDS-derived perennial firn  
614 aquifer and ice slab detections projected on the NH EASE-Grid 2.0 and then identify overlapping rSIR-grid  
615 cells. The total number of AR-derived perched firn aquifer detections is ~75,000, corresponding to a total  
616 extent of ~23 km<sup>2</sup>. The total number of MCoRDS-derived perched firn aquifer detections is ~20,  
617 corresponding to a near-negligible extent (~0.006 km<sup>2</sup>). Perched firn aquifer detections are mapped in  
618 western, and central eastern Greenland as well as the Flade Isblink Ice Cap (Figs. 1c; 2b).

619 The total number of rSIR-grid-cells with at least one perched firn aquifer detection is ~200,  
620 corresponding to a total extent of ~2000 km<sup>2</sup>. However, similar to the other sub-facies, less than ~1% of  
621 the rSIR-grid-cell extent has radargram coverage. The total number of AR- and MCoRDS-derived perennial  
622 firn-aquifer, ice-slab, and perched firn-aquifer detections that we project on three separate NH EASE-Grids  
623 2.0, the associated total number of rSIR-grid-cells that we use in the calibration of our adapted empirical  
624 algorithm, and the coverage of detections and rSIR-grid-cells over each of the three sub-facies within the  
625 broader percolation facies are summarized in Table 1.

626  
627 **Table 1.** The total number of airborne ice-penetrating radar survey detections (2010-2017), the associated  
628 total number of rSIR-grid-cells, and the coverage of detections and rSIR-grid-cells over perennial firn aquifer,  
629 ice-slab, and perched firn aquifer areas.

Formatted: Not Highlight

Formatted: Not Highlight

Formatted: Not Highlight

Formatted: Not Highlight

Formatted: Not Highlight

	Detections	Coverage (km <sup>2</sup> )	rSIR-Grid Cells	Coverage (km <sup>2</sup> )
<b>Perennial Firn Aquifers</b>	~467,000	~178	~80	~8000
<b>Ice Slabs</b>	~505,000	~283	~2000	~20,000
<b>Perched Firn Aquifers</b>	~75,000	~23	~200	~2000

630

631

Formatted: Font: 10 pt

Formatted: Space Before: 1 line, After: 5 pt



632 **2.34 Empirical Algorithm**

633 **2.4.1 Greenland's Ice Facies**

634 Greenland's ice facies (i.e., dry snow facies—percolation facies—wet snow facies—ablation facies) were  
635 first described in detail by Benson et al., (1960), and were shown to represent the GrlS's response to  
636 climate. Evolution of the boundaries of Greenland's ice facies are often used as an indicator of climate  
637 change. Early studies using field-based (Jezek et al., 1994; Zabel et al., 1995), airborne (Swift et al., 1985;  
638 Bindschadler et al., 1987; Rignot et al., 1993; Jezek et al., 1993), and satellite (Fahnestock et al., 1993;  
639 Long and Drinkwater, 1994; Parrington, 1998) synthetic aperture radars and radar scatterometers operating  
640 at frequencies between Ku band (13 GHz) and P band (0.4 GHz) have demonstrated the exceptional  
641 capabilities of microwave sensors for mapping Greenland's ice facies. Early airborne studies using C-band  
642 microwave radiometry (Swift et al., 1985), and more recent studies using L-band microwave radiometry  
643 (Jezek et al., 2018) have demonstrated similar capabilities. In this study, we extend these capabilities to  
644 include satellite L-band microwave radiometry. We delineate the boundaries of the percolation facies  
645 relative to the adjacent dry snow facies (i.e., where negligible seasonal surface melting occurs) and wet  
646 snow facies (i.e., where snow layers are fully water-saturated during the melting season and subsequently  
647 refreeze as superimposed ice overlying deeper glacial ice). And, we further identify sub-facies (i.e.,  
648 perennial firn aquifer, ice slabs, and perched firn aquifers) within the broader percolation facies that are  
649 currently experiencing rapid expansion (McFerrin et al., 2010; Culberg et al., 2021) as Greenland's climate  
650 continues to warm (Hanna et al., 2013; Cullather et al., 2020) and seasonal surface melting increases in  
651 extent, intensity, and duration (Steffen et al., 2004; Tedesco et al., 2008; Tedesco et al., 2011; Nghiem et  
652 al., 2012; Tedesco et al., 2016; Tedesco and Fettweis, 2020; Tedesco and Fettweis, 2020). Higher  
653 frequency microwave sensors provide shallower penetration depths, and an increased sensitivity to snow  
654 grain size, layering, embedded ice structures (Long and Drinkwater, 1994; Drinkwater et al., 2001) and  
655 stored meltwater (Jezek et al., 1993; Miller, 2019) within the upper snow and firn layers of the percolation  
656 facies. Lower frequencies provide deeper penetration depths and a range of sensitivities to embedded ice  
657 structures (Jezek et al., 1993; Jezek et al., 2018) and stored meltwater (Miller et al., 2020) in the deeper  
658 firn layers.

659  
660 **2.34.12 Temporal L-band Signatures over the Percolation Facies**

661 Microwave brightness temperature ( $T^B$ ) expresses the satellite-observed magnitude of thermal emission  
662 and is influenced by the microwave instrument's observation geometry as well as the depth- and time-  
663 integrated dielectric and geophysical properties of the ice sheet (Ulaby et al., 2014). The most significant  
664 geophysical property influencing  $T^B$  is the volumetric fraction of meltwater within the snow and firn pore  
665 space (Mätzler and Hüppi, 1989). During the melting season, the upper snow and firn layers of the  
666 percolation facies are saturated with large volumetric fractions of meltwater that percolates vertically into

Formatted: Font: 10 pt

Formatted: Not Highlight

Formatted: Font: 10 pt

Formatted: Space Before: 5 pt, After: 5 pt

Formatted: Space Before: 5 pt, After: 5 pt, Tab stops: 0", Left + 0.5", Left

Formatted: Space Before: 5 pt, After: 5 pt

Formatted: Not Highlight

Formatted: Not Highlight

Formatted: Not Highlight

Formatted: Space Before: 0 pt

Formatted: Not Highlight



667 the deeper firn layers (Benson, 1960; Humphrey et al., 2012). Increases in the volumetric fraction of  
668 meltwater results in rapid relative increases in the imaginary part of the complex dielectric constant (Tiuri  
669 et al., 1984), ~~with corresponding~~ **This typically** increases in  $T^B$ , ~~and. This increase~~ ~~decreases~~ ~~is attributed~~  
670 ~~to a decrease in~~ volume scattering, and penetration depth. The L-band penetration depth can rapidly  
671 decrease from ~~–tens to hundreds of meters,~~ to less than ~~–a meter,~~ dependent on the local snow and firn  
672 conditions, ~~and englacial firn hydrological features.~~ During the freezing season, ~~s~~Surface and subsurface  
673 water-saturated snow and firn layers and embedded ice structures subsequently refreeze. ~~De~~During the  
674 freezing season, ~~de~~creases in the volumetric fraction of meltwater results in rapid relative decreases in the  
675 imaginary part of the complex dielectric constant. ~~This, with corresponding~~ decreases in  $T^B$ . ~~This increase~~  
676 ~~is attributed to an increase in~~ and increases volume scattering, and penetration depth. The L-band  
677 penetration depth increases back to ~~–tens to hundreds of meters~~ on variable time scales.

678 We analyze melting and freezing seasons in temporal L-band signatures exhibited in  $T_V^B$  time series  
679 ~~(1 April 2015 – 31 March 2019)~~ over and near the AR- and MCoRDS-derived perennial firn aquifer, and, ice  
680 slab, and perched firn aquifer detections projected on the NH EASE-Grids 2.0 (Fig. 4, Table 1). We project  
681 ice surface temperature data observations calculated using thermal infrared brightness temperature  
682 collected by the Moderate Resolution Imaging Spectroradiometer (MODIS) on the Terra and Aqua satellites  
683 (*i.e.*, Hall et al., 2012) on the coincident NH EASE-Grids 2.0 at a 3.125 km rSIR grid cell spacing. We then  
684 derive melt onset and surface freeze-up dates ~~(2015–2019)~~ for each rSIR grid cell using the methodology  
685 described in Miller et al., (2020). We set a threshold of ice surface temperature  $> -1^\circ\text{C}$  for meltwater  
686 detection (Nghiem et al., 2012), consistent with the  $\pm 1^\circ\text{C}$  accuracy of the ice surface temperature  
687 observations data. For temperatures that are close to  $0^\circ\text{C}$ , ice surface temperatures are closely compatible  
688 with contemporaneous NOAA near-surface air temperature data observations (Shuman et al., 2014). Melt  
689 onset and surface freeze-up dates are overlaid on  $T_V^B$  time series to partition the melting and freezing  
690 seasons. Melt onset dates typically occur between ~~–~~April and July, and surface freeze-up dates typically  
691 occur between ~~–~~July and September. The melting season increases in duration moving downslope from  
692 the dry snow facies, and ranges from a single day in the highest elevations ( $>2500$  m) of the percolation  
693 facies, to ~~–~~150 days in the ablation facies. Similarly, the ~~associated~~ freezing season decreases in duration  
694 moving downslope, and ranges from between ~~–~~215 days and 365 days.

695 **▲**

696 ~~Over perennial firn aquifer areas (e.g., Figs. 1c; 2a; 4a),  $T_V^B$  is radiometrically warm during the~~  
697 ~~melting season. Vertically percolating meltwater and gravity driven meltwater drainage seasonally~~  
698 ~~recharges perennial aquifers at depth (Fountain and Walder et al., 1998). Maximum values range from~~  
699 ~~between 200 K and 275 K during seasonal surface melting. Temporal L-band signatures exhibit increases~~  
700 ~~on time scales of days to weeks following the melt onset date, and melting seasons range from between~~  
701 ~~75 and 100 days.  $T_V^B$  remains radiometrically warm during the freezing season as a result of latent heat~~  
702 ~~continuously released by the slow refreezing of the deeper firn layers that are saturated with large~~  
703 ~~volumetric fractions of meltwater (Miller et al., 2020). Minimum values range from between 180 K and 250~~

Formatted: Not Highlight

Formatted: Not Highlight

Formatted: Not Highlight

Formatted: Not Highlight

Formatted: Not Highlight

Formatted: Not Highlight

Formatted: Not Highlight

Formatted: Not Highlight

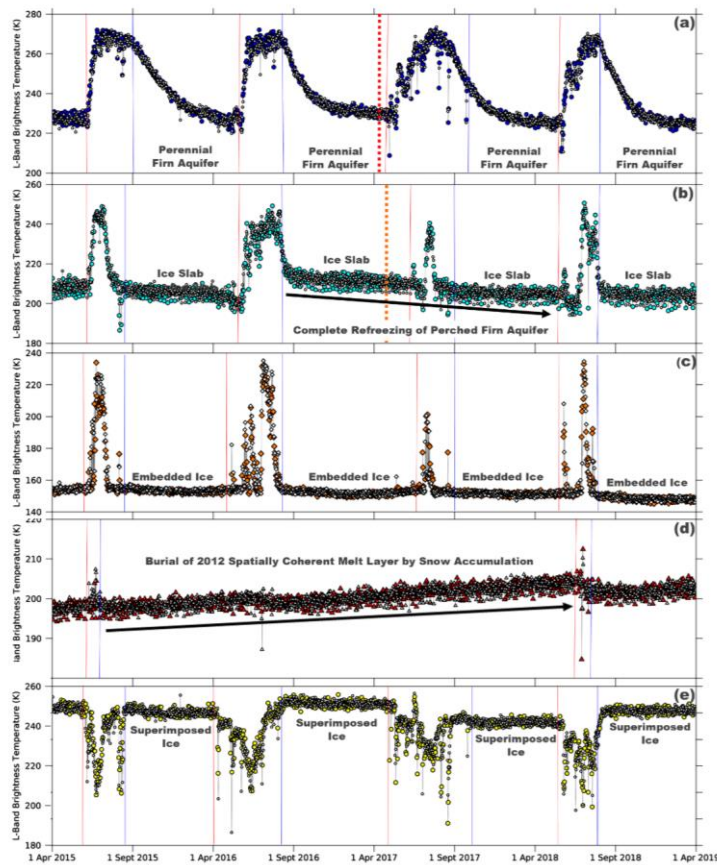
Formatted: Not Highlight

Formatted: Not Highlight

Formatted: Not Highlight

Formatted: Font: Bold, Font color: Red

704 ~~K following the surface freeze-up date. L-band emissions from the radiometrically warm upper snow and~~  
705 ~~firn layers decrease during the freezing season as embedded ice structures slowly refreeze at increased~~  
706 ~~depths below the ice sheet surface (Miller et al., 2020). Temporal L-band signatures exhibit exponential~~  
707 ~~decreases on time scales of months that approach and sometimes achieve relatively stable  $T_{\text{eff}}^{\text{L}}$  values,~~



708

709 **Figure 4**

710 Temporal L-band signatures that alternate morning (white symbols) and evening (colored symbols) orbital  
 711 pass interval enhanced resolution  $T_{\text{E}}^{\text{B}}$  generated using observations collected over the GRIS by the  
 712 microwave radiometer on the SMAP satellite (Brodzik et al., 2019) over (a) perennial firn aquifer area (blue  
 713 circles; Figs. 2a; 3a), (b) perched firn aquifer area (cyan circles; Figs. 2b; 3b), (c) percolation facies area  
 714 (orange diamonds; Fig. 2b), (d) high-elevation (~2500 m.a.s.l.) spatially coherent melt layer area (red  
 715 triangles; Fig. 2a), and (e) superimposed ice area (yellow circles; Fig. 2b). Melt onset (red lines) and surface  
 716 freeze-up (blue lines) dates are derived from thermal infrared  $T_{\text{E}}^{\text{B}}$  collected by MODIS on the Terra and  
 717 Aqua satellites (Hall et al., 2012). AR radargram profile along perennial firn aquifer transect A-B (red dashed  
 718 line; Figs. 1; 2a; 3a) that was collected on 22-April-2017, and ice slab transect C-D (orange dashed line;  
 719 Figs. 1; 2b; 3b) that was collected on 5-May-2017.

720 Over perennial firn aquifer areas (e.g., Fig. 4a, SMAP Test Site A: 66.2115°N, 39.1795°W, 1625 m  
721 a.s.l.), maximum  $T_V^B$  ( $T_{V,max}^B$ ) values are radiometrically warm during the melting season. Vertically  
722 percolating meltwater and gravity-driven meltwater drainage seasonally recharges perennial firn aquifers  
723 at depth (Fountain and Walder et al., 1998). Minimum Maximum values range from between ~200 K and  
724 275 K during seasonal surface melting. Temporal L-band signatures exhibit increases on time scales of  
725 ~days to weeks following the melt onset date, and melting seasons range from between ~75 and 100 days.  
726  $T_V^B$  ( $T_{V,min}^B$ ) values remain radiometrically warm during the freezing season as a result of latent heat  
727 continuously released by the slow refreezing of the deeper firn layers that are saturated with large  
728 volumetric fractions of meltwater (Miller et al., 2020). Minimum values range from between ~180 K and 250  
729 K following the surface freeze-up date. L-band emissions from the radiometrically warm upper snow and  
730 firn layers decrease during the freezing season as embedded ice structures slowly refreeze at increased  
731 depths below the ice sheet surface (Miller et al., 2020). Temporal L-band signatures exhibit slow  
732 exponential decreases, and on time scales of ~months that approach, and sometimes achieve, relatively  
733 stable  $T_V^B$  values, and freezing seasons range from between ~265-290 days.  $T_V^B$  can often decrease  
734 s by more than ~50 K during the freezing season (e.g., Fig. 4a), representing which represents the descent  
735 of the upper surface of stored meltwater by, meters to ~tens of meters (Miège et al., 2016).

736 Over ice slab and perched firn aquifer areas (e.g., Fig. 4b, SMAP Test Site B: 66.8850°N,  
737 42.7765°W, 1817 m a.s.l. e.g., Figs. 4c; 2b; 5b),  $T_V^B$  values are is typically radiometrically colder than  
738 over perennial firn aquifer areas during the melting season. The presence of dense low-permeability solid-  
739 ice layers (e.g., Fig. 3b) reduces the snow and firn pore space available to store seasonal meltwater at  
740 depth. Meltwater may alternatively run-off ice slabs downslope towards the wet snow facies.  $T_V^B$   
741 Maximum values range from between ~170 K and 260 K during seasonal surface melting. Temporal L-  
742 band signatures exhibit increases on time scales of ~days to weeks following the melt onset date, and  
743 melting seasons range from between ~60 and 90 days.  $T_V^B$  values are is also typically radiometrically colder  
744 than over perennial firn aquifer areas during the freezing season as a result of the absence of meltwater  
745 stored at depth (i.e. ice slab areas), or the presence of limited volumetric fractions of meltwater stored at  
746 depth in shallow water-saturated firn layers (i.e. perched firn aquifer areas). Minimum values range from  
747 between ~130 K and 240 K following the surface freeze-up date. Temporal L-band signatures exhibit  
748 exponential decreases that are slightly more rapid than over perennial firn aquifer areas, on time scales of  
749 ~weeks to months and often achieve relatively stable  $T_V^B$  values, and freezing seasons range from  
750 between ~275-305 days. Exponentially decreasing temporal L-band signatures sometimes transition to  
751 linearly decreasing on time scales of ~years following the surface freeze-up date (e.g., between  
752 ~September 2016 and May 2018 in Fig. 4b). We infer this indicates the formation and subsequent refreezing  
753 of a shallow perched firn aquifer on top of a buried ice slab or other semi-impermeable layer. As compared  
754 to the large  $T_V^B$  decreases in percolation facies areas,  $T_V^B$  decreases over perched firn aquifer areas are as  
755 small as ~a few K annually, which represents the descent of the upper surface of stored meltwater by  
756 ~meters rather than by ~tens of meters.

Formatted: Not Highlight

Formatted: Not Highlight

Formatted: Not Highlight

Formatted: Not Highlight

Formatted: Not Highlight

Formatted: Not Highlight

Formatted: Not Highlight

Formatted: Not Highlight

Formatted: Not Highlight

Formatted: Not Highlight

Formatted: Not Highlight

757 Over other percolation facies areas (e.g., Fig. 4c, SMAP Test Site C: 66.9024°N, 44.7528°W, 2350  
758 m a.s.l.), where seasonal meltwater is fully refrozen and stored exclusively as embedded ice,  $T_{V,max}^B$  (e.g.,  
759 Fig. 4c),  $T_V^B$  values are typically radiometrically colder than over perennial firn aquifer and ice slab, and  
760 perched firn aquifer areas during the melting season.  $T_{V,min}^B$  Maximum values range from between ~150 K  
761 and 200 K during seasonal surface melting. Temporal L-band signatures exhibit increases on time scales  
762 of days to weeks following the melt onset date, and melting seasons range from between ~1 and 60 days.  
763  $T_V^B$  values are also typically radiometrically cold during the freezing season. Minimum values range from  
764 between ~130 K and 180 K following the surface freeze-up date. Temporal L-band signatures exhibit rapid  
765 exponential decreases on time scales of days to weeks and achieve relatively stable  $T_V^B$  values, and  
766 freezing seasons range from between ~305-364 days. However, over the highest elevations (>~2500 m  
767 a.s.l.) of the percolation facies approaching the dry snow line, where seasonal surface melting and the  
768 formation of embedded ice structures is limited,  $T_{V,min}^B$   $T_V^B$  values remain radiometrically warm  
769 during the freezing season. Minimum values range from between ~180 K and 220 K following the surface  
770 freeze-up date. We infer  $T_V^B$  decreases, often sometimes step-responses exceeding ~10 K, that  
771 follow the surface freeze-up date (e.g., between April 2018 and September 2018 in Fig. 4c) are a result of  
772 an increase in volume scattering from newly formed embedded ice structures within a spatially coherent  
773 melt layer. We also infer that temporal L-band signatures that increase several K on time scales  
774 of years (e.g., between ~April 2015 and April 2018 in Fig. 4c) indicate the burial of spatially coherent melt  
775 layers formed following the 2010, 2012, 2015, and 2018 melting seasons by snow accumulation, formed  
776 following the 2010, 2012, 2015, and 2018 melting seasons by snow accumulation.

777 Exponentially decreasing temporal L-band signatures transition smoothly between perennial firn  
778 aquifer, ice slab, perched firn aquifer, and other percolation facies areas – there are no distinct  
779 temporal L-band signatures that delineate boundaries between these sub-facies. Boundary transitions  
780 between other facies the dry snow facies and the wet snow facies, however, are delineated both above and  
781 below the percolation facies. Over the dry snow facies (e.g., Fig. 4d, SMAP Test Site D: 66.3649°N,  
782 43.2115°W, 2497 m a.s.l.) e.g., Fig. 4d),  $T_{V,max}^B$ ,  $T_V^B$ , and  $T_{V,min}^B$  values are radiometrically warm during the  
783 melting and freezing seasons. Values range from between ~200 K and 240 K. While  $T_V^B$  is known to be  
784 relatively stable in the dry snow facies, temporal L-band signatures that increase on time scales of years  
785 are observed throughout this region the dry snow facies at elevations as high as Summit Station (~3200 m  
786 a.s.l.) and similar to those observed in the highest elevations (>~2500 m.a.s.l.) of the percolation facies.  
787 indicate the burial of the spatially coherent melt layer formed following the 2012 melting season (Nghiem  
788 et al., 2012), by snow accumulation (Culberg et al., 2021). We infer increasing temporal L-band signatures  
789 indicate the burial of the spatially coherent melt layer formed following the anomalous 2012 melting season  
790 (Nghiem et al., 2012) by snow accumulation (Culberg et al., 2021). Over the wet snow facies (e.g., Fig. 4e,  
791 SMAP Test Site E: 67.3454°N, 48.4789°W, 1469 m a.s.l.) e.g., Fig. 4e), where seasonal meltwater is fully  
792 refrozen and stored as superimposed ice,  $T_{V,max}^B$   $T_V^B$  values are radiometrically warm during the melting

Formatted: Space Before: 0 pt

Formatted: Not Highlight

Formatted: Not Strikethrough

Formatted: Not Highlight

Formatted: Font: Not Italic

Formatted: Not Highlight

Formatted: Not Highlight

Formatted: Font: 10 pt

Formatted: Not Highlight

Formatted: Font: 10 pt

Formatted: Not Highlight

Formatted: Font: 10 pt

Formatted: Not Highlight

Formatted: Font: 10 pt

Formatted: Not Highlight

Formatted: Not Highlight

794 ~~season~~season. Maximum values range from between ~~230 K and 250 K~~ during seasonal surface melting.  
 795 As compared to the percolation facies, where temporal L-band signatures exhibit rapid increases following  
 796 melt onset, temporal L-band signatures reverse and exhibit ~~rapid decreases on time scales of days to~~  
 797 ~~weeks, and melting seasons that range between 90-120 days. We infer these~~These reversals are the ~~a~~  
 798 result of high reflectivity and attenuation at the fully water-saturated snow layer and/or at the wet, rough  
 799 superimposed ice-air interface. Meltwater runs-off superimposed ice downslope towards the ~~ablation facies~~  
 800 ~~in the wet snow~~ablation facies.  ~~$T_{V,min}^B - T_V^B$  values~~ remains radiometrically warm during the freezing season.  
 801 ~~Minimum values range from between 230 K and 250 K following seasonal surface melting.~~Temporal L-  
 802 band signatures exhibit ~~rapid increases, on time scales of days that achieve~~and achieve relatively stable  
 803  ~~$T_V^B$  values, and freezing seasons range from between 245 and 275 days.~~

804 The MODIS-derived total number of days in the melting and freezing seasons estimated from melt  
 805 onset and surface freeze-up dates, the SMAP-derived maximum and minimum vertically-polarized L-band  
 806 brightness temperature, and the time scales of exponential decrease following the surface freeze-up date  
 807 estimated for each  ~~$T_V^B$  time series for rSIR grid-cells over perennial firn aquifer, ice slab, perched firn aquifer,~~  
 808 ~~and other percolation facies areas as well as for the dry snow facies, and the wet snow facies are~~  
 809 summarized in Table 2.

816 **Table 2.** ~~The MODIS-derived total number of days in the melting and freezing seasons (2015-2019), the~~  
 817 ~~SMAP-derived maximum vertically-polarized L-band brightness temperature ( $T_{V,max}^B$ ), the minimum~~  
 818 ~~vertically-polarized L-band brightness temperature ( $T_{V,min}^B$ ), and the time scale scales of exponential~~  
 819 ~~decrease following the surface freeze-up date (1 April 2015 – 31 March 2019) for perennial firn aquifer, ice~~  
 820 ~~slab, perched firn aquifer, and other percolation facies areas as well as for the dry snow facies and the wet~~  
 821 ~~snow facies.~~

	Melting Season (days)	Freezing Season (days)	$T_{V,max}^B$ (K)	$T_{V,min}^B$ (K)	Exponential Decrease (time-scale)
<b>Perennial Firn Aquifers</b>	-75 – 100	-265 – 290	-200 – 275	-180 – 250	-weeks – months
<b>Ice Slabs / Perched Firn Aquifers</b>	-60 – 90	-275 – 305	-170 – 260	-130 – 240	-days – Weeks
<b>Percolation Facies</b>	-1 – 60	-305 – 364	-150 – 200	-130 – 220	-days

Formatted: Not Highlight

Formatted: Not Highlight

Formatted: Not Highlight

Formatted: Not Highlight

Formatted: Not Highlight

Formatted: Not Highlight

Formatted: Not Highlight

Formatted: Not Highlight

Formatted: Widow/Orphan control, Tab stops: Not at 0" + 0.5"

Formatted: Font: 8 pt

Formatted: Font: 8 pt

Formatted: Font: 8 pt

Formatted: Font: 8 pt

Formatted: Font: 8 pt

Formatted: Font: 8 pt

Formatted: Font: 8 pt

Formatted: Font: 8 pt

Formatted: Font: 8 pt

Formatted: Font: 8 pt

Formatted: Font: 8 pt

<del>Dry Snow Facies</del>	-	365	-200-240	-200-240	-
<del>Wet Snow Facies</del>	-90-120	-245-275	-230-250	-230-250	-

Formatted: Font: 8 pt

Formatted: Font: 8 pt

822

Formatted: Font: Bold, Font color: Red

823

**2.34.23 L-band geophysical Two-Layer L-band Brightness Temperature Model**

Formatted: Space After: 5 pt

Formatted: Space Before: 5 pt, After: 5 pt

824

Based on our analysis of  $T_{V,max}^B$  of  $T_{V,min}^B$  and  $T_{V,max}^B$  and  $T_{V,min}^B$  values in temporal L-band signatures over the percolation facies (Section 2.3.1), we derive a 'firn saturation' parameter using the simple two-layer L-band geophysical-brightness temperature model (described in Ashcraft and Long, 2006; Miller et al., 2021, in press) (2006). The 'firn saturation' parameter is similar to the 'melt intensity' parameter derived in Hicks and Long (2011) that uses enhanced resolution vertically-polarized Ku-band radar backscatter imagery (2003) collected by the SeaWinds radar scatterometer that was flown in tandem on NASA's Quick SCATterometer (QuikSCAT) satellite (Tsai et al., 2000) and JAXA's Advanced Earth Observing Satellite 2 (ADEOS-II) (Freilich et al., 1994). We use the firn saturation parameter to estimate the maximum seasonal volumetric fraction of meltwater within the saturated upper snow and firn layers of the percolation facies using  $T_{V,max}^B$  and  $T_{V,min}^B$  values extracted from  $T_V^B$  time series (1 April 2015 – 31 March 2019). We calculate the firn saturation parameter for each rSIR grid cell within the ice sheet-masked extent of the GrIS as part of our adapted empirical algorithm (see Section 2.34.45).

Formatted: Not Highlight

Formatted: Not Highlight

825

826

827

828

829

830

831

832

833

834

835

836

837

838

839

840

841

842

843

844

845

846

847

Formatted: Not Highlight

Formatted: Not Highlight

Formatted: Not Highlight

~~We first describe the geophysical model as follows.~~ We assume a base layer underlying a water-saturated firn layer with a given depth and volumetric fraction of meltwater. Each of the layers is homogenous. ~~We next describe  $T_V^B$  from the geophysical model (Eq. 1).~~ The ice sheet is discretely layered (i.e., two layers; the base layer, and the water-saturated firn layer) to calculate  $T_V^B$  at an oblique incidence angle (Eq. 1). Emissions from the base layer ~~are is~~ a function of both the macroscopic roughness and the dielectric properties of the layer. ~~They It occurs~~ in conjunction with volume scattering at depth, and ~~are is~~ locally dependent on ~~englacial firn hydrological features, including~~ embedded ice structures, spatially coherent melt layers, ice slabs, and perennial ~~and perched~~ firn aquifers. Reflectivity at depth (i.e., at the base layer-water-saturated firn layer interface), and at the ice sheet surface (i.e., at the water-saturated firn layer-air interface) is neglected. The contribution from each layer is individually calculate ~~d, d~~.

The two-layer L-band geophysical-brightness temperature model is represented analytically by

Formatted: Space Before: 0 pt

848

$$T_{V,max}^B = T(1 - e^{-\kappa_e d \sec \theta}) + T_{V,min}^B e^{-\kappa_e d \sec \theta}, \quad \text{(Eq. 1)}$$

Formatted: Space Before: 5 pt, After: 5 pt, Line spacing: single

849

850

851

852

853

854

where  $T_{V,max}^B$  is the maximum vertically-polarized L-band brightness temperature at the ice sheet surface, and represents emission from the maximum seasonal volumetric fraction of meltwater stored within the water-saturated firn layer.  $T_{V,min}^B$  is the minimum vertically-polarized L-band brightness temperature emitted from the base layer.  $T$  is the physical temperature of the water-saturated firn layer,  $\theta$  is the transmission angle,  $\kappa_e$  is the extinction coefficient, and  $d$  is depth.

Formatted: Font:



855  
856  
857  
858  
859  
860  
861  
862  
863  
864  
865  
866  
867  
868  
869  
870  
871  
872  
873  
874  
875  
876  
877  
878

We invert Eq. 1 and solve for the firn saturation parameter ( $\xi$ )

$$\xi = \ln \left( \frac{T_{V,max}^B - T}{T_{V,min}^B - T} \right) \cos \theta , \quad \text{(Eq. 2)}$$

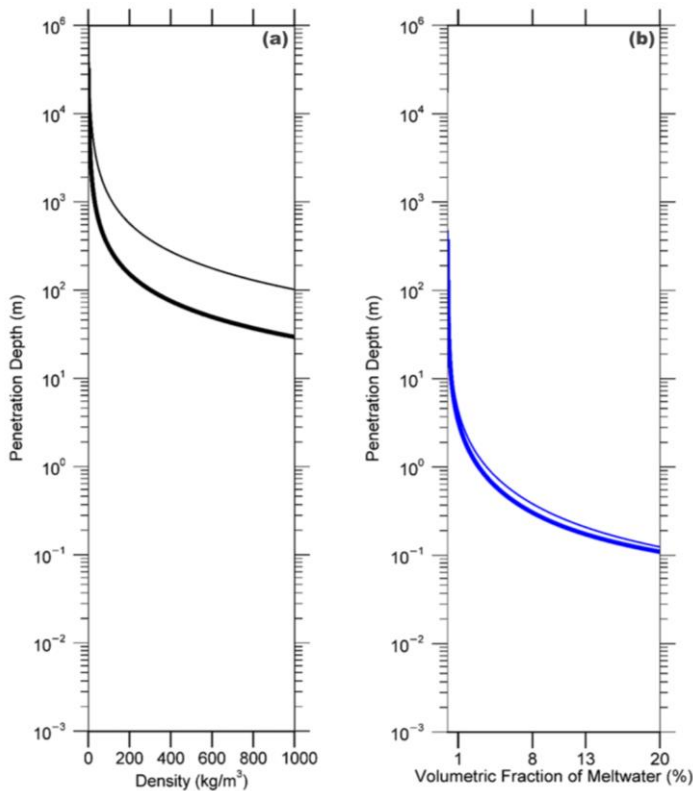
where  $\xi = \kappa_e d$ . The maximum vertically-polarized L-band brightness temperature asymptotically approaches the physical temperature of the water-saturated firn layer as the extinction coefficient and the depth of the water-saturated firn layer increases. For simplicity, we follow Jezek et al., (2015) and define the extinction coefficient as the sum of the Raleigh scattering coefficient ( $\kappa_s$ ) and the absorption coefficient ( $\kappa_a$ ). This assumes scattering from snow grains, which are small (millimeter scale) relative to the L-band wavelength (21 cm), and neglects Mie scattering from large (centimeter scale) embedded ice structures. However, The extinction coefficient is defined as the sum of the Raleigh scattering coefficient ( $\kappa_s$ ) and the absorption coefficient ( $\kappa_a$ ). For water-saturated firn, absorption dominates over scattering, and increases in the extinction coefficient are controlled by the volumetric fraction of meltwater ( $m_v$ ).

We assume that thicker water-saturated firn layers with larger volumetric fractions of meltwater generate higher firn saturation parameter values. However, the thickness of the water-saturated firn layer is limited by the L-band penetration depth. Theoretical L-band penetration depths calculated for a water-saturated firn layer range from between ~10 m for small volumetric fractions of meltwater ( $m_v < 1\%$ ), and ~1 cm for large volumetric fractions of meltwater ( $m_v = 20\%$ ) (Fig. 5). Large volumetric fractions of meltwater results in high reflectivity and attenuation at the water-saturated firn layer-air interface the interface between water-saturated firn layers and the overlying refrozen firn layers, and between glacial ice or a semi-impermeable layer and the overlying water-saturated firn layers, and a radiometrically cold firn layer (e.g., Fig. 5e).

Formatted: Space Before: 5 pt, After: 5 pt

Formatted: Not Highlight





879

880 **Figure 5**

881 *Theoretical L-band penetration depths for of uniform layer of (a) refrozen, and (b) water-saturated firn.*  
 882 *Penetration depths ( $\frac{4\pi}{\kappa_{\text{im}} + \kappa_{\text{ab}}}$ ) are calculated as a function of the Raleigh-scattering coefficient ( $\kappa_{\text{rs}}$ , Eq. 9) and*  
 883 *the absorption coefficient ( $\kappa_{\text{a}}$ , Eq. 10), which are functions of the dielectric and geophysical properties of*  
 884 *the GrlS. The complex dielectric constant is calculated using the empirically derived models described in*  
 885 *Tiuri et al., (1984). Refrozen firn penetration depths are calculated as a function of firn density ( $\rho_{\text{firn}}$ ), and*  
 886 *the curves are plotted for snow grain radii ( $r$ ) set to  $r=0.5$  mm (upper curve), and  $r=4$  mm (lower curve).*  
 887 *Water saturated firn penetration depths are calculated as a function of the volumetric fraction of meltwater*  
 888 *( $m_{\text{w}}$ ), and the curves are plotted for firn density set to  $\rho_{\text{firn}}=400$  kg/m<sup>3</sup> (upper curve), and  $\rho_{\text{firn}}=917$  kg/m<sup>3</sup>*  
 889 *(lower curve). Given the complexity of modeling embedded ice structures, they are excluded from the*  
 890 *penetration depth calculation. Increases in the volumetric fraction of embedded ice in the firn will result in*  
 891 *an increase in volume scattering, which will decrease and compress the distance between the penetration*  
 892 *depth curves for both refrozen and water saturated firn.*

Formatted: Strikethrough

## 2.34.34 Continuous Logistic Model

We adapt our previously developed empirical algorithm to map the extent of Greenland's perennial firn aquifers (Miller et al., 2020) to also map the extent of ice slab ~~and perched firn aquifer~~ areas. The empirical algorithm is derived from the continuous logistic model, which is based on a differential equation that models the decrease in physical systems as a function of time using a set of sigmoidal curves. These curves begin at a maximum value with an initial interval of decrease that is approximately exponential. Then, as the function approaches its minimum value, the decrease slows to approximately linear. Finally, as the function asymptotically reaches its minimum value, the decrease exponentially tails off and achieves stable values. We use the continuous logistic model to parametrize the refreezing rate within the ~~water~~-saturated upper snow and firn layers of the percolation facies using  $T_V^B$  time series ~~(1 April 2015 – 31 March 2019)~~ that are partitioned using  $T_{V,max}^B$  and  $T_{V,min}^B$  values. We calculate the refreezing rate for each rSIR grid cell within the percolation facies extent as part of our adapted empirical algorithm (see Section 2.34.45).

The continuous logistic model is described by a differential equation known as the logistic equation

$$\frac{dx}{dt} = \zeta x(1 - x)$$

(Eq. 3)

that has the solution

$$x(t) = \frac{1}{1 + \left(\frac{1}{x_0} - 1\right)e^{-\zeta t}},$$

(Eq. 4)

where  $x_0$  is the function's initial value,  $\zeta$  is the function's exponential rate of decrease, and  $t$  is time. The function  $x(t)$  is also known as the sigmoid function. We use the sigmoid function to model the exponentially decreasing temporal L-band signatures observed over the percolation facies as a set of decreasing sigmoidal curves.

We first normalize  $T_V^B$  time series for each rSIR grid cell

$$T_{V,N}^B(t) = \frac{T_V^B(t) - T_{V,min}^B}{T_{V,max}^B - T_{V,min}^B},$$

(Eq. 5)

where  $T_{V,min}^B$  is the minimum vertically-polarized L-band brightness temperature, and  $T_{V,max}^B$  is the maximum vertically-polarized L-band brightness temperature. We then apply the sigmoid fit

$$T_{V,N}^B(t \in [t_{max}, t_{min}]) = \frac{1}{1 + \left(\frac{1}{T_{V,N}^B(t_{max})} - 1\right)e^{-\zeta t}}.$$

(Eq. 6)

Formatted: Not Highlight

Formatted: Not Highlight

Formatted: Not Highlight

Formatted: Space Before: 5 pt, After: 5 pt, Line spacing: single

Formatted: Space Before: 5 pt, After: 5 pt, Line spacing: single

Formatted: Space Before: 5 pt, After: 5 pt, Line spacing: single

Formatted: Space Before: 5 pt, After: 5 pt, Line spacing: single

925  $T_{V,N}^B(t \in [t_{max}, t_{min}])$  is the normalized vertically-polarized L-band brightness temperature on the time  
 926 interval  $t \in [t_{max}, t_{min}]$ , where  $t_{max}$  is the time the function achieves a maximum value, and  $t_{min}$  is the  
 927 time the function achieves a minimum value. The initial normalized vertically-polarized L-band brightness  
 928 temperature ( $T_{V,N}^B(t_{max})$ ) is the function's maximum value. The final normalized vertically-polarized L-band  
 929 brightness temperature ( $T_{V,N}^B(t_{min})$ ) is the function's minimum value. The function's exponential rate of  
 930 decrease represents the refreezing rate parameter ( $\zeta$ ). An example set of simulated sigmoidal curves is  
 931 shown in Fig. 6.

Formatted: Right: 0.06", Space Before: 5 pt, After: 5 pt, Line spacing: single

Formatted: Not Highlight

### 2.34.45 ~~SMAP-Derived Perennial Firn Aquifer and Ice Slab, and perched firn aquifer Mappings~~

937 Our adapted empirical algorithm uses ice sheet-masked SMAP enhanced-resolution  $T_{V,N}^B$  imagery over the  
 938 GRIS that alternates morning and evening orbital pass observations annually, beginning and ending just  
 939 prior to melt onset. Our adapted empirical algorithm is implemented in two steps: (1) mapping the extent of  
 940 the percolation facies using the firn saturation parameter derived from the simple two-layer L-band  
 941 geophysical-brightness temperature model (see Section 2.34.23), and (2) mapping the extent of perennial  
 942 firn aquifer and ice slab, and perched firn aquifer areas over the percolation facies using the continuous  
 943 logistic model (see Section 2.34.34) we calibrate using airborne ice-penetrating radar detections surveys  
 944 (Section 2.2), projected on three separate NH EASE-Grids 2.0 (see Section 2.2).

Formatted: Not Highlight

Formatted: Not Highlight

Formatted: Not Highlight

Formatted: Space Before: 5 pt, After: 5 pt

Formatted: Not Highlight

Formatted: Not Highlight

Formatted: Not Highlight

Formatted: Not Highlight

Formatted: Not Highlight

Formatted: Not Highlight

Formatted: Not Highlight

945 Using Eq. 2, we first set a threshold for the firn saturation parameter ( $\xi_T$ ) defined by the relationship

$$947 \xi_T = (\kappa_s + \kappa_a)d \leq \xi .$$

(Eq. 7)

Formatted: Space Before: 5 pt, After: 5 pt, Line spacing: single

949 We calculate the Raleigh scattering coefficient ( $\kappa_s$ ) in Eq. 7 using

$$951 \kappa_s = N_d \frac{8}{3} k_o^4 r^6 \left| \frac{\epsilon_r - 1}{\epsilon_r + 2} \right|^2 ,$$

(Eq. 8)

Formatted: Space Before: 5 pt, After: 5 pt, Add space between paragraphs of the same style, Line spacing: single, Don't adjust space between Latin and Asian text, Don't adjust space between Asian text and numbers, Tab stops: Not at 0.56"

Formatted: Space Before: 5 pt, After: 5 pt, Line spacing: single

953 where  $N_d$  is the particle density,  $k_o$  is the wave number of the background medium of air,  $r$  is the snow  
 954 grain radius set to  $r=2$  mm, and  $\epsilon_r$  is the complex dielectric constant. The particle density is defined by

$$956 N_d = \frac{\rho_{firn}}{\rho_{ice}} \frac{1}{\frac{4}{3}\pi r^3} ,$$

(Eq. 9)

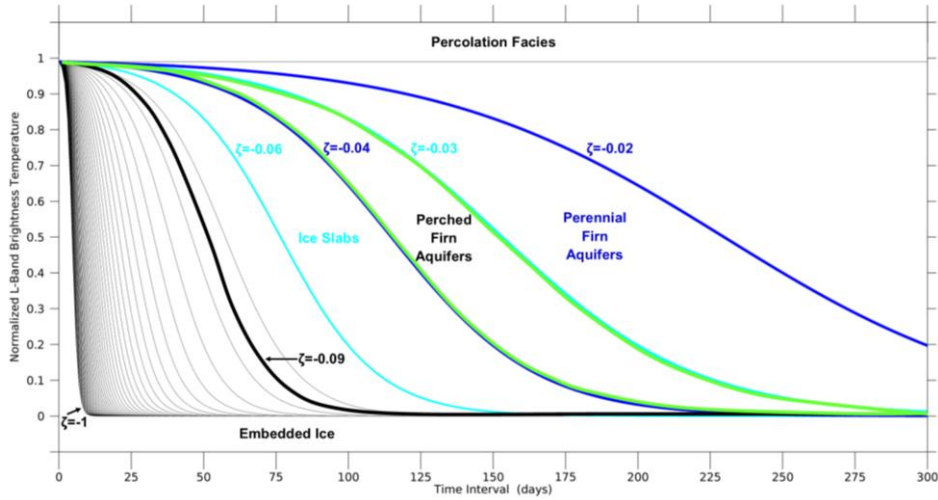
Formatted: Space Before: 5 pt, After: 5 pt, Line spacing: single

Formatted: Font: 10 pt

Formatted: Space Before: 5 pt, Line spacing: single

958 where  $\rho_{firn}$  is firn density, which we set to  $\rho_{firn}=400 \text{ kg/m}^3$ , and  $\rho_{ice}$  is ice density, which we set to  $\rho_{ice}=917$   
 959  $\text{kg/m}^3$ . Our grain radius and firn density estimates are consistent with measurements within the upper snow  
 960 and firn layers of the percolation facies of south eastern Greenland at the Helheim Glacier field site (Fig.

961



962

963

**Figure 6**

964 *Example set of simulated sigmoidal curves that represent our model of the exponentially decreasing*  
 965 *temporal L-band signatures predicted over the percolation facies. The initial normalized vertically polarized*  
 966 *L-band brightness temperature was fixed at a value of  $T_{v,p}^B(t_{min}) = 0.99$ , and the time interval was set to a*  
 967 *value of  $t \in [t_{max}, t_{min}] = 300$  observations. The refreezing rate parameter was set to values between  $\zeta =$*   
 968  *$[-1, 0]$  incremented by steps of 0.02. The blue lines correspond to the interval  $\zeta \in [-0.04, -0.02]$  and*  
 969 *produce curves similar to those observed over perennial firn aquifer areas. The cyan lines correspond to*  
 970 *the interval  $\zeta \in [-0.06, -0.03]$  and produce curves similar to those observed over ice slab areas. The green*  
 971 *lines correspond to the interval  $\zeta \in [-0.04, -0.03]$  and produce curves similar to those observed over*  
 972 *perched firn aquifer areas. The black line is the observed lower bound ( $\zeta = -0.09$ ) of the refreezing rate*  
 973 *parameter of partitioned  $T_{v,p}^B$  time series (1 April 2015 – 31 March 2019) iteratively fit to the sigmoid function*  
 974 *(see Section 3).*

975

976  $2a_r$ ; blue circle; Fig. 4a), where in situ perennial firn aquifer measurements have recently been collected  
977 (Miller et al., 2017).

Formatted: Not Highlight

978 We calculate the absorption coefficient ( $\kappa_a$ ) in Eq. 7 using

Formatted: Space After: 0 pt

979

$$980 \kappa_a = -2k_o \Im\{\sqrt{\epsilon_r}\}, \quad (\text{Eq. 10})$$

Formatted: Space Before: 5 pt, After: 5 pt

981

982 where  $\Im\{\}$  represents the imaginary part. We calculate the complex dielectric constant of the water-  
983 saturated firn layer in Eq. 8 and Eq. 10 using the empirically derived models described in Tiuri et al., (1984).

Formatted: Space Before: 5 pt, After: 5 pt, Don't add space between paragraphs of the same style, Tab stops: 0.56", Left

984 We set the volumetric fraction of meltwater to  $m_v=1\%$ . We set the depth of the water-saturated firn layer in  
985 Eq. 7 to  $d=1$  m. These values are consistent with typical lower frequency (e.g., 37 GHz, 13.4 GHz, 19 GHz)  
986 passive (e.g., Mote, et al. 1995; Abdalati and Steffen, 1997; Ashcraft and Long, 2006) and active (e.g.,  
987 Hicks and Long, 2011) microwave algorithms used to detect seasonal surface melting over the GrIS. Using  
988 the results of Eq. 7, 8, 9, and 10, we calculate the firn saturation parameter threshold at  $\xi_r=0.1$ .

989 The first step in our adapted empirical algorithm is to map the extent of the percolation facies. For  
990 each rSIR grid cell within the ice sheet-masked extent of the GrIS, we smooth the corresponding  $T_V^B$  time  
991 series s (1 April 2015 – 31 March 2019) using a 14-observation (1 week) moving window. We extract the  
992 minimum vertically-polarized L-band brightness temperature ( $T_{V,min}^B$ ), and the maximum vertically-polarized  
993 L-band brightness temperature ( $T_{V,max}^B$ ). We set the physical temperature of the water-saturated firn layer  
994 to  $T=273.15$  K, and the transmission angle to  $\theta=40^\circ$ . We then calculate the firn saturation parameter ( $\xi$ )  
995 using Eq. 2. If the calculated firn saturation parameter exceeds the firn saturation parameter threshold, the  
996 rSIR grid cell is converted to a binary parameter to map the total extent of the percolation facies.

997 We note that smoothing  $T_V^B$  time series will mask brief low-intensity seasonal surface melting that  
998 occurs in the high-elevation ( $>2500$  m) percolation facies, where seasonal meltwater is rapidly refrozen  
999 within the colder snow and firn layers (e.g., Fig. 4d). Thus, the calculated firn saturated parameter will not  
1000 exceed the firn saturation parameter threshold, and these rSIR grid cells will be excluded from the algorithm.  
1001 The exclusion of rSIR grid cells in the high-elevation percolation facies is not expected to have a significant  
1002 impact on our results as our algorithm targets rSIR grid cells in areas that experience intense seasonal  
1003 surface melting. The exclusion of rSIR grid cells will, however, slightly underestimate the mapped  
1004 percolation facies extent.

1005 The second step in our adapted empirical algorithm is to map the extent of perennial firn aquifer  
1006 and ice slab, and perched firn aquifer areas over the percolation facies. For each rSIR grid cell within the  
1007 mapped percolation facies extent, we normalize the corresponding  $T_V^B$  time series time series (1 April 2015  
1008 – 31 March 2019) using Eq. 5 ( $T_{V,N}^B(t)$ ) using Eq. 5. We then extract the initial normalized vertically-polarized  
1009 L-band brightness temperature ( $T_{V,N}^B(t_{max})$ ) and the final normalized vertically-polarized L-band brightness  
1010 temperature ( $T_{V,N}^B(t_{min})$ ) and partition  $T_{V,N}^B(t)$  on the time interval  $t \in [t_{max}, t_{min}]$ . We smooth  
1011  $T_{V,N}^B(t \in [t_{max}, t_{min}])$  using a 56-observation (4 week) moving window. The sigmoid fit is then iteratively

1012 applied using Eq. 6. Smoothing reduces the chi-squared error statistic when fitting  $T_{V,N}^B(t \in [t_{max}, t_{min}])$  to  
1013 the sigmoid function. We fix the initial normalized vertically-polarized L-band brightness temperature at  
1014  $T_{V,N}^B(t_{max})=0.99$ , which provides a uniform parameter space in which the refreezing rate parameter ( $\zeta$ ) can  
1015 be analyzed. Variability in  $T_{V,N}^B(t_{max})$  is controlled by the volumetric fraction of meltwater within the upper  
1016 snow and firn layers of the percolation facies, and is accounted for in the firn saturation parameter ( $\xi$ ), which  
1017 is analyzed separately.  $T_{V,N}^B(t \in [t_{max}, t_{min}])$  iteratively fit to the sigmoid function converge quickly (i.e.,  
1018 algorithm iterations  $I \in [5, 15]$ ), and observations are a good fit (i.e., chi squared error statistic is  $\chi^2 \in [0,$   
1019  $0.1]$ ).

1020 Using the SMAP-derived  $T_{V,N}^B(t_{max})$  and  $T_{V,N}^B(t_{min})$ , rather than the MODIS-derived initial  
1021 normalized vertically-polarized L-band brightness temperature at the surface freeze-up date ( $T_{V,N}^B(t_{sfu})$ ),  
1022 and final normalized vertically-polarized L-band brightness temperature at the melt onset date ( $T_{V,N}^B(t_{mo})$ )  
1023 that were used in the empirical algorithm described in Miller et al., 2020 (e.g., Fig. 4), has several  
1024 advantages. The key advantage of this approach is that maps can be generated using  $T^B$  imagery  
1025 collected from a single satellite, which simplifies the our adapted empirical algorithm. Another advantage is  
1026 that unlike  $T^B$  collected at shorter-wavelength thermal infrared frequencies (e.g., MODIS),  $T^B$  collected at  
1027 longer wavelength microwave frequencies (e.g., SMAP) is not sensitive to clouds, which eliminates  
1028 observational gaps and cloud contamination, and provides more accurate time series partitioning and more  
1029 robust curve fitting. ~~The mapped extent of Greenland's perennial firn aquifers generated by our adapted~~  
1030 ~~empirical algorithm and by our empirical algorithm (Miller et al., 2020) are consistent (see Section 3).~~

1031 We calibrate our adapted empirical algorithm using the AR- and MCoRDS-derived perennial firn  
1032 aquifer (2010-2017) and ice slab (2010-2014), and perched firn aquifer (2010-2017) detections projected  
1033 separately on the three-NH EASE-Grids 2.0. For each rSIR grid cell with at least one detection, we extract  
1034 the corresponding correlated maximum vertically-polarized L-band brightness temperature ( $T_{V,max}^B$ ), the  
1035 minimum vertically-polarized L-band brightness temperature ( $T_{V,min}^B$ ), the firn saturation parameter ( $\xi$ ), and  
1036 the refreezing rate parameter ( $\zeta$ ), and for each of the extracted SMAP-derived calibration parameters,  
1037 we calculate the standard deviation ( $\sigma$ ). ~~Thresholds similar to Miller et al., 2020, thresholds~~ of  $\pm 2\sigma$  are set  
1038 ~~for each of the extracted SMAP-derived calibration parameters~~ in an attempt to eliminate peripheral rSIR  
1039 grid cells near the ice sheet edge and near ~~the the upper and lower~~ boundaries of each sub-facies, where  
1040 ~~where~~ L-band emissions can be influenced by morphological features, such as crevasses, superimposed  
1041 and glacial ice, and spatially integrated with emissions from rock, land, the ocean, and adjacent percolation  
1042 facies and wet snow facies areas. ~~The SMAP-derived calibration parameter threshold intervals extracted~~  
1043 ~~from  $T_{V,N}^B$  time series that we use to map perennial firn aquifer, ice slab, and perched firn aquifer areas~~ are  
1044 given in Table 23. We apply the calibration to each rSIR grid cell within the percolation facies extent. If the  
1045 extracted ~~SMAP-derived~~ calibration parameters are within the ~~threshold~~ intervals, the rSIR grid cell is  
1046 converted to a binary parameter to map the total extent of each of these sub-facies.

Formatted: Not Highlight

Formatted: Not Highlight

Formatted: Not Highlight

Formatted: Not Highlight

Formatted: Not Highlight

1048  
1049  
1050

**Table 3.** SMAP-derived calibration parameter threshold intervals (1 April 2015 – 31 March 2019) used for mapping perennial firn aquifer, ice slab, and perched firn aquifer areas.

	$\xi$	$T_{V,max}^B$ (K)	$T_{V,min}^B$ (K)	$\zeta$
<b>Perennial Firn Aquifers</b>	0.2 – 4	200 – 275	180 – 250	-0.04 – 0.02
<b>0.1 – 2</b>	170 – 260	130 – 240	-0.03 – 0.06	
<b>Perched Firn Aquifers</b>	0.2 – 1.2	200 – 260	180 – 240	-0.03 – 0.04

1051

1052 Iteratively applying the sigmoid fit to  $T_{V,N}^B(t \in [t_{max}, t_{min}])$  over perched firn aquifer areas is a  
 1053 source of uncertainty in our adapted empirical algorithm. While the continuous logistic model is reasonable  
 1054 for the majority of exponentially decreasing temporal L-band signatures over the percolation facies, it is not  
 1055 optimal for exponentially decreasing temporal L-band signatures that transition to linearly decreasing on  
 1056 time scales of ~years following the surface freeze-up date. Especially multi-year linearly decreasing  
 1057 temporal L-band signatures over areas where perching occurs following intense seasonal surface melting  
 1058 and shallow water-saturated firn layers persist throughout the following freezing season as well as  
 1059 throughout weaker seasonal surface melting the following melting season (e.g., between ~September 2016  
 1060 and May 2018 in Fig. 4b). Although  $T_{V,N}^B(t \in [t_{max}, t_{min}])$  over perched firn aquifer areas iteratively fit to  
 1061 the sigmoid function converge quickly (i.e., algorithm iterations  $l \in [8, 15]$ ), and observations appear to be  
 1062 a good fit (i.e., chi-squared error statistic is  $\chi^2 \in [0.06, 0.1]$ ), simulated sigmoidal curves often  
 1063 asymptotically approach  $T_{V,min}^B$  too quickly, which underestimates the refreezing rate parameter ( $\zeta$ ) to  
 1064 values outside the SMAP-derived calibration parameter threshold intervals. Perched firn aquifer areas may  
 1065 alternatively be mapped as ice slab areas or percolation facies areas, which will underestimate or  
 1066 overestimate the mapped extent of each of these sub-facies.

1067 Miller et al., 2020 cited significant uncertainty in the SMAP-derived perennial firn aquifer extent as  
 1068 a result of the lack of a distinct temporal L-band signature delineating the boundary between perennial firn  
 1069 aquifer areas and adjacent percolation facies areas. In this study, similar uncertainty exists in the SMAP-  
 1070 derived perennial firn aquifer and, ice slab, and perched firn aquifer extents. This uncertainty could, at least  
 1071 in part, be a result of the rSIR algorithm. An rSIR grid cell corresponds to the weighted average of  $T^B$  over  
 1072 SMAP's antenna footprint (Long et al., 2020). The weighting is the grid cell's spatial response function  
 1073 (SRF), which is approximately ~18 km (i.e., the effective resolution) in diameter. The SRF is centered on  
 1074 the rSIR grid cell. Since the effective resolution (i.e., the size of the 3-dB 3 dB contour of the SRF) is less  
 1075 than the rSIR grid cell spacing, rSIR grid cell SRF's overlap and the grid cells  $T^B$  values are not statistically  
 1076 independent. This uncertainty, however, could also have a geophysical basis, as it is unlikely that the  
 1077 boundaries between sub-facies (perennial firn aquifers, ice slabs, and perched firn aquifers) as well as  
 1078 between facies (percolation facies, dry snow facies, wet snow facies) are distinct. The thickness of the

Formatted: Not Highlight

1079 water-saturated firn layer or ice slab may thin and taper-off at the periphery, and sub-facies and facies may  
1080 become spatially scattered and merge together. ~~Over SMAP's ~18 km footprint, spatially integrated L-band~~  
1081 ~~emissions may also result in a smooth transition between temporal L-band signatures.~~

1082 The limited extent (AR, 15 m x 20 m; MCoRDS, 14 m x 40 m) of the airborne ice-penetrating radar  
1083 ~~detections surveys~~ as compared to the rSIR grid cell extent (3.125 km x 3.125 km) and the effective  
1084 resolution (~~~18 km~~) of the SMAP enhanced-resolution  $T_{V,A}^B$  imagery is also cited in Miller et al., 2020 as a  
1085 source of uncertainty in the empirical algorithm. In this study, similar uncertainty exists in our adapted  
1086 empirical algorithm. The total rSIR grid cell extent with ~~airborne ice-penetrating radar survey radargram~~  
1087 coverage is less than 2%. ~~Thus, which means that~~ ~98% of the total rSIR grid cell extent ~~with radargram~~  
1088 ~~coverage~~, from which the SMAP-derived calibration parameter ~~threshold~~ intervals are extracted, is  
1089 unknown. Calculating the total rSIR grid cell extent where detections are absent along OIB flight lines and  
1090 statistically integrating this calculation into the multi-year calibration technique may help reduce the  
1091 uncertainty, particularly the significant uncertainty in the interannual variability, ~~in extent~~, which we have yet  
1092 to resolve. A sensitivity analysis suggests that even small changes in ~~any of~~ the SMAP-derived calibration  
1093 parameter ~~threshold~~ intervals (i.e., several K for  $T_{V,min}^B$  and  $T_{V,max}^B$ , several tenths of a percentage point for  
1094  $\xi_v$  and several hundredths of a percentage point for  $\zeta$ ) can result in variability in the mapped extents of  
1095 hundreds of square kilometers, and boundary transitions between perennial firn aquifer, ~~and~~ ice slab, ~~and~~  
1096 ~~perched firn aquifer~~ areas. Thus, the mapped extent of each of these sub-facies ~~of the broader percolation~~  
1097 ~~facies~~ should simply be considered an initial result demonstrating the potential of our adapted empirical  
1098 algorithm for future work.

1101 ~~Similar to ice slabs, the formation of spatially coherent melt layers reduces the pore~~  
1102 ~~space within the upper snow and firn layers and may also facilitate lateral meltwater~~  
1103 ~~flow with minimum vertical percolation into the deeper firn layers, thus enhancing~~  
1104 ~~meltwater run-off from significantly higher elevations downslope towards the~~  
1105 ~~periphery on accelerated time scales. The formation of spatially coherent melt layers~~  
1106 ~~overlying deeper perennial firn aquifers (e.g., Fig. 3a) will limit or terminate gravity-~~  
1107 ~~driven meltwater drainage and seasonal recharging (Fountain and Walder, 1998),~~  
1108 ~~which may eventually completely refreeze stored meltwater into decimeters thick~~  
1109 ~~solid ice layers overlying deeper glacial ice.~~

### 1110 **3. Results and Discussion**

1111 The SMAP-derived maximum vertically-polarized L-band brightness temperature values generated by our  
1112 adapted empirical algorithm range from between  $T_{V,max}^B=150$  K and 275 K, and the minimum vertically-

Formatted: Font color: Auto

Formatted: Font color: Auto

Formatted: Font color: Auto

Formatted: Font color: Auto

Formatted: Not Highlight

Formatted: Not Highlight

Formatted: Font color: Auto

Formatted: Font color: Auto

Formatted: Font color: Auto

Formatted: Font color: Auto

Formatted: Not Highlight

Formatted: Font: Arial Black

Formatted: Space Before: 5 pt, After: 5 pt

Formatted: Font: 10 pt



1113 polarized L-band brightness temperature values range from between  $T_{V,min}^B=130$  K and 250 K. These values  
1114 are consistent with the range of  $T_{V,max}^B$  and  $T_{V,min}^B$  values given in the temporal L-band signature analysis  
1115 (Section 2.4.2; Table 12). Firn saturation parameter values range from between  $\xi=0.1$  and 4.0. Refreezing  
1116 rate parameter values range from between  $\zeta=-0.09$  and -0.01. The observed lower bound ( $\zeta=-0.09$ ) of the  
1117 refreezing rate parameter observed over the percolation facies is significantly higher than the predicted  
1118 lower bound ( $\zeta=-1$ ) in our example set of simulated sigmoidal curves (black line, Fig. 6).

1119 The SMAP-derived perennial firn aquifer r\_f (blue shading), ice slab (cyan shading), perched firn  
1120 aquifer (green shading), and percolation facies (purple shading) extents (2015-2019) are generated by our  
1121 adapted empirical algorithm are shown in Figs. 7a-9a, and are summarized in Table 4. The percolation  
1122 facies extent ( $\sim 5.8 \times 10^5$  km<sup>2</sup>) generated by our adapted empirical algorithm is mapped at elevations  
1123 between  $\sim 500$  m a.s.l. and 3500 m a.s.l., and extends over  $\sim 32\%$  of the GrIS extent ( $\sim 1.8 \times 10^6$  km<sup>2</sup>).  
1124 The perennial firn aquifer extent (64,000 km<sup>2</sup>) is mapped at elevations between  $\sim 600$  m a.s.l and 2600 m  
1125 a.s.l., and extends over  $\sim 11\%$  of the percolation facies extent and  $\sim 4\%$  of the GrIS extent. Predominately  
1126 high  $T_{V,max}^B$ ,  $T_{V,min}^B$ .

Formatted: Not Highlight

Formatted: Not Highlight

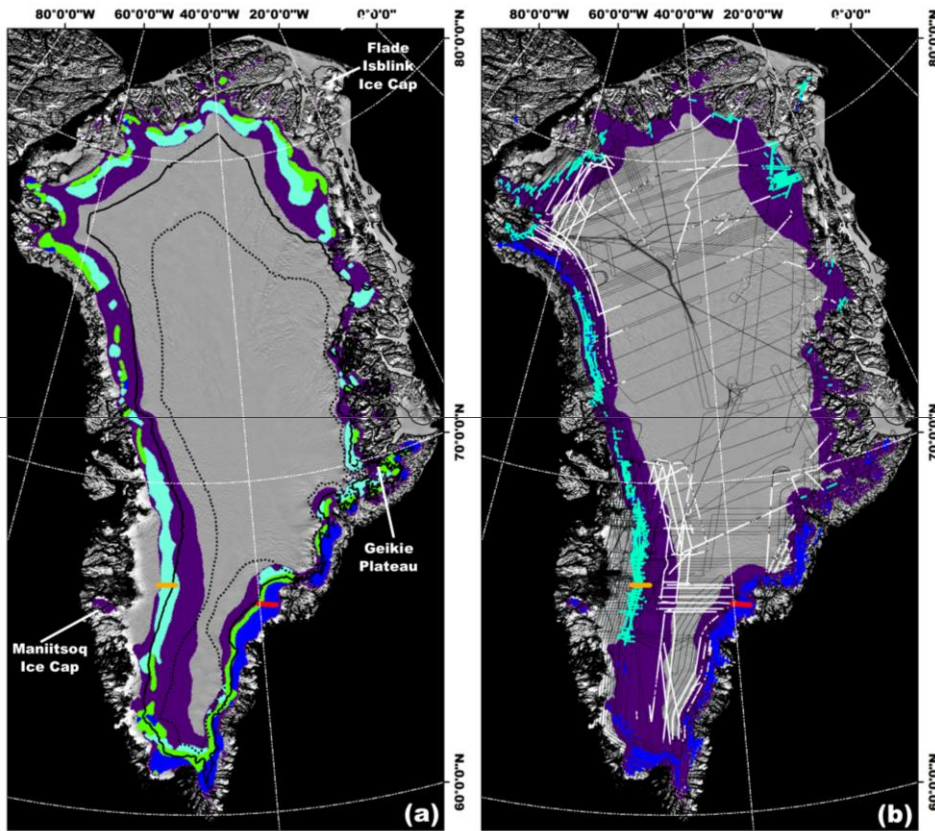
Formatted: Not Highlight

Formatted: Not Highlight

Formatted: Not Highlight

Formatted: Not Highlight

Formatted: Font:



1127

1128

**Figure 7**

1129

1130

1131

1132

1133

1134

1135

1136

1137

1138

(a) The SMAP-derived perennal firn aquifer (blue shading), ice slab (cyan shading), perched firn aquifer (green shading), and percolation facies (purple shading) extents (2015-2019) generated by the adapted empirical algorithm overlaid on the 2015 MODIS Mosaic of Greenland image map (Haran et al., 2018). The black line is the 2000 m.a.s.l. contour, and the black dotted line is the 2500 m.a.s.l. contour (Howat et al., 2014). (b) The SMAP-derived extents are overlaid with AR- and MCoRDS-derived 2010-2017 perennal firn aquifer (blue shading; Miège et al., 2016), 2010-2014 ice slab (cyan shading; McFerrinMacFerrin et al., 2019), and 2012 spatially coherent melt layer (white shading; Culberg et al., 2021) detections along OIB flight lines (black lines). Overlapping perennal firn aquifer and ice slab detections are interpreted as perched firn aquifer areas. The red line is AR radargram profile along perennal firn aquifer transect A-B (Fig. 3a). The orange line is AR radargram profile along ice slab transect C-D (Fig. 3b).



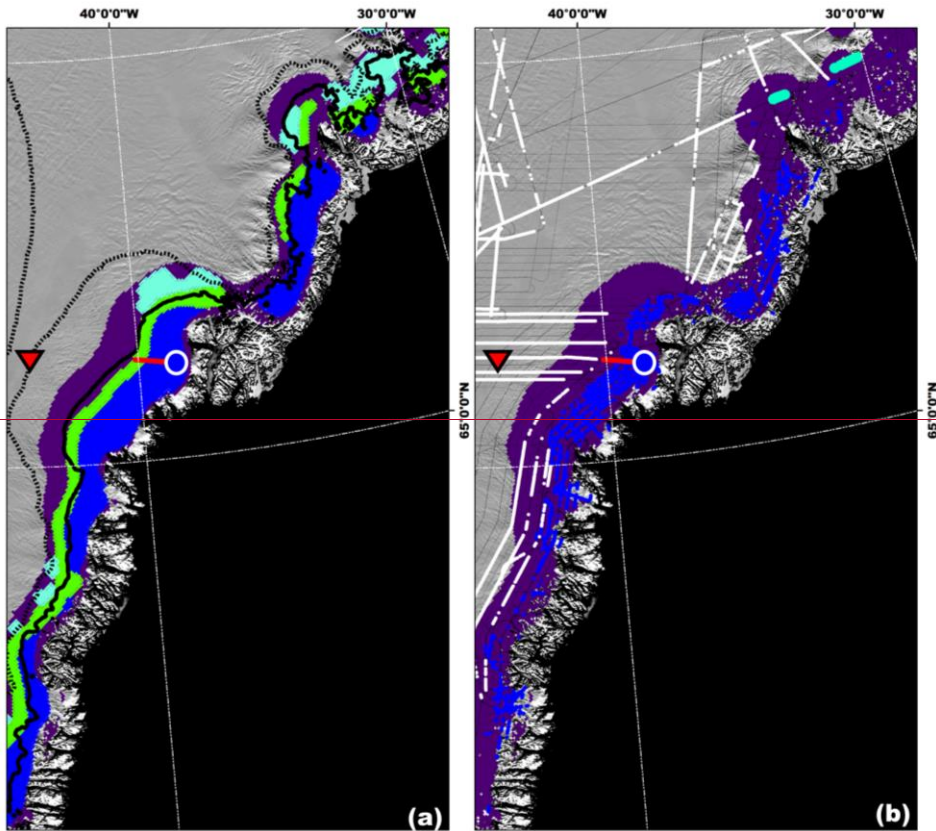


**Figure 8**

(a) The SMAP-derived perennial firn aquifer (blue shading), ice slab (cyan shading), perched firn aquifer (green shading), and percolation facies (purple shading) extents (2015-2019) generated by the adapted empirical algorithm over south eastern Greenland (Fig. 1c; zoom area in red box) overlaid on the 2015 MODIS Mosaic of Greenland image map (Haran et al., 2018). The solid black line is the 2000 m.a.s.l. contour, and the black dotted line is the 2500 m.a.s.l. contour (Howat et al., 2014). (b) The SMAP-derived percolation facies extent is overlaid with AR- and MCoRDS-derived 2010-2017 perennial firn aquifer (blue shading; Miège et al., 2016), 2010-2014 ice slab (cyan shading; McFerrinMacFerrin et al., 2019), and 2012 spatially coherent melt layer (white shading; Culberg et al., 2021) detections along OIB flight lines (black lines). Overlapping perennial firn aquifer and ice slab detections are interpreted as perched firn aquifer areas. The red line is AR radargram profile along perennial firn aquifer transect A-B (Figs. 1; 3a). The blue circle is a perennial firn aquifer area (Figs. 3a; 4a). The red triangle is a high-elevation (~2500 m.a.s.l.) percolation facies area (Figs. 4d).

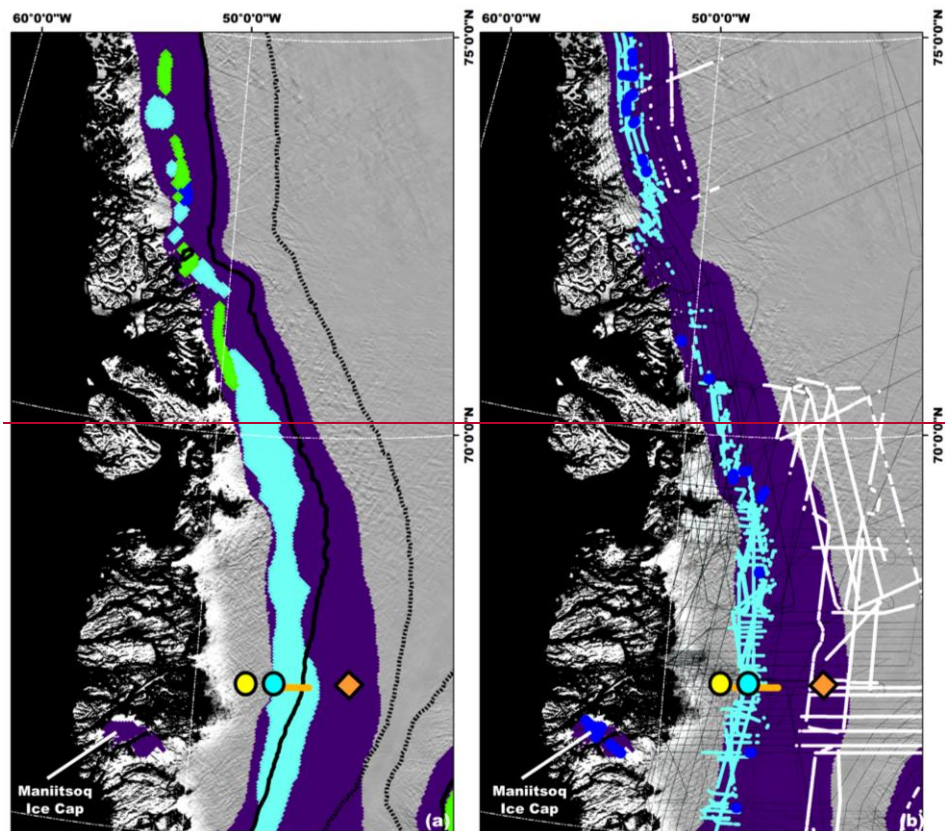


**Figure 9**

(a) The SMAP-derived perennal firn aquifer (blue shading), ice slab (cyan shading), perched firn aquifer (green shading), and percolation facies (purple shading) extents (2015-2019) generated by the adapted empirical algorithm over south western Greenland (Fig. 1c; zoom area in red box) overlaid on the 2015 MODIS Mosaic of Greenland image map (Haran et al., 2018). The solid black line is the 2000 m.a.s.l. contour, and the black dotted line is the 2500 m.a.s.l. contour (Howat et al., 2014). (b) The SMAP-derived percolation facies extent is overlaid with AR- and MCoRDS-derived 2010-2017 perennal firn aquifer (blue shading; Miège et al., 2016), 2010-2014 ice slab (cyan shading; McFerrinMacFerrin et al., 2019), and 2012 spatially coherent melt layer (white shading; Culberg et al., 2021) detections along OIB flight lines (black lines). Overlapping perennal firn aquifer and ice slab detections are interpreted as perched firn aquifer areas. The orange line is AR radargram profile along ice slab transect C-D ( Figs 1; 3b). The cyan circle is a perched firn aquifer area (Figs. 3b; 4b). The orange diamond is a percolation facies area (Fig. 4c). The yellow circle is a superimposed ice area (Fig. 4e).

1168  $\xi$ , and  $\zeta$  values mapped within the perennial firn aquifer extent indicates the widespread presence of thicker  
 1169 water-saturated firn layers with larger volumetric fractions of meltwater that are radiometrically warm during  
 1170 both the melting and freezing seasons, and have extended refreezing rates. The ice slab extent (76,000  
 1171 km<sup>2</sup>) is mapped at elevations between -800 m.a.s.l and 2700 m.a.s.l., and extends over ~13 % of the  
 1172 percolation facies extent, and ~4 % of the GrIS extent. As compared to perennial firn aquifer areas,  
 1173 decreased  $T_{V,max}^B$ ,  $T_{V,min}^B$ ,  $\xi$  and  $\zeta$  values in ice slabs areas indicates the presence of thinner water-  
 1174 saturated firn layers with lower volumetric fractions of meltwater that are radiometrically colder, and have  
 1175 slightly more rapid refreezing rates. ~~The SMAP-derived perched firn aquifer calibration parameter intervals~~  
 1176 ~~are within the perennial firn aquifer and the ice slab calibration parameter intervals (see Fig. 6, Table 3).~~  
 1177 ~~The extents of these three sub-facies within the broader percolation facies are overlapping, such that~~  
 1178 ~~perched firn aquifers typically represent the upper boundary of perennial firn aquifer areas that~~  
 1179 ~~subsequently transition to percolation facies as well as the lower boundary of ice slab areas that~~  
 1180 ~~subsequently transition to wet snow facies. However, in several areas in south and southeastern~~  
 1181 ~~Greenland, the full progression of facies and sub-facies (dry snow facies - percolation facies - ice slab -~~  
 1182 ~~perched firn aquifer - perennial firn aquifer - ablation facies) occur (e.g., Fig. 7a). The perched firn aquifer~~  
 1183 ~~extent (37,000 km<sup>2</sup>) is mapped at elevations between -600 m.a.s.l and 2700 m.a.s.l., and extends over~~  
 1184 ~~~30% of perennial firn aquifer extent, ~24% of ice slab extent, ~2% of the percolation facies extent, and~~  
 1185 ~~less than ~1% of the GrIS extent. Combined together, the total extent (~140,000 km<sup>2</sup>) is the equivalent of~~  
 1186 ~~~24% of the percolation facies extent, and 10% of the GrIS extent. The extents of these sub-facies are~~  
 1187 ~~generally isolated and somewhat scattered within the percolation facies. However, in several areas in south,~~  
 1188 ~~south and central eastern, and northern Greenland, the sequential formation of facies and sub-facies (dry~~  
 1189 ~~snow facies - percolation facies - ice slab - perennial firn aquifer - ablation facies) is mapped. This increases~~  
 1190 ~~previous AR- and MCoRDS-derived elevation estimates upslope ~600 m.a.s.l. in both perennial firn aquifer~~  
 1191 ~~areas (Miège et al., 2016) and ice slab areas (McFerrinMacFerrin et al., 2019).~~  
 1192 ~~The highest perennial firn aquifer, ice slab, and perched firn aquifer elevations (>2500 m.a.s.l.) are mapped~~  
 1193 ~~in southern Greenland and on the Geikie plateau, in central eastern Greenland.~~

Formatted: Not Highlight

Formatted: Not Highlight

Formatted: Not Highlight

Formatted: Not Highlight

Formatted: Not Highlight

Formatted: Not Highlight

Formatted: Font: English (United States)

1195 **Table 4.** ~~The SMAP-derived perennial firn aquifer, ice slab, and perched firn aquifer extents (2015-2019)~~  
 1196 ~~over the percolation facies and the GrIS, and the elevation range at which they are mapped.~~

	Percolation Facies Extent (%)	Ice Sheet Extent (%)	Elevation Range (m.a.s.l.)
Perennial Firn Aquifers	44	4	600—2600
Ice Slabs	43	4	800—2700
Perched Firn Aquifers	5	<1	600—2700

Formatted: Not Highlight



1198 Figs. 7b-9b shows perennial firn aquifers (blue shading), ice slabs, and spatially coherent melt  
 1199 layers (cyan shading), and spatially coherent melt layers (white shading) detected by airborne ice-  
 1200 penetrating radar surveys (2010-2017) overlaid on the SMAP-derived percolation facies extent (2015-  
 1201 2019). Perched firn aquifer areas are inferred where perennial firn aquifer and ice slab detections overlap.  
 1202 The SMAP-derived perennial firn aquifer extent mapped in southern, and south and central eastern  
 1203 Greenland is consistent with the AR- and MCoRDS-geophysical derived perennial firn aquifer detections  
 1204 (2010-2017), except in north-western Greenland where perched firn aquifers are alternatively mapped.  
 1205 Additional smaller perennial firn aquifer areas are mapped in northern Greenland. The SMAP-derived ice  
 1206 slab extent mapped in south western, and central eastern, central and north eastern, and northern  
 1207 Greenland is generally consistent with the spatial patterns of the AR-derived ice slab detections (2010-  
 1208 2014), however, is significantly significantly expanded upslope in each of each of these these areas. In  
 1209 northern Greenland, perennial firn aquifer areas are alternatively mapped, and additional expansive ice  
 1210 slab areas are mapped upslope of perennial firn aquifer areas. Additional smaller ice slab areas are mapped  
 1211 in south and south eastern (Figs. 9a; 9b) Greenland. We note that the AR- and MCoRDS-derived perennial  
 1212 firn aquifer and ice slab detections are limited in space and time, particularly in northern Greenland, with a  
 1213 time interval as large as nine years between the airborne ice-penetrating radar surveys and the SMAP  
 1214 enhanced-resolution  $T_v^{\beta}$  imagery we use in our adapted empirical algorithm. In western and northern  
 1215 Greenland, the 2015 melting season was especially intense (Tedesco et al., 2016). And, in northern  
 1216 Greenland, the ablation facies have recently (2010-2019) increased in extent (Noël et al., 2019), and  
 1217 supraglacial lakes have recently (2014-2019) advanced inland (Turton et al., 2021), indicating a possible  
 1218 geophysical basis for the observed formation, boundary transitions, and expansion. Neither perennial firn  
 1219 aquifer or ice slab areas are mapped on the Maniitsoq and Flade Isblink Ice Caps, where spatially integrated  
 1220 L-band emission results in calibration parameter values outside the defined intervals for each of these sub-  
 1221 facies.

1222 Although the AR-derived spatially coherent melt layers detections are often observed to be adjacent  
 1223 to perennial firn aquifer and ice slab areas, these sub-facies were masked in the original airborne ice  
 1224 penetrating radar survey analysis by Culberg et al., (2021). Spatially coherent melt layers often overlay  
 1225 perennial firn aquifers (e.g., Fig. 3a), and merge with ice slabs (Culberg et al., 2021; Fig.4). We note that  
 1226 the AR-derived ice slab detections are limited in space and time, particularly in northern Greenland, with a  
 1227 time interval as large as nine years between the airborne ice-penetrating radar surveys and the SMAP  
 1228 enhanced-resolution  $T_v^{\beta}$  imagery used in the adapted empirical algorithm (i.e., 2010 to 2019). In western  
 1229 and northern Greenland, the 2015 melting season was especially intense (Tedesco et al., 2016). And, in  
 1230 northern Greenland, the ablation facies have recently increased in extent (2010-2019; Noël et al., 2019),  
 1231 and supraglacial lakes have recently advanced inland (2014-2019; Turton et al., 2021), indicating a likely  
 1232 geophysical basis for the observed upslope expansion. In central and north eastern, and northern  
 1233 Greenland, perched firn aquifers are often alternatively mapped. Additional smaller ice slab areas are  
 1234 mapped in south and south eastern (Figs. 9a; 9b) Greenland. The scattered SMAP-derived perched firn

Formatted: Not Highlight

Formatted: Not Highlight

Formatted: Not Highlight

Formatted: Not Highlight

Formatted: Not Highlight

Formatted: Not Highlight

Formatted: Not Highlight

Formatted: Not Highlight

Formatted: Not Highlight

Formatted: Not Highlight

Formatted: Font:

Formatted: Not Highlight

Formatted: Indent: First line: 0.5"

Formatted: Not Highlight

Formatted: Not Highlight

Formatted: Not Highlight



1235 aquifer extent mapped in north western and central eastern Greenland is fairly consistent with the sparse  
1236 AR- and MCoRDS-derived perched firn aquifer detections (2010-2017), however, in central western  
1237 Greenland (Figs. 9a; 9b) ice slab areas are alternatively mapped. Expansive additional perched firn aquifer  
1238 areas are mapped in southern, and south and central eastern Greenland. These areas are often coincident  
1239 with spatially coherent melt layer detections, particularly in south eastern Greenland (Figs. 8a, 8b). Neither  
1240 perennial firn aquifer, ice slab, nor perched firn aquifer areas are mapped on the Maniitsoq and Flade Isblink  
1241 Ice Caps. Over these two small ice caps, L-band emissions spatially integrated with emissions from rock,  
1242 land, the ocean, and adjacent percolation facies and wet snow facies areas result in SMAP-derived  
1243 calibration parameter values outside the defined intervals for each of these sub-facies.

1244  
1245 \_\_\_\_\_ We infer that the SMAP-derived perched firn aquifer extent represents L-band emissions  
1246 from: (1) spatially expansive, relatively shallow water-saturated firn layers with lower volumetric fractions of  
1247 meltwater as compared to perennial firn aquifer areas. These shallow water-saturated firn layers transiently  
1248 form on top of buried ice slabs, spatially coherent melt layers, or other semi-impermeable layers that have  
1249 previously formed within the upper snow and firn layers of the percolation facies, as shown in Figs. 7-8. Or,  
1250 (2) spatially scattered deeper water-saturated firn layers with larger volumetric fractions of meltwater (i.e.,  
1251 perennial firn aquifers) that are spatially integrated with L-band emissions from adjacent ice slabs,  
1252 percolation facies, and/or wet snow facies areas. These areas are observed as shallow water-saturated firn  
1253 layers with lower volumetric fractions of meltwater over SMAP's ~18 km footprint (i.e., the effective  
1254 resolution). Or, (3) a combination of these englacial firn hydrological features, which is a likely scenario  
1255 over many perched firn aquifers areas. This is particularly likely in north western Greenland, where airborne  
1256 ice penetrating radar surveys consistently detect perennial firn aquifers; however, the SMAP-derived extent  
1257 indicates perched firn aquifer areas (Fig. 7).

1258  
1259 \_\_\_\_\_ Shallow buried supraglacial lakes have recently been identified within the percolation facies of  
1260 western, northern, and north and central eastern Greenland using airborne ice-penetrating radar surveys  
1261 (Koenig et al., 2015) and satellite synthetic aperture radar imagery (Miles et al., 2017; Schröder et al., 2020;  
1262 Dunmire et al., 2021). These buried supraglacial lakes are within the SMAP-derived perennial firn aquifer  
1263 and, ice slab, and perched firn aquifer extents, however, they are not expected to significantly influence L-  
1264 band emissions in these areas for two reasons: (1) As compared to SMAP's ~18 km footprint, the mean  
1265 extent of buried supraglacial lakes is limited (less than ~1 km<sup>2</sup>), and they are sparsely distributed in  
1266 perennial firn aquifer and, ice slab, and perched firn aquifer areas (Dunmire et al., 2021). (2) Supraglacial  
1267 lakes form during the melting season as a result of meltwater storage within meltwater storage in  
1268 topographic depressions at the ice sheet surface (Echelmeyer et al. 1991). Similar to subglacial lakes  
1269 (Jezek et al., 2015) and perennial firn aquifers (Miller et al., 2020), supraglacial lakes represent  
1270 radiometrically cold subsurface near-surface meltwater reservoirs. Upwelling L-band emissions from  
1271 deeper firn layers, superimposed and/or glacial ice, and the underlying bedrock are effectively blocked by

Formatted: Not Highlight

Formatted: Not Highlight

Formatted: Not Highlight

1272 high reflectivity and attenuation at the interface between the impermeable layer-lake bottom and the  
1273 underlying interfaceimpermeable layer. This results in a low observed  $T^B$  at the upper surface of meltwater  
1274 stored within supraglacial lakes. During the freezing season, the upper surface of meltwater of meltwater  
1275 stored within supraglacial lakes refreezes and forms a partial or solid-ice cap that is sometimes buried by  
1276 snow accumulation (Koenig et al., 2015). Airborne ice-penetrating radar surveys in April and May between  
1277 2009 and 2012 suggest the mean depth to the upper surface of meltwater stored within buried supraglacial  
1278 lakes is approximately ~2 m (Koenig et al., 2015). As previously noted, over perennial firn aquifer, ice slab,  
1279 and perched firn aquifer areas, L-band emissions from the radiometrically warm upper snow and firn layers  
1280 decrease on variable time scales during the freezing season as embedded ice structures slowly refreeze  
1281 at increased depths below the ice sheet surface and induce strong volume scattering (Rignot et al., 1993;  
1282 Rignot 1995).  $T_V^B$  can decrease by as much as ~50 K during the freezing season (e.g., Fig. 4a), representing  
1283 the descent of the upper surface of stored meltwater by ~tens of meters (Miège et al., 2016). However,  
1284 overOver buried supraglacial lakes, L-band emissions from the refreezing partial or solid-ice cap, which is  
1285 smooth relative to the L-band wavelength (~21 cm), likely induces surface scattering. As a result,  $T_V^B$   
1286 decreases over buried supraglacial lakes are likely negligible. Thus, over SMAP's ~18 km footprint, we  
1287 postulate water-saturated firn layers dominate L-band emissions over the percolation facies of the GrIS.

1288 The SMAP-derived perennial firn aquifer extent (64,000 km<sup>2</sup>) generated by our adapted empirical  
1289 algorithm and the multi-year calibration technique (2015-2019) is consistent with the extent (66,000 km<sup>2</sup>)  
1290 generated by the previously developed empirical algorithm and the single-coincident year calibration  
1291 technique (2016) described in Miller et al., 2020. The SMAP-derived perennial firn aquifer extent is generally  
1292 consistent with previous C-band (5.3 GHz) satellite radar scatterometer-derived perennial firn aquifer  
1293 extents mapped using the Advanced SCATterometer (ASCAT) on the European Organization for the  
1294 Exploitation of Meteorological Satellites (EUMETSAT) Meteorological Operational A (MetOp-A) satellite  
1295 (2009-2016, 52 000-153 000 km<sup>2</sup>; Miller, 2019), and the Active Microwave Instrument in radar scatterometer  
1296 mode (ESCAT) on ESA's European Remote Sensing (ERS) satellite series (1992-2001, 37 000-64 000 km<sup>2</sup>;  
1297 Miller, 2019) as well as the C-band (5.4 GHz) synthetic aperture radar-derived extent mapped using ESA's  
1298 Sentinel-1 satellite (2014-2019, 54 000 km<sup>2</sup>; Brangers et al., 2020). The exception is the ASCAT-derived  
1299 perennial firn aquifer extent (2012-2013, 153,000 km<sup>2</sup>; Miller, 2019) mapped following the 2012 melting  
1300 season (Nghiem et al., 2012) in which significant changes in the dielectric and geophysical properties that  
1301 influence radar backscatter likely occurred. The unreasonably expansive (j.e., more than twice the mean)  
1302 mapped extent is a result of ASCAT'S shallow (several meters) C-band penetration depth (Jezek et al.,  
1303 1994), and the simple threshold-based algorithm, which was not calibrated for an extreme melting season  
1304 that included saturation of the upper snow and firn layers of the dry snow facies and percolation facies with  
1305 relatively large volumetric fractions of meltwater (Miller et al., 2019). Water-saturated firn layers had  
1306 extended refreezing rates, however, seasonal meltwater was not stored at depth. Widespread spatially  
1307 coherent melt layers were alternatively formed in many of the mapped areas (Culberg et al., 2021). The

Formatted: Not Highlight

Formatted: Not Strikethrough

Formatted: Not Highlight

Formatted: Not Highlight

Formatted: Not Highlight

Formatted: Not Highlight

Formatted: Not Highlight

1308 SMAP-derived ice slab extent (76,000 km<sup>2</sup>) is also consistent with previous AR-derived ice slab extents  
1309 (2010-2014, 64,800 km<sup>2</sup>-69,400 km<sup>2</sup>; McFerrin et al., 2019).

1310 ~~————— The SMAP-derived perennial firn aquifer extent (~64,000 km<sup>2</sup>) generated by our adapted empirical~~  
1311 ~~algorithm and the multi-year (2010-2017) calibration technique is consistent with the extent (~66,000 km<sup>2</sup>)~~  
1312 ~~generated by the previously developed empirical algorithm and the single-coincident year (2016) calibration~~  
1313 ~~technique described in Miller et al., 2020. The SMAP-derived perennial firn aquifer extent is generally~~  
1314 ~~consistent with previous C-band (5.3 GHz) satellite radar scatterometer-derived perennial firn aquifer~~  
1315 ~~extents mapped using the Advanced SCATterometer (ASCAT) on the European Organization for the~~  
1316 ~~Exploitation of Meteorological Satellites (EUMETSAT) Meteorological Operational A (MetOp-A) satellite~~  
1317 ~~(2009-2016, ~52,000-153,000 km<sup>2</sup>; Miller, 2019), and the Active Microwave Instrument in radar~~  
1318 ~~scatterometer mode (ESCAT) on ESA's European Remote Sensing (ERS) satellite series (1992-2001,~~  
1319 ~~~37,000-64,000 km<sup>2</sup>; Miller, 2019) as well as the C-band (5.4 GHz) synthetic aperture radar-derived extent~~  
1320 ~~mapped using ESA's Sentinel-1 satellite (2014-2019, ~54,000 km<sup>2</sup>; Brangers et al., 2020). The exception~~  
1321 ~~is the ASCAT-derived perennial firn aquifer extent (2012-2013, ~153,000 km<sup>2</sup>; Miller et al., 2019) mapped~~  
1322 ~~following the anomalous 2012 melting season (Nghiem et al., 2012) in which significant changes in the~~  
1323 ~~dielectric and geophysical properties that influence radar backscatter and the temporal C-band signatures~~  
1324 ~~occurred. The unreasonably expansive (i.e., more than twice the mean) mapped extent is a result of~~  
1325 ~~ASCAT'S shallow (~several meters) C-band penetration depth (Jezek et al., 1994), and the simple~~  
1326 ~~threshold-based algorithm that was not calibrated for an extreme melting season that included saturation~~  
1327 ~~of the upper snow and firn layers of the dry snow facies and percolation facies with relatively large~~  
1328 ~~volumetric fractions of meltwater (Miller et al., 2019). Water-saturated firn layers had extended refreezing~~  
1329 ~~rates, however, seasonal meltwater was not stored at depth. Spatially coherent melt layers were~~  
1330 ~~alternatively formed in many of the mapped areas (Culberg et al., 2024). The SMAP-derived ice slab extent~~  
1331 ~~(~76,000 km<sup>2</sup>) is also consistent with previous AR-derived ice slab extents (2010-2014, ~64,800 km<sup>2</sup>-69,400~~  
1332 ~~km<sup>2</sup>; McFerrinMacFerrin et al., 2019).~~

1333 Although we simply consider our mapped extents a high-probability area for preferential formation,  
1334 the maps generated by our adapted empirical algorithm and the multi-year (2010-2017) calibration  
1335 technique for individual years suggest there reasonable interannual variability in perennial firn aquifer and  
1336 ice and slab, and perched firn aquifer extents (which is summarized in Table 35). Our results demonstrate  
1337 reasonable sensitivity to the variability in the depth- and time-integrated dielectric and geophysical  
1338 properties of the percolation facies that dielectric and geophysical properties that influence the radiometric  
1339 temperature and temporal L-band signatures, even during the extreme 2015 melting season (Tedesco et  
1340 al., 2016).

#### 1341 **4 Implications**

1342 Seasonal surface melting over the GrIS has increased in extent, intensity, and duration since early in the  
1343 satellite era (Steffen et al., 2004; Tedesco e al., 2008; Tedesco et al., 2011; Nghiem et al., 2012; Tedesco  
1344 et al., 2016; Tedesco and Fettweis, 2020; Cullather et al., 2020). Consistent with recent seasonal surface

Formatted: Not Highlight

Formatted: Font: Arial Black, Not Highlight

Formatted: Space Before: 1.5 pt, After: 1.5 pt

Formatted: Not Highlight

Formatted: Not Highlight

Formatted: Font: 10 pt, Not Highlight

Formatted: Not Highlight

1345 melting trends, meltwater run-off has accelerated to become the dominant mass loss mechanism over the  
1346 GrIS (van den Broeke et al., 2016). Meltwater storage in both solid (i.e., embedded ice structures, including  
1347 ice slabs, spatially coherent melt layers) and liquid (i.e., perennial firn aquifers) form can buffer meltwater  
1348 run-off in the percolation facies and delay its eventual release into the ocean (Harper et al., 2012). However,  
1349 significant uncertainty remains in meltwater run-off estimates as a result of the lack of knowledge of  
1350 heterogeneous infiltration and refreezing processes within the snow and firn layers (Pfeffer and Humphrey,  
1351 1996), and the depths to which meltwater can descend beneath the ice sheet surface (Humphrey et al.,  
1352 2012).

1353 If the increasing seasonal surface melting trend continues (Franco et al., 2013; Noël et al., 2021),  
1354 perennial firn aquifer formation and expansion may increase the possibility of crevasse-deepening via  
1355 meltwater-induced hydrofracturing (Alley et al., 2005; van der Veen, 2007), especially if crevasse fields  
1356 expand into perennial firn aquifer areas as a result of accelerated ice flow (Colgan et al., 2016). Meltwater-  
1357 induced hydrofracturing is an important component of supraglacial lake drainage during the melting season  
1358 (Das et al., 2008; Stevens et al., 2015) leading to at least temporary localized accelerated ice flow velocities  
1359 (Zwally et al., 2002; Joughin et al., 2013; Moon et al., 2014) as well as ice discharge from outlet glaciers  
1360 (Chudley et al., 2019), and mass balance changes (Joughin et al., 2008). Perennial firn aquifers may also  
1361 support meltwater-induced hydrofracturing, even during the freezing season (Poinar et al., 2017; Poinar et  
1362 al., 2019).

1363 The formation and expansion of ice slabs reduces permeability within the upper snow and firn  
1364 layers and facilitates lateral meltwater flow with minimum vertical percolation into the deeper firn layers,  
1365 thereby enhancing meltwater run-off and mass loss at the periphery (MacFerrin et al., 2019). Lateral  
1366 meltwater flow across ice layers overlying deeper permeable firn layers was first postulated by Müller  
1367 (1962). The theory was then further developed by Pfeffer et al., (1991) as an end-member case for  
1368 meltwater run-off in the percolation facies, with the other end member case being lateral meltwater flow  
1369 across superimposed ice in the wet snow facies and/or across glacial ice in the ablation facies. Lateral  
1370 meltwater flow and high-elevation (1850 m a.s.l) meltwater run-off across ice slabs in the percolation facies  
1371 was recently observed in visible satellite imagery collected by the NASA-USGS Landsat 7 mission during  
1372 the 2012 melting season (MacFerrin et al., 2019).

1373 Spatially coherent melt layers represent a newly identified end-member case for meltwater runoff  
1374 in the dry snow facies (Culberg et al., 2021). Similar to ice slabs, the formation and expansion of spatially  
1375 coherent melt layers reduces the pore space within the upper snow and firn layers, and may also facilitate  
1376 lateral meltwater flow with minimum vertical percolation into the deeper firn layers, thereby enhancing  
1377 meltwater run-off from significantly higher elevations on accelerated time scales. The rapid formation of  
1378 spatially coherent melt layers that merge with ice slabs upslope of perennial firn aquifers areas may  
1379 simultaneously accelerate both meltwater run-off and meltwater-induced hydrofracturing during extreme  
1380 melting seasons. The formation of spatially coherent melt layers overlying deeper perennial firn aquifers  
1381 may result in the formation of shallow perched firn aquifers (Culberg et al., 2021), or may terminate gravity-

Formatted: Not Highlight

Formatted: Not Highlight

Formatted: Not Highlight

Formatted: Space Before: 0 pt

Formatted: Not Highlight

Formatted: Not Highlight

Formatted: Not Highlight

Formatted: Not Highlight

Formatted: Not Highlight

Formatted: Font: Arial, Not Highlight

Formatted: Not Highlight

Formatted: Not Highlight

Formatted: Not Highlight

Formatted: Not Highlight

Formatted: Not Highlight

Formatted: Not Highlight

Formatted: Not Highlight

Formatted: Not Highlight

Formatted: Not Highlight

Formatted: Not Highlight

Formatted: Not Highlight

Formatted: Not Highlight

1382 driven meltwater drainage and seasonal recharging (Fountain and Walder, 1998), which may eventually  
 1383 completely refreeze stored meltwater into ice slabs or decimeters thick solid-ice layers overlying deeper  
 1384 glacial ice.

Formatted: Pattern: Clear, Not Highlight

1385 ▲  
 1386 Nghiem et al., (2003) previously demonstrated mapping spatially coherent melt layers that were formed  
 1387 following the anomalous 2002 melting season (Steffen et al., 2004) using similar signatures observed in  
 1388 Ku-band radar backscatter time series collected by the SeaWinds radar scatterometer that was flown on  
 1389 NASA's QuikSCAT satellite (Tsai et al., 2000).

Formatted: Not Highlight

1390  
 1391  
 1392 **Table 5** *The SMAP-derived perennial firn aquifer, ice slab, and perched firn aquifer extents (2015-2019).*

	<b>Perennial Firn Aquifer Extent</b>	<b>Ice Slab Extent</b>	<b>Perched Firn Aquifer Extent</b>
	<b>(km<sup>2</sup>)</b>	<b>(km<sup>2</sup>)</b>	<b>(km<sup>2</sup>)</b>
<b>2015-2019</b>	66,000	76,000	37,000
<b>2015-2016</b>	63,000	23,000	17,000
<b>2016-2017</b>	69,000	48,000	38,000
<b>2017-2018</b>	73,000	27,000	20,000
<b>2018-2019</b>	70,000	38,000	26,000

1393  
 1394

Formatted: Space After: 5 pt

1395  
 1396  
 1397  
 1398 Consistent with recent seasonal surface melting trends, meltwater run-off has accelerated to  
 1399 become the dominant mass loss mechanism over the GrIS (van den Broeke et al., 2016). However,  
 1400 significant uncertainty remains in meltwater run-off estimates in the percolation facies as a result of the lack  
 1401 of knowledge of heterogeneous infiltration processes within the snow and firn layers (Pfeffer and Humphrey,  
 1402 1996), the depths to which meltwater can descend beneath the ice sheet surface (Humphrey et al., 2012),  
 1403 and the formation of englacial firn hydrological features (Benson et al., 1960; Humphrey et al., 2012; Forster  
 1404 et al., 2014), especially ice layers and ice slabs (Machguth et al., 2016; McFerrin, MacFerrin et al., 2019;  
 1405 Culberg et al., 2021). A notable example of this lack of knowledge is the identification by Forster et al.,  
 1406 (2014) of widespread perennial firn aquifers within the percolation facies of the GrIS via airborne ice-  
 1407 penetrating radar surveys collected by NASA's OIB campaigns (2010-2014; Rodriguez-Morales et al. 2014)  
 1408 that store large volumes (~140 Gt; Koenig et al., 2014) of meltwater that was previously unknown. The

1409 mapped extent (2010-2014) shown in Forster et al., (2014) can be distinctly observed in 1978 enhanced  
1410 resolution Ku-band radar backscatter imagery (Long and Drinkwater, 1994) collected by the radar  
1411 scatterometer on NASA's first Earth-observing satellite—the Seasat A mission (Jones et al., 1982). This  
1412 suggests that Greenland's perennial firn aquifers have likely existed undetected in the deeper firn layers of  
1413 the percolation facies for decades. Meltwater storage in both solid (i.e., embedded ice structures) and liquid  
1414 (i.e., perennial firn and perched firn aquifers) form can buffer meltwater run-off in the percolation facies  
1415 (Harper et al., 2012). However, the formation of near-surface ice layers and ice slabs reduces the pore  
1416 space within the upper snow and firn layers and facilitates lateral meltwater flow with minimum vertical  
1417 percolation into the deeper firn layers, thus enhancing meltwater run-off downslope towards the periphery.  
1418 Lateral meltwater flow across ice layers overlying deeper permeable firn layers was first postulated by  
1419 Müller (1962). The theory was then further developed by Pfeffer et al., (1991) as an end member case for  
1420 meltwater run-off, with the other end member case being lateral meltwater flow across superimposed ice in  
1421 the wet snow facies and/or across glacial ice in the ablation facies. McFerrinMacFerrin et al., (2019) recently  
1422 identified widespread near-surface ice slabs within the percolation facies of the GrIS via airborne ice-  
1423 penetrating radar surveys collected by NASA's OIB campaigns (2010-2014; Rodriguez-Morales et al.  
1424 2014). Lateral meltwater flow and high-elevation (~1850 m.a.s.l.) meltwater run-off across the identified ice  
1425 slabs was also observed in visible satellite imagery collected by the NASA-USGS Landsat 7 mission (e.g.  
1426 Goward et al., 2001). This was also observed during the anomalous 2012 melting season  
1427 (McFerrinMacFerrin et al., 2019) during which seasonal surface melting extended over ~99% of the GrIS  
1428 (Nghiem et al., 2012).

1429 Additionally, we correlate exponentially decreasing temporal L-band signatures with AR- and MCoRDS-  
1430 derived detections where perennial firn aquifer and ice slab areas overlap. We identify these transitional  
1431 areas as perched firn aquifer areas. We infer that, in these areas, shallow water-saturated firn layers  
1432 transiently form on top of buried ice slabs or other semi-impermeable layers, such as spatially coherent  
1433 melt layers that form in the higher elevations (> ~2000 m.a.s.l.) of the percolation facies and the dry snow  
1434 facies that were recently identified via AR (Culberg et al., 2021). Perched firn aquifers likely form during  
1435 some melting seasons as a result of interannual variability in surface melting and snow accumulation, and  
1436 the formation of englacial firn hydrological features.

## 1437 **5 Summary and Future Work**

1438 Many open questions remain about Greenland's perennial firn aquifers, regarding initial formation,  
1439 extent, depth, flow characteristics, timescales of refreezing and/or englacial drainage, and connections to  
1440 the subglacial hydrological system. Seasonal surface melting over the GrIS has increased in extent,  
1441 intensity, and duration since the beginning of the satellite era (Steffen et al., 2004; Tedesco et al., 2008;  
1442 Tedesco et al., 2011; Nghiem et al., 2012; Tedesco et al., 2016; Tedesco and Fettweis, 2020; Cullather et  
1443 al., 2020). If this trend continues (Franco et al., 2013; Noël et al., 2021), subsequent increases in the  
1444 volume of meltwater stored within Greenland's perennial firn aquifers will increase the possibility of

Formatted: Font: 10 pt

1445 ~~crevasse-deepening via meltwater-induced hydrofracturing (Alley et al., 2005; van der Veen, 2007),~~  
1446 ~~especially if crevasse fields laterally expand into perennial firn aquifer areas as a result of accelerated ice~~  
1447 ~~flow (Colgan et al., 2016). Meltwater-induced hydrofracturing is an important component of supraglacial~~  
1448 ~~lake drainage during the melting season (Das et al., 2008; Stevens et al., 2015) leading to at least temporary~~  
1449 ~~accelerated flow velocities (Zwally et al., 2002; Joughin et al., 2013; Moon et al., 2014) and mass balance~~  
1450 ~~changes (Joughin et al., 2008). Greenland's firn perennial aquifers may also support meltwater-induced~~  
1451 ~~hydrofracturing, even during the freezing season (Poinar et al., 2017; 2019).~~

1452  
1453 ~~\_\_\_\_\_ L-band satellite microwave sensors — including NASA's L-band SMAP mission — represent a~~  
1454 ~~relatively new Earth-observation tool that has exceptional capabilities for cryospheric applications.~~  
1455 ~~Especially, mapping englacial and subglacial hydrological features at depths of tens to hundreds of meters~~  
1456 ~~beneath the surface of Earth's polar ice sheets. In this study, for the first time, we have exploited this~~  
1457 ~~capability and demonstrated the novel use of the L-band microwave radiometer on NASA's SMAP satellite~~  
1458 ~~for mapping perennial firn aquifers and, ice slabs, and perched firn aquifers together as a continuous system~~  
1459 ~~over the percolation facies of the GfIS. We have also demonstrated that SMAP-enhanced-resolution L-~~  
1460 ~~band  $T_V^{\beta}$  imagery can effectively resolve percolation facies features that are not effectively resolved in~~  
1461 ~~conventionally processed SMAP L-band  $T_V^{\beta}$  imagery (e.g., Fig. 1). We have adapted our previously~~  
1462 ~~developed empirical algorithm (Miller et al., 2020) by expanding our analysis of spatiotemporal differences~~  
1463 ~~in SMAP enhanced-resolution  $T_V^{\beta}$  imagery and temporal L-band signatures ~~over the GfIS. We have used~~~~  
1464 ~~this analysis to derive a firn saturation parameter from a simple two-layer L-band geophysical-brightness~~  
1465 ~~temperature model (Miller et al., 2021, in press). And, we have used the firn saturation parameter to map~~  
1466 ~~the extent of the percolation facies. We have found that by correlating maximum and minimum  $T_V^{\beta}$  values,~~  
1467 ~~the firn saturation parameter, and the refreezing rate parameter with perennial firn aquifer and, ice slab,~~  
1468 ~~and perched firn aquifer detections identified via via the CReSIS AR and MCoRDS instruments flown by~~  
1469 ~~NASA's OIB campaigns that we can calibrate our previously developed empirical algorithm (Miller et al.,~~  
1470 ~~2020) to map plausible extents.~~

1471 ~~\_\_\_\_\_ We note that significant uncertainty exists in the mapped extents as a result of (1) (1)~~  
1472 ~~correlating the SMAP-derived parameters with airborne ice-penetrating radar detections that are not~~  
1473 ~~coincident in time, (2) (2) the lack of a distinct temporal L-band signature delineating the boundary between~~  
1474 ~~perennial firn aquifer areas, ice slabs areas, and adjacent percolation facies areas delineating the boundary~~  
1475 ~~between each of the mapped sub-facies within the broader percolation facies, and (3) (3) the much more~~  
1476 ~~limited extent of the airborne ice-penetrating radar detections as compared to the rSIR grid cell extent, as~~  
1477 ~~well as and the effective resolution of the SMAP enhanced-resolution  $T_V^{\beta}$  imagery. Additional uncertainty~~  
1478 ~~exists in the perched firn aquifer extent as a result of fitting L-band signatures to the continuous logistic~~  
1479 ~~model, which is not optimal for these specific sub-facies.~~

Formatted: Not Highlight

Formatted: Not Highlight

Formatted: Font: , Pattern: Clear (White)

Formatted: Not Highlight

Formatted: Not Highlight



1481 \_\_\_\_\_ Miller et al., (2020) normalized SMAP enhanced-resolution  $T_V^B$  time series and converted  
1482 the exponential rate of  $T_V^B$  decrease over perennial firn aquifer areas to a binary parameter to map extent.  
1483 In this study, we have converted the SMAP-derived parameters to binary parameters to map the extent of  
1484 ~~both perennial firn aquifer, and, ice slab, and perched firn aquifer~~ areas. Moreover, we have included  
1485 additional analysis of the spatiotemporal differences in maximum and minimum  $T_V^B$  values, the firn  
1486 saturation parameter, and the refreezing rate parameter. We have shown that spatiotemporal differences  
1487 in the SMAP-derived parameters are consistent with our assumption of spatiotemporal differences in the  
1488 englacial hydrology and thermal characteristics of firn layers at depth.  
1489 ~~Particularly, our assumption that latent heat release influences temporal L-band signatures within~~  
1490 ~~the percolation facies of the GrIS. This includes continuous latent heat release via the slow refreezing of~~  
1491 ~~the deeper firn layers in perennial and perched firn aquifer areas that are saturated with large volumetric~~  
1492 ~~fractions of meltwater. And, latent heat release that occurs throughout the percolation facies via more rapid~~  
1493 ~~refreezing of seasonal meltwater by the descending winter cold wave, and the subsequent formation of~~  
1494 ~~embedded ice structures, including ice slabs and spatially coherent melt layers, within the upper snow and~~  
1495 ~~firn layers.~~  
1496 \_\_\_\_\_ Future work will focus on simulating ~~maximum and minimum  $T_V^B$ , the firn saturation parameter, and~~  
1497 ~~the refreezing rate parameter as well as~~ temporal L-band signatures observed over perennial firn aquifer  
1498 ~~and, ice slab, and perched firn aquifer~~ areas ~~within the percolation facies of the GrIS~~ for a wide range of  
1499 geophysical properties. ~~Significant interannual variability in the dielectric and geophysical properties that~~  
1500 ~~seasonally influence the radiometric temperature and temporal L-band signatures can occur, particularly~~  
1501 ~~following extreme melting seasons, such that it is critical that these properties are understood and~~  
1502 ~~considered in any given year.~~ To better interannual variability, ~~in extent as well as other geophysical~~  
1503 ~~properties~~, we will interpret our results together with climatological parameters, such as snow accumulation,  
1504 liquid water content, ~~temperature~~, and surface mass balance ~~simulated, and over the GrIS simulated using~~  
1505 ~~theby the~~ Regional Atmospheric Climate Model (RACMO2.3p2; Noël et al., 2018). Additionally, we will  
1506 simulate the distinct temporal L-band signatures observed over spatially coherent melt layers ~~in the upper~~  
1507 ~~snow and firn layers of the dry snow facies and percolation facies of the GrIS recently identified via~~  
1508 ~~MCoRDS flown by NASA's OIB campaigns (Culberg et al., 2021) following the anomalous 2012 melting~~  
1509 ~~season (Nghiem et al., 2012) and and as well as explore the potential for mapping thethe extent of these~~  
1510 ~~near surface englacial hydrological features using satellite L-band microwave radiometry.~~ Nghiem et al.,  
1511 ~~(2003) previously demonstrated mapping spatially coherent melt layers that were formed following the~~  
1512 ~~anomalous 2002 melting season (Steffen et al., 2004) using similar signatures observed in Ku band radar~~  
1513 ~~backscatter time series collected by the SeaWinds radar scatterometer that was flown on NASA's~~  
1514 ~~QuikSCAT satellite (Tsai et al., 2000).~~  
1515 \_\_\_\_\_ Combining multi-layer depth-integrated L-band ~~geophysical~~ brightness temperature models (e.g.,  
1516 Jezek et al., 2015) that include embedded ice structure parametrizations (e.g., Jezek et al., 2018) with  
1517 models of depth-dependent geophysical parameters can lead to an improved understanding of the

Formatted: Widow/Orphan control

Formatted: Not Highlight

Formatted: Not Highlight

Formatted: Strikethrough

Formatted: Not Highlight

1518 extremely complex and ~~very~~ poorly described physics controlling L-band emissions over the percolation  
1519 facies of the GrIS. For ~~L-band emissions over perennial firn aquifer, ice slab, perched firn aquifer, and~~  
1520 ~~spatially coherent melt layer areas, the~~ ~~Key~~ key geophysical parameters include atmospheric temperature  
1521 forcing, physical temperature versus depth, latent heat, snow accumulation, the volumetric fraction and  
1522 depth of meltwater, and the volumetric fraction and geometric configuration of embedded ice structures.  
1523 The development of more sophisticated empirical algorithms that incorporate multi-layer depth-integrated  
1524 L-band ~~geophysical~~ brightness temperature models that are constrained by in situ measurements can help  
1525 reduce the significant uncertainty in the current mapped extents, and provide more accurate boundary  
1526 ~~delineation ies delineating each of these sub-facies within the broader percolation facies~~ that can be used  
1527 to ~~further~~ quantify ~~the interannual variability in future mapped extents of perennial firn aquifer, ice slabs and~~  
1528 ~~spatially coherent melt layer areas, in extent. As Greenland's climate continues to warm, and seasonal~~  
1529 ~~surface melting increases in extent, intensity, and duration, quantifying the possible rapid expansion of each~~  
1530 ~~of these sub-facies using satellite L-band microwave radiometry has significant implications for~~  
1531 ~~understanding ice sheet-wide variability in englacial firn hydrology resulting in meltwater-induced~~  
1532 ~~hydrofracturing and accelerated ice flow as well as high-elevation run-off that can impact the mass balance~~  
1533 ~~and stability of the GrIS.~~

1534 ——— The results presented in this study demonstrate the outstanding potential of L-band satellite  
1535 microwave sensors for mapping englacial firn hydrological features within the percolation facies of the GrIS  
1536 that can be extended to forthcoming satellite missions, such as the NASA-ISRO SAR mission (NISAR),  
1537 ESA's Copernicus Imaging Microwave Radiometer (CIMR) mission, ESA's Copernicus Radar Observation  
1538 System for Europe in L-band (ROSE-L) mission, and candidate missions, such as ESA's Earth Explorer 10  
1539 Cryorad mission.

1540

## 1541 **Data Availability**

1542 ~~SMAP Radiometer Twice-Daily rSIR-Enhanced EASE-Grid 2.0 Brightness Temperatures, Version 1~~ SMAP  
1543 ~~enhanced-resolution L-band  $T_{\mu}$  imagery~~ (2015-2019) have been produced as part of the NASA Science  
1544 Utilization of SMAP project and are available at <https://doi.org/10.5067/QZ3WJNOUZLFK> (Brodzik et al.,  
1545 2019). The NASA MEASUREs Greenland Ice Mapping Project (GIMP) Land Ice and Ocean Classification  
1546 Mask, Version 1, is available at <https://doi.org/10.5067/B8X58MQBFUPA> (Howat, 2017), and the Digital  
1547 Elevation Model, Version 1, is available at <https://nsidc.org/data/nsidc-0645/versions/1> (Howat et al., 2015).  
1548 The coastline data are available from GSHHG – A Global Self-consistent, Hierarchical, High-resolution  
1549 Geography Database <https://doi.org/10.1029/96JB00104> (Wessel and Smith, 1996). Ice surface  
1550 temperature imagery (2015-2019) have been produced as part of the Multilayer Greenland Ice Surface  
1551 Temperature, Surface Albedo, and Water Vapor from MODIS V001 data set and are available at  
1552 <https://doi.org/10.5067/7THUWT9NMPDK> (Hall and DiGirolamo, 2019). OIB AR- and MCoRDS-derived  
1553 perennial firn aquifers detections (2010-2017) are available at

Formatted: Not Highlight

Formatted: Font:

Formatted: No Spacing, Widow/Orphan control

Formatted: Font: Font color: Black, , Pattern: Clear (White)

Formatted: Space Before: 5 pt, After: 5 pt

Formatted: Font: 10 pt

Formatted: Font: 10 pt

Formatted: Font: 10 pt

Formatted: Font: 10 pt

Formatted: Font: 10 pt

Formatted: Font: 10 pt

1554 <https://arcticdata.io/catalog/view/doi:10.18739/A2985M> (Miège et al., 2016). OIB AR-derived ice slab  
1555 detections (2010-2014) are available at <https://doi.org/10.6084/m9.figshare.8309777> (McFerrinMacFerrin  
1556 et al., 2019). OIB AR-derived spatially coherent melt layer detections (2017) are available at  
1557 (<https://doi.org/10.18739/A2736M33W>) (Culberg et al., 2021). OIB AR L1B Geolocated Radar Echo  
1558 Strength Profiles, Version 2, are available at <https://doi.org/10.5067/OZY1XYHNIQNY> (Paden et al., 2018).  
1559 NASA MEaSURES MODIS Mosaic of Greenland (MOG) 2015 Image Map, Version 2, is available at  
1560 <https://nsidc.org/data/NSIDC-0547/versions/2> (Haran et al., 2018). SMAP-derived perennial firn aquifer, ice  
1561 slab, and perched firn aquifer extents are available from JZM upon request.

Formatted: Font: 10 pt

Formatted: Font: 10 pt

Formatted: Font: 10 pt

Formatted: Font: 10 pt

Formatted: Font: 10 pt

1562

### 1563 **Author Contributions**

1564 JZM initiated the study, adapted the empirical model, performed the analyses, and wrote the manuscript.  
1565 RC processed and interpreted the OIB AR radargram profiles. RC and DMS provided the spatially coherent  
1566 melt layer detections. All authors participated in discussions and reviewed manuscript drafts.

Formatted: Font: 10 pt

Formatted: Space Before: 5 pt, After: 5 pt

1567

1568

### 1569 **Competing Interests**

1570 The authors declare that they have no conflict of interest.

Formatted: Font: 10 pt

Formatted: Space Before: 5 pt, After: 5 pt

1571

1572

1573

1574

### 1575 **Financial Support**

1576 JZM, DGL, and MJB are supported by the NASA SMAP Science Team (no. 80NSSC20K1806), and by  
1577 the NASA Cryospheric Science Program (no. 80NSSC18K1055 and no. 80NSSC21K0749) under grants  
1578 to the University of Colorado and Brigham Young University. RC is supported by a National Defense  
1579 Science and Engineering Graduate Fellowship. RC and DMS are supported in part by NASA (no.  
1580 NNX16AJ95G and NSF (no. 1745137). CAS is supported by the NASA Headquarters Cryospheric Science  
1581 Program. We acknowledge the use of data from CReSIS generated with support from the University of  
1582 Kansas, NASA Operation IceBridge grant NNX16AH54G, NSF grants ACI-1443054, OPP-1739003, and  
1583 IIS-1838230, Lilly Endowment Incorporated, and Indiana METACyt Initiative.

Formatted: Font: 10 pt

Formatted: Space Before: 5 pt, After: 5 pt

Formatted: Font: 10 pt, Not Italic

1584

### 1585 **References**

Formatted: Font: 10 pt

Formatted: Space Before: 5 pt, After: 5 pt

1586 Abdalati, W., and Steffen, K.: Snowmelt on the Greenland Ice Sheet as derived from passive microwave  
1587 satellite data, *J. Climate*, 10, 165-175, [https://doi.org/10.1175/1520-0442\(1997\)010<0165:SOTGIS>2.0.CO;2](https://doi.org/10.1175/1520-0442(1997)010<0165:SOTGIS>2.0.CO;2), 1997.

1589  
1590 Alley, R. B., Dupont, T. K., Parizek, B. R., Anandakrishnan, S.: Access of surface meltwater to beds of sub-  
1591 freezing glaciers: Preliminary insights, *Ann. Glaciol.*, 40, 8-14,  
1592 <https://doi.org/10.3189/172756405781813483>, 2005.

1593  
1594 Ashcraft, I. and Long, D.: Comparison of methods for melt detection over Greenland using active and  
1595 passive microwave measurements, *Int. J. Remote Sens.*, 27, 2469-2488,  
1596 <https://doi.org/10.1080/01431160500534465>, 2006.

1597  
1598 Benson, C. S.: Stratigraphic studies in the snow and firn of the Greenland Ice Sheet, Ph.D. thesis, California  
1599 Institute of Technology, 228 pp., 1960.

1600  
1601 Bindschadler, R. A., Jezek, K. C., and Crawford, J.: Glaciological investigations using the synthetic aperture  
1602 radar imaging system, *Ann. Glaciol.*, 9, 11-19. <https://doi.org/10.1017/S0260305500200694>, 1987.

1603  
1604 Brangers, I., Lievens, H., Miège, C., Demuzere, M., Brucker, L., and De Lannoy, G. J. M.: Sentinel-1 detects  
1605 firn aquifers in the Greenland Ice Sheet, *Geophys. Res. Lett.*, 47, [e2019GL085192](https://doi.org/10.1029/2019GL085192),  
1606 <https://doi.org/10.1029/2019GL085192>, 2020.

1607  
1608 Brodzik, M. J., Long, D. G., and Hardman, M. A.: SMAP Radiometer Twice-Daily rSIR-Enhanced EASE-  
1609 Grid 2.0 Brightness Temperatures, Version 1, NASA National Snow and Ice Data Center Distributed Active  
1610 Archive Center, <https://doi.org/10.5067/QZ3WJNOUZLFK>, 2019.

1611  
1612 Brodzik, M. J., Billingsley, B., Haran, T., Raup, B., and Savoie, M. H.: EASE-Grid 2.0: Incremental but  
1613 significant improvements for Earth-gridded data sets, *ISPRS Int. J. Geo-Inf.*, 1, 32-45,  
1614 <https://doi.org/10.3390/ijgi1010032>, 2012.

1615  
1616 Chu, W., Schroeder, D. M., and Siegfried, M. R.: Retrieval of englacial firn aquifer thickness from ice-  
1617 penetrating radar sounding in southeastern Greenland, *Geophys. Res. Lett.*, 45, 11,770-11,778,  
1618 <https://doi.org/10.1029/2018GL079751>, 2018.

1619  
1620 CReSIS: CReSIS radar depth sounder data, Digital Media, <http://data.cresis.ku.edu/>, 2016.

1621  
1622 Colgan, W., Rajaram, H., Abdalati, W., McCutchan, C., Mottram, R., Moussavi, M. S., and Grigsby, S.:  
1623 Observations, models, and mass balance implications: Glacier crevasses, *Rev. Geophys.*, 54, 119-161,  
1624 <https://doi.org/10.1002/2015RG000504>, 2016.

1625  
1626 Culberg, R., Schroeder, D.M. and Chu, W.: Extreme melt season ice layers reduce firn permeability across  
1627 Greenland, *Nat Commun*, 12, 2336, <https://doi.org/10.1038/s41467-021-22656-5>, 2021

1628  
1629 Culberg, R.: Refrozen melt layer location, density, and connectivity records from airborne radar sounding,  
1630 Greenland, NSF Arctic Data Center, <https://doi.org/10.18739/A2736M33V>, 2021.

1631  
1632 Cullather, R. I., Andrews, L. C., Croteau, M. J., Digirolamo, N. E., Hall, D. K., Lim, Y., Loomis, B. D.,  
1633 Shuman, C. A., and Nowicki, S. M. J.: Anomalous circulation in July 2019 resulting in mass loss on the  
1634 Greenland Ice Sheet. *Geophys. Res. Lett.*, 47, <https://doi.org/10.1029/2020GL087263>, 2020.

1635  
1636 Das, S. B., Joughin, I., Behn, M. D., Howat, I. M., King, M. A., Lizarralde, D., Bhatia, M. P., Fracture  
1637 propagation to the base of the Greenland Ice Sheet during supraglacial lake drainage, *Science*, 320, 778-  
1638 781, <https://doi.org/10.1126/science.1153360>, 2008.

1639 Drinkwater, M. R., Long, D. G., and Bingham, A. W.: Greenland snow accumulation estimates from satellite  
 1640 radar scatterometer data, *J. Geophys. Res. Atmos.*, 106, 33935-33950.  
 1641 <https://doi.org/10.1029/2001JD900107>, 2001.

1642  
 1643 Dunmire, D., Banwell, A. F., Lenaerts, J. T. M., and Datta, R. T.: Contrasting regional variability of buried  
 1644 meltwater extent over two years across the Greenland Ice Sheet, *The Cryosphere Discuss.*,  
 1645 <https://doi.org/10.5194/tc-2021-3>, in review, 2021.

1646  
 1647 Early, D. S., and Long, D. G.: Image reconstruction and enhanced-resolution imaging from irregular  
 1648 samples, *IEEE Trans. Geosci. Remote Sens.* 39, 291-302, <https://doi.org/10.1109/36.905237>, 2001.

1649  
 1650 Echelmeyer, K., Clarke, T. S., and Harrison, W. D.: Surficial glaciology of Jakobshavn Isbræ, West  
 1651 Greenland 1. Surface morphology, *J. Glaciol.*, 37, 368–382, <https://doi.org/10.1017/S002214300005803>,  
 1652 1991.

1653  
 1654 Entekhabi, D., et al.: The Soil Moisture Active Passive (SMAP) Mission, *Proc. IEEE*, 98, 704-716,  
 1655 <https://doi.org/10.1109/JPROC.2010.2043918>, 2010.

1656  
 1657 Fahnestock, M., Bindschadler, R., Kwok, R., and Jezek, K.: Greenland Ice Sheet surface properties and  
 1658 ice dynamics from ERS-1 SAR imagery. *Science*, 262, 1530-1534.  
 1659 <https://doi.org/10.1126/science.262.5139.1530>, 1993.

1660  
 1661 Forster, R. R., Box, J. E., Van Den Broeke, M. R., Miège, C., Burgess, E. W., Van Angelen, J. H., Lenaerts,  
 1662 J. T. M., Koenig, L. S., Paden, J., Lewis, C., Gogineni, S. P., Leuschen, C., and McConnell, J. R.: Extensive  
 1663 liquid meltwater storage in firn within the Greenland Ice Sheet, *Nat. Geosci.*, 7, 95–98,  
 1664 <https://doi.org/10.1038/ngeo2043>, 2014.

1665  
 1666 Fountain, A. G., and Walder, J. S.: Water flow through temperate glaciers. *Rev. of Geophys.*, 36, 299-328,  
 1667 <https://doi.org/10.1029/97RG03579>, 1998.

1668  
 1669 Freilich, M. H., Long, D. G., and Spencer, M. W.: SeaWinds: A scanning scatterometer for ADEOS-II  
 1670 science overview, *Proc. IEEE*, 1994, 960-963, <https://doi.org/10.1109/IGARSS.1994.399313>, 1994.

1671  
 1672 Franco, B., Fettweis, X., and Ericum, M.: Future projections of the Greenland ice sheet energy balance  
 1673 driving the surface melt, *The Cryosphere*, 7, 1–18, <https://doi.org/10.5194/tc-7-1-2013>, 2013

1674  
 1675 Goward, S. N., Masek, J. G., Williams, D. L., Irons, J. R., and Thompson, R. J.: The Landsat 7 mission:  
 1676 Terrestrial research and applications for the 21st century. *Remote Sensing of Environment*, 78, 3-12.  
 1677 [https://doi.org/10.1016/S0034-4257\(01\)00262-0](https://doi.org/10.1016/S0034-4257(01)00262-0), 2001.

1678  
 1679 Hall, D. K., and DiGirolamo, N.: Multilayer Greenland Ice Surface Temperature, Surface Albedo, and Water  
 1680 Vapor from MODIS, Version 1, NASA National Snow and Ice Data Center Distributed Active Archive Center,  
 1681 <https://doi.org/10.5067/7THUWT9NMPDK>, 2019.

1682  
 1683 Hall, D. K., Comiso, J. C., DiGirolamo, N. E., Shuman, C. A., Key, J. R., and Koenig, L. S.: A satellite-derived  
 1684 climate-quality data record of the clear-sky surface temperature of the Greenland Ice Sheet, *J. Clim.*, 25,  
 1685 4785–4798, <https://doi.org/10.1175/JCLI-D-11-00365.1>, 2012.

1686  
 1687 Hanna, E., Navarro, F. J., Whitehouse, P. L., Zwally, H. J., Pattyn, F., Domingues, C. M., Fettweis, X., Ivins,  
 1688 E. R., Nicholls, R. J., Ritz, C., Smith, B., and Tulaczyk, S.L.: Ice-sheet mass balance and climate change,  
 1689 *Nature*, 498, 51-59, <https://doi.org/10.1038/nature12238>, 2013.

1690  
 1691 Haran, T., Bohlander J., Scambos T., Painter, T., and Fahnestock, M.: MEaSUREs MODIS Boulder,  
 1692 Colorado USA. NASA National Snow and Ice Data Center Distributed Active Archive Center,  
 1693 <https://doi.org/10.5067/9Z079PHOTYE5>, 2018.

Formatted: Space Before: 0 pt

1693 Harper, J., Humphrey, N., Pfeffer, W. T., Brown, J., and Fettweis, X.: Greenland ice-sheet contribution to  
 1694 sea-level rise buffered by meltwater storage in firn, *Nature*, 491, 240–243,  
 1695 <https://doi.org/10.1038/nature11566>, 2012.

1696  
 1697 Hicks, B. R., and Long, D. G.: Inferring Greenland melt and refreeze severity from SeaWinds scatterometer  
 1698 data, *Int. J. Remote Sensing*, 32, 8053-8080, <https://doi.org/10.1080/01431161.2010.532174>, 2011.

1699  
 1700 Howat, I.: MEaSUREs Greenland Ice Mapping Project (GIMP) Land Ice and Ocean Classification Mask,  
 1701 Version 1, NASA National Snow and Ice Data Center Distributed Active Archive Center,  
 1702 <https://doi.org/10.5067/B8X58MQBFUPA>, 2017.

1703  
 1704 Howat, I., Negrete, A., and Smith, B.: MEaSUREs Greenland Ice Mapping Project (GIMP) Digital Elevation  
 1705 Model, Version 1, NASA National Snow and Ice Data Center Distributed Active Archive Center, doi:  
 1706 <https://doi.org/10.5067/NV34YUJXLP9W>, 2015.

1707  
 1708 Howat, I., Negrete, A., and Smith, B.: The Greenland Ice Mapping Project (GIMP) land classification and  
 1709 surface elevation datasets, *The Cryosphere*, 8, 1509-1518, <https://doi.org/10.5194/tc-8-1509-2014>, 2014.

1710  
 1711 Humphrey, N. F., Harper, J. T., and Pfeffer, W. T.: Thermal tracking of meltwater retention in Greenland's  
 1712 accumulation area, *J. Geophys. Res.*, 117, <https://doi.org/10.1029/2011JF002083>, 2012.

1713  
 1714 Jezek, K. C., Drinkwater M. R., Crawford, J. P., Bindshandler, R., and Kwok, R.: Analysis of synthetic  
 1715 aperture radar data collected over the southwestern Greenland Ice Sheet. *J. of Glaciol*, 39, 119-132,  
 1716 <https://doi.org/10.1017/S002214300001577X>, 1993.

1717  
 1718 Jezek, K. C., Gogineni, P., and Shanableh, M.: Radar measurements of melt zones on the Greenland Ice  
 1719 Sheet, *Geophys. Res. Lett.*, 21, 33-36, <https://doi.org/10.1029/93GL03377>, 1994.

1720  
 1721 Jezek, K. C., Johnson, J. T., Drinkwater, M. R., Macelloni, G., Tsang, L., Aksoy, M., and Durand M.:  
 1722 Radiometric approach for estimating relative changes in intraglacier average temperature, *IEEE Trans.*  
 1723 *Geosci. Remote Sens.*, 53, 134-143, <https://doi.org/10.1109/TGRS.2014.2319265>, 2015.

1724  
 1725  
 1726 Jezek, K. C., Johnson J. T., Tan S., Tsang L., Andrews, M. J., Brogioni, M., Macelloni, G., Durand, M.,  
 1727 Chen, C. C., Belgiovane, D. J., Duan, Y., Yardim, C., Li, H., Bringer, A., Leuski, V., and Aksoy, M.: 500–  
 1728 2000-MHz brightness temperature spectra of the northwestern Greenland Ice Sheet, *IEEE Trans. Geosci.*  
 1729 *Remote Sens.*, 56, 1485-1496, <https://doi.org/10.1109/TGRS.2017.2764381>, 2018.

1730  
 1731 Jones, W. L., Schroeder, L. C., Boggs, D. H., Bracalente, E. M., Brown, R. A., Dome, G. J., Pierson, W. J.,  
 1732 and Wentz, F. J.: The SEASAT-A satellite scatterometer: The geophysical evaluation of remotely sensed  
 1733 wind vectors over the ocean: *J. Geophys. Res. Oceans*, 87, 3297-3317,  
 1734 <https://doi.org/10.1029/JC087iC05p03297>, 1982.

1735  
 1736 Joughin, I., Das, S. B., Flowers, G. E., Behn, M. D., Alley, R. B., King, M. A., Smith, B. E., Bamber, J. L.,  
 1737 van den Broeke, M. R., and Van Angelen, J. H.: Influence of ice-sheet geometry and supraglacial lakes on  
 1738 seasonal ice-flow variability, *The Cryosphere*, 7, 1185-1192, <https://doi.org/10.5194/tc-7-1185-2013>, 2013.

1739  
 1740 Joughin, I., Das, S. B., King, M. A., Smith, B. E., Howat, I. M., and Moon, T.: Seasonal speedup along the  
 1741 western flank of the Greenland Ice Sheet, *Science*, 320, 781-783, <https://doi.org/10.1126/science.1153288>,  
 1742 2008.

1743  
 1744 Kerr, Y. H., Waldteufel, P., Wigneron, J., Martinuzzi, J., Font, J., and Berger, M.: Soil moisture retrieval from  
 1745 space: The Soil Moisture and Ocean Salinity (SMOS) mission, *IEEE Trans. Geosci. Remote Sens.*, 39,  
 1746 1729-1735, <https://doi.org/10.1109/36.942551>, 2001.

1747

Formatted: Space Before: 0 pt

1748 Koenig, L. S., Miège, C., Forster, R. R., and Brucker, L.: Initial in situ measurements of perennial meltwater  
1749 storage in the Greenland firn aquifer, *Geophys. Res. Lett.*, 41, 81-85,  
1750 <https://doi.org/10.1002/2013GL058083>, 2014.

1751  
1752 Kuipers Munneke, P. K., Ligtenberg, S. R. M., Van Den Broeke, M. R., Van Angelen, J. H., and Forster, R.  
1753 R.: Explaining the presence of perennial liquid water bodies in the firn of the Greenland Ice Sheet, *Geophys.*  
1754 *Res. Lett.*, 41, 476–483, <https://doi.org/10.1002/2013GL058389>, 2014.

1755  
1756 Le Vine, D. M., Lagerloef, G. S. E., and Torrusio, S. E.: Aquarius and remote sensing of sea surface salinity  
1757 from space, *Proc. IEEE*, 98, 688-703, <https://doi.org/10.1109/JPROC.2010.2040550>, 2010.

1758  
1759 Lewis, C., Gogineni, S., Rodriguez-Morales, F., Panzer, B., Stumpf, T., Paden, J., and Leuschen, C.:  
1760 Airborne fine-resolution UHF radar: An approach to the study of englacial reflections, firn compaction and  
1761 ice attenuation rates, *J. Glaciology*, 61, 89-100. <https://doi.org/10.3189/2015JoG14J089>, 2015.

1762  
1763 Long, D. G., Brodzik, M. J., and Hardman M. A.: Enhanced-resolution SMAP brightness temperature image  
1764 products, *IEEE Trans. Geosci. Remote Sens.*, 57, 4151-4163,  
1765 <https://doi.org/10.1109/TGRS.2018.2889427>, 2019.

1766  
1767 Long, D. G., and Brodzik, M. J.: Optimum image formation for spaceborne microwave radiometer products,  
1768 *IEEE Trans. Geosci. Remote Sens.*, 54, 2763-2779. <https://doi.org/10.1109/TGRS.2015.2505677>, 2016.

1769  
1770 Long, D. G., and Daum, D. L.: Spatial resolution enhancement of SSM/I data, *IEEE Trans. Geosci. Remote*  
1771 *Sens.*, 36, 407-417, <https://doi.org/10.1109/36.662726>, 1998.

1772  
1773 Long, D. G., and Drinkwater, M. R.: Greenland Ice Sheet surface properties observed by the Seasat-A  
1774 scatterometer at enhanced resolution, *J. Glaciol.*, 40, 213-230,  
1775 <https://doi.org/10.1017/S0022143000007310>, 1994.

1776  
1777 Long, D. G., Hardin, P. J., and Whiting, P. T.: Resolution enhancement of spaceborne scatterometer data,  
1778 *IEEE Trans. Geosci. Remote Sens.*, 31, 700-715, <https://doi.org/10.1109/36.225536>, 1993.

1779  
1780  
1781 MacFerrin, M., Machguth, H., van As, D., Charalampidis, C., Stevens, C. M., Heilig, A., Vandecrux, B.,  
1782 Langen, P. L., Mottram, R., Fettweis, X., van den Broeke, M. R., Pfeffer, W. T., Moussavi, M. S., and  
1783 Abdalati, W.: Rapid expansion of Greenland's low-permeability ice slabs. *Nature*, 573, 403-407,  
1784 <https://doi.org/10.1038/s41586-019-1550-3>, 2019.

1785  
1786 Machguth, H. ~~MacFerrin~~ MacFerrin M., van As, D., Box, J. E., Charalampidis, C., Colgan, W., Fausto, R.  
1787 S., Harro, A. J., Mosley-Thompson, E., and van de Wal, R. S. W.: Greenland meltwater storage in firn  
1788 limited by near-surface ice formation. *Nat. Clim. Chang.* 6, 390-393, <https://doi.org/10.1038/nclimate2899>,  
1789 2016.

1790  
1791 Mätzler, C., and Hüppi, R.: Review of signature studies for microwave remote sensing of snowpacks, *Adv.*  
1792 *in Space Res.*, 9, 253-265, [https://doi.org/10.1016/0273-1177\(89\)90493-6](https://doi.org/10.1016/0273-1177(89)90493-6), 1989.

1793  
1794 Miège, C., Forster, R. R., Brucker, L., Koenig, L. S., Solomon, D.K., Paden, J. D., Box, J. E., Burgess, E.  
1795 W., Miller, J. Z., McNerney, L., Brautigam, N., Fausto, R. S., and Gogineni, S.: Spatial extent and temporal  
1796 variability of Greenland firn aquifers detected by ground and airborne radars, *J. Geophys. Res. Earth*, 121,  
1797 2381–2398, <https://doi.org/10.1002/2016JF003869>, 2016.

1798  
1799 Miles, K. E., Willis, I. C., Benedek, C. L., Williamson, A. G., and Tedesco, M.: Toward monitoring surface  
1800 and subsurface lakes on the Greenland Ice Sheet Using Sentinel-1 SAR and Landsat-8 OLI imagery,  
1801 *Frontiers in Earth Science*, 5, 58, <https://doi.org/https://doi.org/10.3389/feart.2017.00058>, 2017.

1802



1803 Miller, J. Z., Long, D. G., Jezek, K. C., Johnson, J. T., Brodzik, M. J., Shuman, C. A., Koenig, L. S., and  
1804 Scambos, T. A.: Brief communication: Mapping Greenland's perennial firn aquifers using enhanced-  
1805 resolution L-band brightness temperature image time series, *The Cryosphere*, 14, 2809–2817,  
1806 <https://doi.org/10.5194/tc-14-2809-2020>, 2020.  
1807  
1808 Miller, J. Z.: Mapping Greenland's firn aquifers from space using active and passive satellite microwave  
1809 remote sensing, Ph.D. thesis, Department of Geography, University of Utah, 135 pp., 2019.  
1810  
1811 Miller, O. L., Solomon, D. K., Miège, C., Koenig, L. S., Forster, R. R., Montgomery, L. N., Schmerr, N.,  
1812 Ligtenberg, S. R. M., Legchenko, A., and Brucker, L.: Hydraulic conductivity of a firn aquifer in southeast  
1813 Greenland, *Front. Earth Sci.*, 5, <https://doi.org/10.3389/feart.2017.00038>, 2017.  
1814  
1815 Montgomery, L. N., Schmerr, N., Burdick, S., Forster, R. R., Koenig, L., Legchenko, A., Ligtenberg, S.,  
1816 Miège, C., Miller, O. L., and Solomon, D. K.: Investigation of firn aquifer structure in southeastern Greenland  
1817 using active source seismology, *Front. Earth Sci.*, 5, <https://doi.org/10.3389/feart.2017.00010>, 2017.  
1818  
1819 Moon, T., Joughin, I., Smith, B., Broeke, M. R., Berg, W. J., Noël, B., and Usher, M.: Distinct patterns of  
1820 seasonal Greenland glacier velocity, *Geophys. Res. Lett.*, 41, 7209–7216,  
1821 <https://doi.org/10.1002/2014GL061836>, 2014.  
1822  
1823 Mote, T. L., and Andersen, M. R.: Variations in snowpack melt on the Greenland Ice Sheet based on passive  
1824 microwave measurements, *J. Glaciology*, 41, 51–60, <https://doi.org/10.1017/S0022143000017755>, 1995.  
1825  
1826 Noël, B., van Kampenhout, L., Lenaerts, J. T. M., van de Berg, W. J., and van den Broeke, M. R.: A 21st  
1827 century warming threshold for sustained Greenland Ice Sheet mass loss, *Geophys. Res. Lett.*, 48(5),  
1828 <https://doi.org/10.1029/2020GL090471>, 2021.  
1829  
1830 Noël, B., van de Berg, Willem Jan, Lhermitte, S. L. M., and van den Broeke, Michiel R.: Rapid ablation zone  
1831 expansion amplifies north Greenland mass loss, *Sci. Adv.*, 5, eaaw0123,  
1832 <https://doi.org/10.1126/sciadv.aaw0123>, 2019.  
1833  
1834 Noël, B., van de Berg, W. J., van Wessem, J. M., van Meijgaard, E., van As, D., Lenaerts, J. T. M., Lhermitte,  
1835 S., Kuipers Munneke, P., Smeets, C. J. P. P., van Uffl, L. H., van de Wal, R. S. W., and van den Broeke,  
1836 M. R.: Modelling the climate and surface mass balance of polar ice sheets using RACMO2 – Part 1:  
1837 Greenland (1958–2016), *The Cryosphere*, 12, 811–831, <https://doi.org/10.5194/tc-12-811-2018>, 2018.  
1838 Nghiem, S. V., Hall, D. K., Mote, T. L., Tedesco, M., Albert, M. R., Keegan, K., Shuman, C. A., DiGirolamo,  
1839 N. E., & Neumann, G.: The extreme melt across the Greenland Ice Sheet in 2012, *Geophys. Res. Lett.*,  
1840 39, <https://doi.org/10.1029/2012GL053611>, 2003  
1841  
1842 Nghiem, S. V., Hall, D. K., Mote, T. L., Tedesco, M., Albert, M. R., Keegan, K., Shuman, C. A., DiGirolamo,  
1843 N.E., and Neumann, G.: The extreme melt across the Greenland Ice Sheet in 2012, *Geophys. Res. Lett.*,  
1844 39, L20502, <https://doi.org/10.1029/2012GL053611>, 2012.  
1845  
1846 Paden, J., Li, J., Leuschen C., F. Rodriguez-Morales, F., and Hale, R.: IceBridge Accumulation Radar L1B  
1847 Geolocated Radar Echo Strength Profiles, Version 2, NASA National Snow and Ice Data Center Distributed  
1848 Active Archive Center, <https://doi.org/10.5067/OZY1XYHNIQNY>, 2014, updated 2018.  
1849 Partington, K. C.: Discrimination of glacier facies using multi-temporal SAR data. *J. Glaciol.*, 44, 42–53.  
1850 <https://doi.org/10.3189/S0022143000002331>, 1998.  
1851  
1852 Pfeffer, W. T., Meier, M. F., and Illangasekare, T. H.: Retention of Greenland runoff by refreezing:  
1853 Implications for projected future sea level change. *J. Geophys. Res. Oceans*, 96, 22117–22124,  
1854 <https://doi.org/10.1029/91JC0250>, 1991.  
1855  
1856 Pfeffer, W. T., and Humphrey, N.F.: Determination of timing and location of water movement and ice-layer  
1857 formation by temperature measurements in sub-freezing snow, *J. Glaciol.*, 42, 292–304,  
1858 <https://doi.org/10.1017/S0022143000004159>, 1996.

1859  
1860 Piepmeier, J. R., et al.: SMAP L-band microwave radiometer: Instrument design and first year on orbit.  
1861 IEEE Trans. Geosci. Remote Sens., 55, 1954-1966, <https://doi.org/10.1109/TGRS.2016.2631978>, 2017.  
1862  
1863 Poinar, K., Joughin, I., Lilien, D., Brucker, L., Kehrl, L., and Nowicki, S.: Drainage of southeast Greenland  
1864 firn aquifer water through crevasses to the bed. Front. Earth Sci., <https://doi.org/10.3389/feart.2017.00005>,  
1865 2017.  
1866  
1867 Poinar, K., Dow, C. F., and Andrews, L. C.: Long-term support of an active subglacial hydrologic system in  
1868 southeast Greenland by firn aquifers. Geophys. Res. Lett., 46, 4772-4781,  
1869 <https://doi.org/10.1029/2019GL082786>, 2019.  
1870  
1871 Rignot, E.: Backscatter model for the unusual radar properties of the Greenland Ice Sheet, J. Geophys.  
1872 Res. Planets, 100, 9389–9400, <https://doi.org/10.1029/95JE00485>, 1995.  
1873  
1874 Rignot, E. J., Ostro, S. J., Van Zyl, J., and Jezek, K. C.: Unusual radar echoes from the Greenland Ice  
1875 Sheet, Science, 261, 1710-1713, <https://doi.org/10.1126/science.261.5129.171>, 1993.  
1876  
1877 Rodriguez-Morales, F., et al.: Advanced multi-frequency radar instrumentation for polar research, IEEE  
1878 Trans. Geosci. Remote Sens., 52, 2824-2842, <https://doi.org/10.1109/TGRS.2013.2266415>, (2014).  
1879  
1880 Schröder L., Neckel N., Zindler R., Humbert A.: Perennial supraglacial lakes in northeast Greenland  
1881 observed by polarimetric SAR, Remote Sensing, 12, 2798, <https://doi.org/10.3390/rs12172798> (2020).  
1882  
1883 Shuman, C. A., Hall, D. K., DiGirolamo, N. E., Mefford T. K., and Schnaubelt, M. J.: Comparison of near-  
1884 surface air temperatures and MODIS ice-surface temperatures at Summit, Greenland (2008–2013), J. Appl.  
1885 Meteor. Climatol., 53, 2171-2180, <https://doi.org/10.1175/JAMC-D-14-0023.1>, 2014.  
1886  
1887 Steffen, K., Nghiem, S. V., Huff, R., and Neumann, G.: The melt anomaly of 2002 on the Greenland Ice  
1888 Sheet from active and passive microwave satellite observations. Geophys. Res. Lett., 31, L2040,  
1889 <https://doi.org/10.1029/2004GL020444>, 2004.  
1890  
1891 Stevens, L. A., Behn, M. D., McGuire, J. J., Das, S. B., Joughin, I., Herring, T., Shean, D. E., and King, M.  
1892 A.: Greenland supraglacial lake drainages triggered by hydrologically induced basal slip, Nature, 522, 73-  
1893 76. <https://doi.org/10.1038/nature14480>, 2015.  
1894  
1895 Swift, C. T., Hayes, P. S., Herd, J. S., Jones, W. L., and Delnore, V. E.: Airborne microwave measurements  
1896 of the southern Greenland Ice Sheet, J. Geophys. Res. Solid Earth, 90, 1983-1994,  
1897 <https://doi.org/10.1029/JB090iB02p01983>, 1985.  
1898  
1899 Tedesco, M., and Fettweis, X.: Unprecedented atmospheric conditions (1948–2019) drive the 2019  
1900 exceptional melting season over the Greenland Ice Sheet, The Cryosphere, 14, 1209-1223,  
1901 <https://doi.org/10.5194/tc-14-1209-2020>, 2020.  
1902  
1903 Tedesco, M., Mote, T., Fettweis, X., Hanna, E., Jeyaratnam, J., Booth, J. F., Datta, R., and Briggs, K.: Arctic  
1904 cut-off high drives the poleward shift of a new Greenland melting record, Nature Commun., 7, 11723-11723,  
1905 <https://doi.org/10.1038/ncomms11723>, 1985, 2016.  
1906  
1907 Tedesco, M., Fettweis, X., van den Broeke, M. R., van de Wal, R. S. W., Smeets, C. J. P. P., van de Berg,  
1908 W. J., Serreze, M. C., and Box, J. E.: The role of albedo and accumulation in the 2010 melting record in  
1909 Greenland, Environ. Res. Lett., 6, 014005, <https://doi.org/10.1088/1748-9326/6/1/014005>, 2011.  
1910  
1911 Tedesco, M., Serreze, M., and Fettweis, X.: Diagnosing the extreme surface melt event over southwestern  
1912 Greenland in 2007. The Cryosphere, 2, 159-166. <https://doi.org/10.5194/tc-2-159-2008>, 2008.  
1913

1914 Tiuri, M. E., Sihvola, A. H., Nyfors, E. G., Hallikaiken, M. T.: The complex dielectric constant of snow at  
1915 microwave frequencies, IEEE J. Ocean Eng, 9, 377-382, <https://doi.org/10.1109/JOE.1984.1145645>, 1984.  
1916  
1917 Tsai, W., Nghiem, S. V., Van Zyl, J. J.: SeaWinds scatterometer on QuikSCAT mission and the emerging  
1918 land and ocean applications, Proc. SPIE 4152, <https://doi.org/10.1117/12.410586>, 2000.  
1919  
1920 Trusel, L. D., Das, S. B., Osman, M. B., Evans, M. J., Smith, B. E., Fettweis, X., McConnell, J. R., Noël, B.  
1921 P. Y., and van den Broeke, M. R.: Nonlinear rise in Greenland runoff in response to post-industrial Arctic  
1922 warming, Nature, 564, 104-108, <https://doi.org/10.1038/s41586-018-0752-4>, 2018.  
1923  
1924 Turton, J. V., Hochreuther, P., Reimann, N., and Blau, M. T.: The distribution and evolution of supraglacial  
1925 lakes on the 79° N Glacier (northeast Greenland) and interannual climatic controls, The Cryosphere  
1926 Discuss, <https://doi.org/10.5194/tc-2021-45>, in review, 2021.  
1927  
1928 Ulaby, F. T., Long, D. G., Blackwell, W. J., Elachi, C., Fung, A. K., Ruf, C., Sarabandi, C., Zebker, H. A.,  
1929 Van Zyl, J.: Microwave radar and radiometric remote sensing, University of Michigan Press, Ann Arbor,  
1930 2014.  
1931  
1932 van den Broeke, M. R., Enderlin, E. M., Howat, I. M., Kuipers Munneke, P., Noël, B. P. Y., van de Berg, W.  
1933 J., van Meijgaard, E., and Wouters, B.: On the recent contribution of the Greenland ice sheet to sea level  
1934 change, The Cryosphere, 10, 1933–1946, <https://doi.org/10.5194/tc-10-1933-2016>, 2016.  
1935  
1936 van der Veen, C. J.: Fracture propagation as means of rapidly transferring surface meltwater to the base  
1937 of glaciers, Geophys. Res. Lett., 34, L01501, <https://doi.org/10.1029/2006GL028385>, 2005.  
1938  
1939 Wessel, P., and Smith, W. H. F.: A global, self-consistent, hierarchical, high-resolution shoreline database,  
1940 J. Geophys. Res., 101, 8741–8743, <https://doi.org/10.1029/96JB00104>, 1996.  
1941  
1942 Zabel, I. H. H., Jezek, K. C., Baggeroer, P. A., and Gogineni, S. P.: Ground-based radar observations of  
1943 snow stratigraphy and melt processes in the percolation facies of the Greenland Ice Sheet, Ann. Glaciol.,  
1944 21, 40-44. <https://doi.org/10.3189/S0260305500015573>, 1995.  
1945  
1946 Zwally, H. J., Abdalati, W., Herring, T., Larson, K., Saba, J., and Steffen, K.: Surface melt-induced  
1947 acceleration of Greenland Ice Sheet flow, Science, 297, 218-222, <https://doi.org/10.1126/science.1072708>,  
1948 2002.  
1949  
1950 Zwally, J. H.: Microwave emissivity and accumulation rate of polar firn, J. Glaciol., 18, 195-215,  
1951 <https://doi.org/10.1017/S0022143000021304>, 1977.

Formatted: Space Before: 0 pt

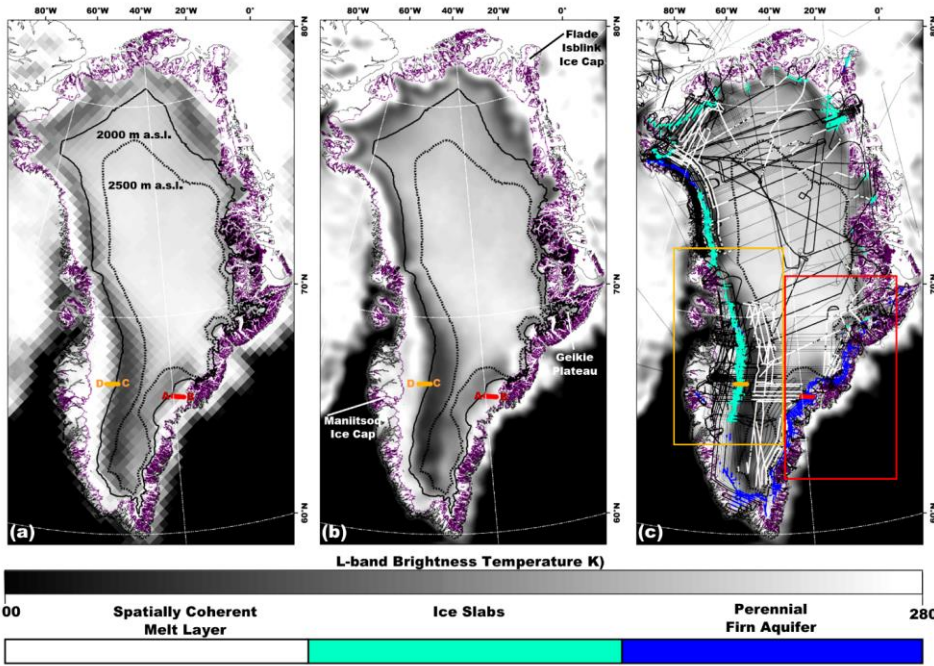


**Figure 1**

(a) Gridded (25 km gridding, 30 km effective resolution), and (b) enhanced-resolution (3.125 km gridding, 18 km effective resolution) L-band  $T_V^B$  imagery generated using observations collected 15 April 2016 by the microwave radiometer on the SMAP satellite during the evening orbital pass interval over Greenland (Long et al., 2019), overlaid with the 2000 m a.s.l. contour (black line), and the 2500 m a.s.l. contour (dotted black line; Howat et al., 2014); the ice sheet extent (purple line; Howat et al., 2014); and the coastline (black peripheral line; Wessel and Smith, 1996). (c) SMAP enhanced-resolution L-band  $T_V^B$  imagery overlaid with AR- and MCoRDS-derived 2010-2017 perennial firn aquifer (blue shading; Miège et al., 2016), 2010-2014 ice slab (cyan shading; MacFerrin et al., 2019), and 2012 spatially coherent melt layer (white shading; Culberg et al., 2021) detections along OIB flight lines (black interior lines); zoom areas over south eastern Greenland (red box; Fig. 2a), and south western Greenland (orange box; Fig. 2b); and AR radargram transect A-B (red line; Fig. 3a) and C-D (orange line; Fig. 3b).

Formatted: Not Highlight

Formatted: Left

Formatted: Not Highlight

Formatted: Not Highlight

Formatted: Not Highlight

Formatted: Not Highlight

Formatted: Not Highlight

Formatted: Not Highlight

Formatted: Not Highlight

Formatted: Not Highlight

Formatted: Not Highlight

Formatted: Not Highlight

Formatted: Not Highlight

Formatted: Not Highlight

Formatted: Not Highlight

Formatted: Not Highlight

Formatted: Not Highlight

Formatted: Not Highlight

Formatted: Not Highlight

Formatted: Not Highlight

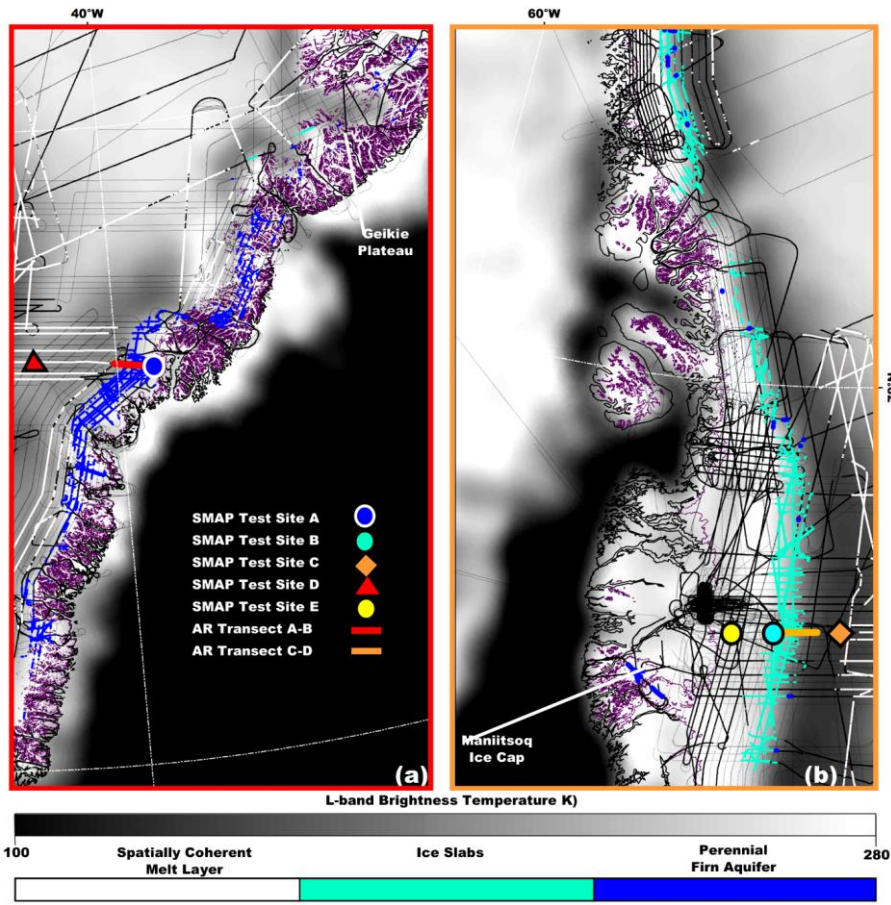


**Figure 2**

Enhanced-resolution (3.125 km gridding, 30 km effective resolution) L-band  $T_v^B$  imagery generated using observations collected 15 April 2016 by the microwave radiometer on the SMAP satellite during the evening orbital pass interval over (a) south eastern Greenland (red box, Fig. 1c), and (b) south western Greenland (orange box, Fig. 1c.) (Long et al., 2019) overlaid with the ice sheet extent (purple line; Howat et al., 2014); the coastline (black peripheral line; Wessel and Smith, 1996); the AR- and MCoRDS-derived 2010-2017 perennial firn aquifer (blue shading; Miège et al., 2016), 2010-2014 ice slab (cyan shading; MacFerrin et al., 2019), and 2012 spatially coherent melt layer (white shading; Culberg et al., 2021) detections along OIB flight lines (black interior lines); AR transect A-B (red line; Fig. 3a), and C-D (orange line; Fig. 3b); and SMAP Test Site A (blue circle; Fig. 4a), B (cyan circle; Fig. 4b), C (orange diamond; Fig. 4c), D (red triangle; Fig. 4d), and E (yellow circle; Fig. 4e).

Perennial Firn Aquifers and Ice Slabs, Perched Firn Aquifers

Formatted: Font: Arial

Formatted: Centered, Space Before: 10 pt

Formatted: Not Highlight

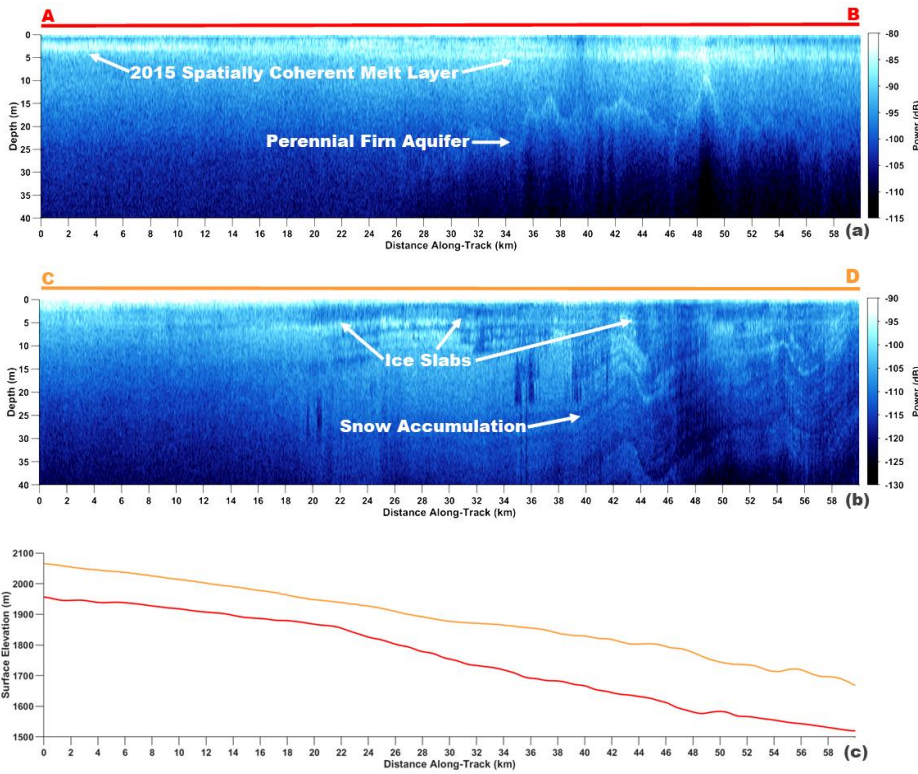
Formatted: Not Highlight

Formatted: Not Highlight

Formatted: Not Highlight

Formatted: Not Highlight





1977  
 1978 **Figure 3**  
 1979 *AR transect radargram profile (Rodríguez-Morales et al. 2014) (a) along perennial firn aquifer transect A-B*  
 1980 *(red line, Figs. 4; 22a) that was collected on 22 April 2017, and (b) ice slab transect C-D (orange line,*  
 1981 *Figs. 4; 22b) that was collected on 5 May 2017 (Rodríguez-Morales et al. 2014). (c) The corresponding*  
 1982 *perennial firn aquifer AR transect A-B elevation profile (red line), and (d) ice slab transect C-D (orange*  
 1983 *line) elevation profiles (orange line). The exceptionally bright upper surface-parallel reflector in (a) is*  
 1984 *interpreted as a spatially coherent melt layer. The that formed following the 2015 melting season. The*  
 1985 *bright lower reflector in (a) is the interpreted as the upper surface of meltwater stored within a perennial*  
 1986 *firn aquifer. The thick dark surface-parallel regions of low-reflectivity in (b) are interpreted as ice slabs.*  
 1987 *The alternating sequences of bright and dark surface-parallel reflectors in (b) are interpreted as*  
 1988 *seasonal snow accumulation layers. A first maximum after maximum gradient re-tracker is used to identify*  
 1989 *the surface return in each profile. Each profile is flattened so that the depth axis is measured relative to the*  
 1990 *local elevation. Corresponding elevation profiles in (c) are calculated by subtracting the radar-measured*  
 1991 *flight clearance over the ice sheet from the aircraft's global positioning system altitude measurements that*  
 1992 *were coincidentally collected along each transect.*

Formatted: Centered

Formatted: Font: 10 pt, Not Highlight

Formatted: Font: 10 pt

Formatted: Not Highlight

Formatted: Not Highlight

Formatted: Not Highlight

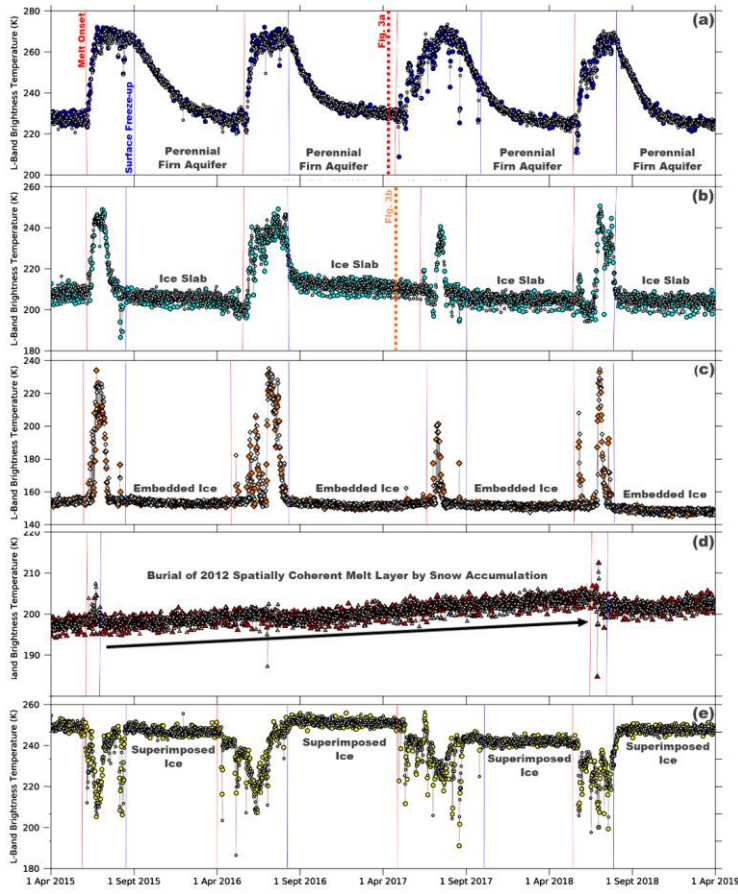


**Figure 4**

*Temporal L-band signatures that alternate morning (white symbols) and evening (colored symbols) orbital pass interval enhanced-resolution  $T_V^B$  generated using observations collected over the GRIS by the microwave radiometer on the SMAP satellite (Brodzik et al., Long et al., 2019) over (a) perennial firn aquifer SMAP Test Site A area (blue circles; Figs. 2a; 3a), (b) perched firn aquifer B area (cyan circles; Figs. 2b; 3b), (c) percolation facies area C (orange diamonds; Fig. 2b), (d) high-elevation (~2500 m.a.s.l.) spatially coherent melt layer D area (red triangles; Fig. 2a), and (e) superimposed ice E area (yellow circles; Fig. 2b). Melt onset (red lines) and surface freeze-up (blue lines) dates are derived from thermal infrared  $T^B$  collected by MODIS on the Terra and Aqua satellites (Hall et al., 2012). AR radargram profile along perennial firn aquifer transect A-B (red dashed line; Figs. 1; 2a; 3a) that was collected on 22 April 2017, and ice slab transect C-D (orange dashed line; Fig. 1; 2b; 3b) that was collected on 5 May 2017.*

Formatted: Centered

Formatted: Font: 10 pt



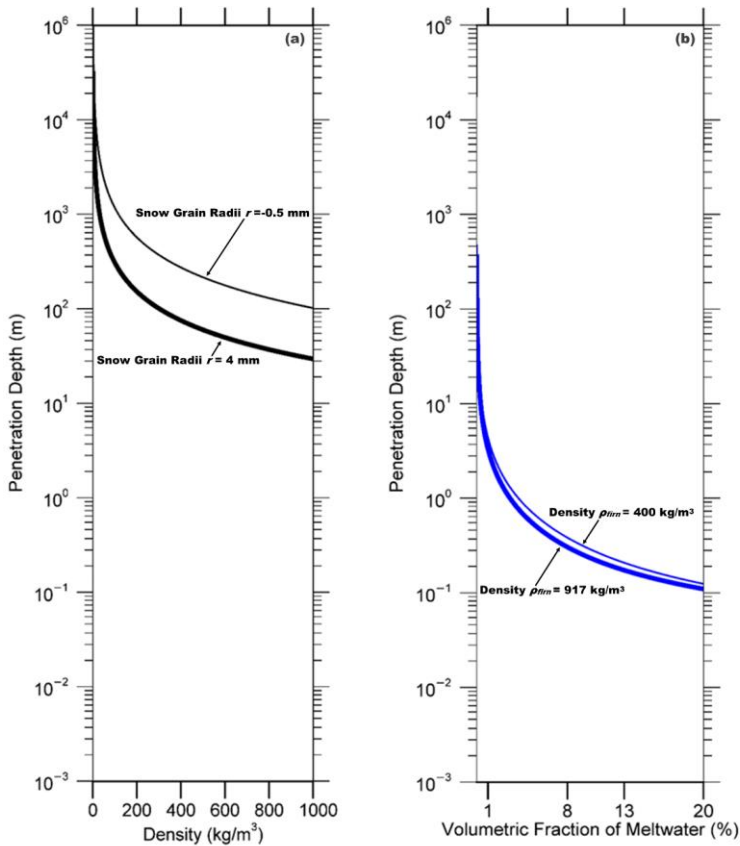


**Figure 5**

Theoretical L-band penetration depths for of uniform layer of (a) refrozen, and (b) water-saturated firn. Penetration depths  $\left(\frac{1}{\kappa_s + \kappa_d}\right)$  are calculated as a function of the Raleigh scattering coefficient ( $\kappa_s$ ; Eq. 8) and the absorption coefficient ( $\kappa_d$ ; Eq. 10), which are functions of the dielectric and geophysical properties of the GHS. The complex dielectric constant is calculated using the empirically derived models described in Tiuri et al., (1984). Refrozen firn penetration depths are calculated as a function of firn density ( $\rho_{firn}$ ), and the curves are plotted for snow grain radii ( $r$ ) set to  $r=0.5$  mm (upper curve), and  $r=4$  mm (lower curve). Water-saturated firn penetration depths are calculated as a function of the volumetric fraction of meltwater ( $m_v$ ), and the curves are plotted for firn density set to  $\rho_{firn}=400$  kg/m<sup>3</sup> (upper curve), and  $\rho_{firn}=917$  kg/m<sup>3</sup> (lower curve). Given the complexity of modeling embedded ice structures, they are excluded from the penetration depth calculation. Increases in the volumetric fraction of embedded ice within the firn will result

Formatted: Centered

Formatted: Font: 10 pt

Formatted: Not Highlight

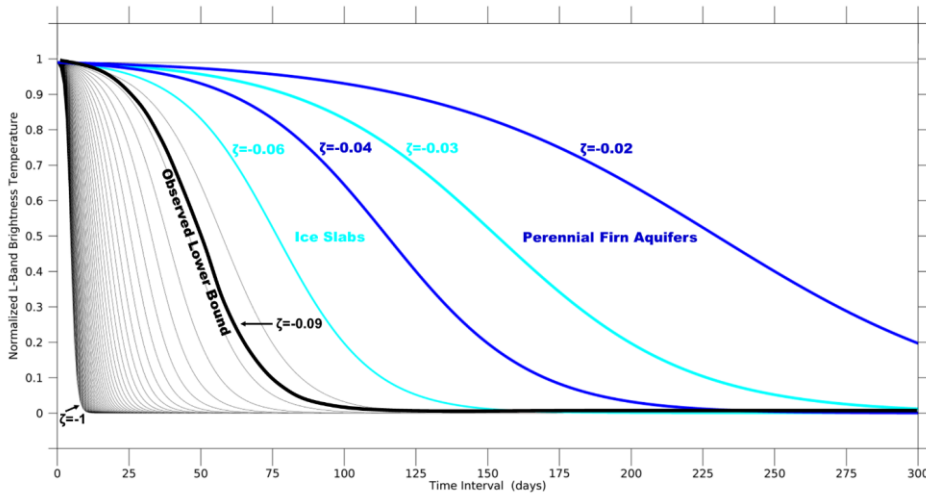
Formatted: Not Highlight

Formatted: Not Strikethrough

Formatted: Not Strikethrough

2017 *in an increase in volume scattering, which will decrease and compress the distance between the penetration*  
2018 *depth curves for both refrozen and water-saturated firn. Given the complexity of modeling embedded ice*  
2019 *structures, they are excluded from the penetration depth calculation. Increases in the volumetric fraction of*  
2020 *embedded ice in the firn will result in an increase in volume scattering, which will decrease and compress*  
2021 *the distance between the penetration depth curves for both refrozen and water-saturated firn.*

2022



2023

2024 **Figure 6**

2025

2026 *Example set of simulated sigmoidal curves that represent our model of the exponentially*  
 2027 *decreasing temporal L-band signatures predicted over the percolation facies. The initial*  
 2028 *normalized vertically-polarized L-band brightness temperature was fixed at a value of  $T_{V,N}^B(t_{max})$*   
 2029 *= 0.99, and the time interval was set to a value of  $t \in [t_{max}, t_{min}] = 300$  observations. The*  
 2030 *refreezing rate parameter was set to values between  $\zeta = [-1, 0]$  incremented by steps of 0.02.*  
 2031 *The blue lines correspond to the interval  $\zeta \in [-0.04, -0.02]$  and produce curves similar to those*  
 2032 *observed over perennial firn aquifer areas. The cyan lines correspond to the interval  $\zeta \in [-0.06,$   
 2033 *-0.03] and produce curves similar to those observed over ice slab areas. The green lines*  
 2034 *correspond to the interval  $\zeta \in [-0.04, -0.03]$  and produce curves similar to those observed over*  
 2035 *perched firn aquifer areas. The black line is the observed lower bound ( $\zeta = -0.09$ ) of the refreezing*  
 2036 *rate parameter of partitioned  $T_{V,N}^B$  time series (1 April 2015 – 31 March 2019) iteratively fit to the*  
 2037 *sigmoid function (see Section 2.3.43).**

2038

Formatted: Centered

Formatted: Font: 10 pt

Formatted: Font: 10 pt

Formatted: Space Before: 0 pt

Formatted: Font: 11 pt

Formatted: No Spacing

Formatted: Font: Italic

Formatted: Font: Italic

Formatted: Font: Italic

Formatted: Font: Italic

Formatted: Font: Italic

Formatted: Font: Italic

Formatted: Font: Italic

Formatted: Font: Italic

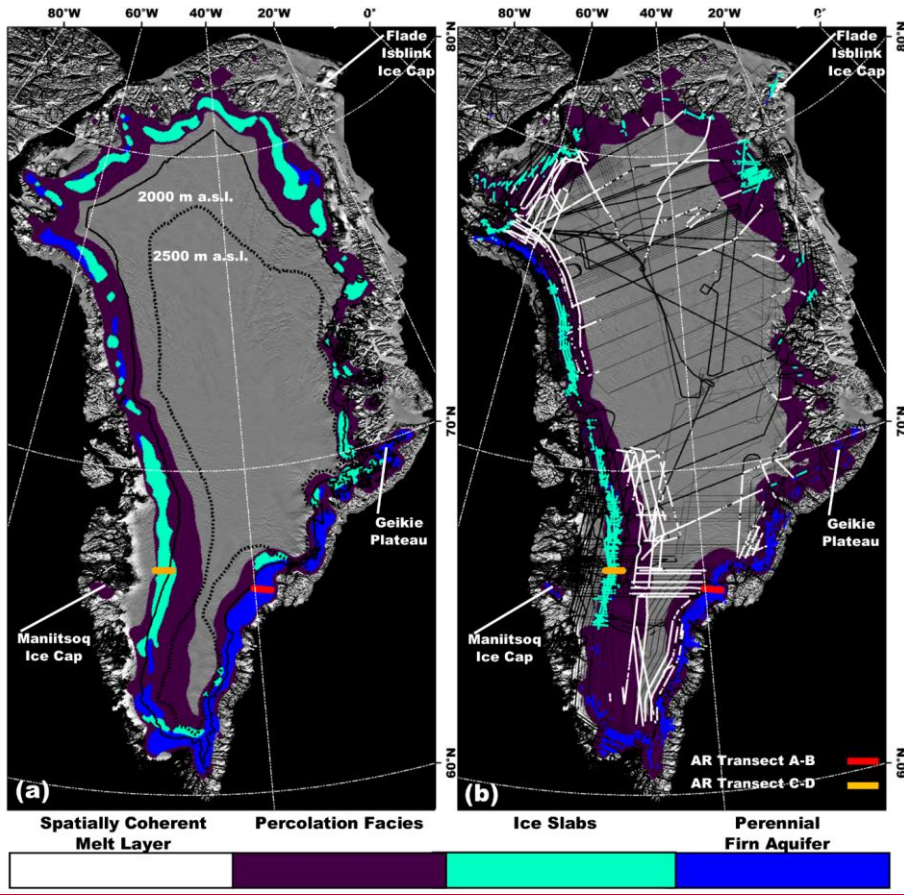
Formatted: Font: Italic

Formatted: Font: Italic

Formatted: Font: Italic

Formatted: Font: Italic

2039



Formatted: Centered

2040

2041

**Figure 7**

2042

2043

2044

2045

2046

2047

2048

2049

(a) SMAP-derived perennial firn aquifer (blue shading), ice slab (cyan shading), and percolation facies (purple shading) extents (2015-2019) generated by the adapted empirical algorithm; and the 2000 m a.s.l. contour (black line), and the 2500 m a.s.l. contour (black dotted line; Howat et al., 2014) overlaid on the 2015 MODIS Mosaic of Greenland (MOG) image map (Haran et al., 2018). (b) SMAP-derived extents are overlaid with AR- and MCoRDS-derived 2010-2017 perennial firn aquifer (blue shading; Miège et al., 2016), 2010-2014 ice slab (cyan shading; MacFerrin et al., 2019), and 2012 spatially coherent melt layer (white shading; Culberg et al., 2021) detections along OIB flight lines (black interior lines); and AR transect A-B (red line; Fig. 3a), and C-D (orange line; Fig. 3b).

Formatted: Font: 10 pt

Formatted: Left

Formatted: Line spacing: 1.5 lines

Formatted: Not Highlight

Formatted: Not Highlight

Formatted: Not Highlight

Formatted: Not Highlight

Formatted: Not Highlight

Formatted: Not Highlight

Formatted: Not Highlight

Formatted: Not Highlight

Formatted: Not Highlight

Formatted: Not Highlight

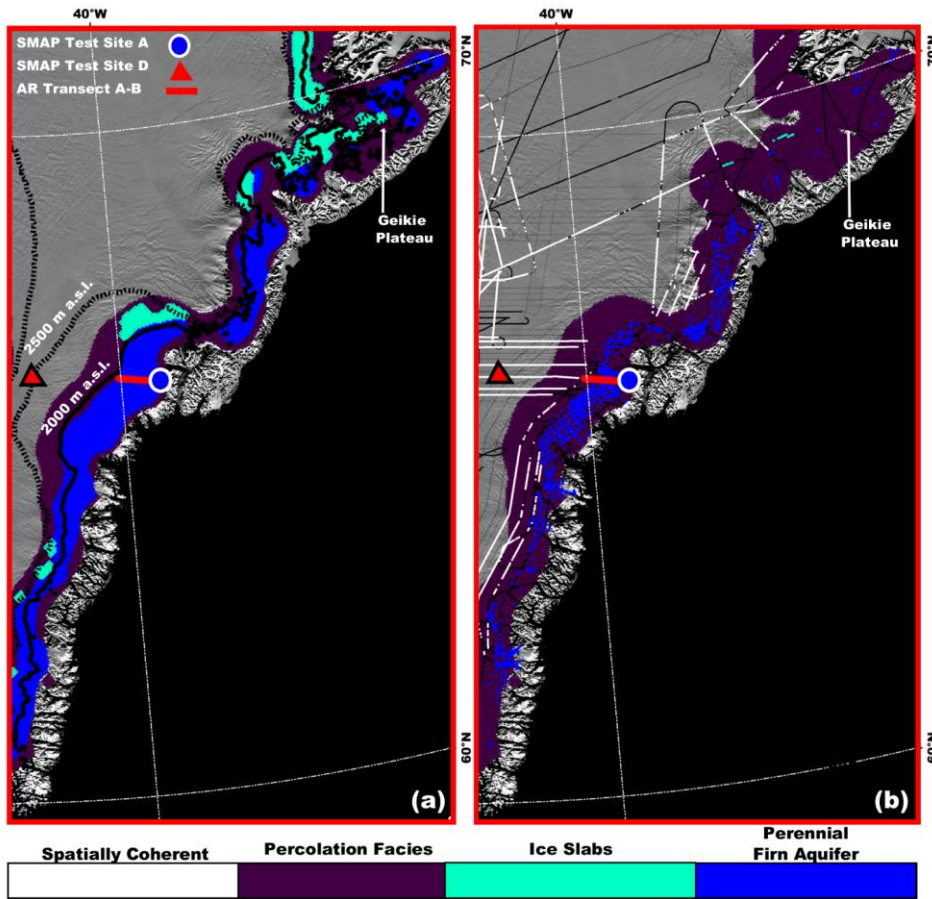


**Figure 8**

*The SMAP-derived perennial firn aquifer (blue shading), ice slab (cyan shading), and percolation facies (purple shading) extents (2015-2019) generated by the adapted empirical algorithm over south eastern Greenland (red box; Fig. 1c); and the 2000 m a.s.l. contour (black line), and the 2500 m a.s.l. contour (black dotted line; Howat et al., 2014), overlaid on the 2015 MODIS MOG image map (Haran et al., 2018). (b) The SMAP-derived percolation facies extent is overlaid with AR- and MCoRDS-derived 2010-2017 perennial firn aquifer (blue shading; Miège et al., 2016), 2010-2014 ice slab (cyan shading; MacFerrin et al., 2019), and 2012 spatially coherent melt layer (white shading; Culberg et al., 2021) detections along OIB flight lines (black lines); AR transect A-B (red line; Fig. 3a); and SMAP Test Site A (blue circle; Fig. 4a), and D (red triangle; Fig. 4d).*

Formatted: Centered, Line spacing: single, Pattern: Clear (White)

Formatted: Font: (Default) Arial,

Formatted: Font: 10 pt

Formatted: Space Before: 5 pt

Formatted: Font: 10 pt, Italic

Formatted: Line spacing: 1.5 lines, Pattern: Clear

Formatted: Font: 10 pt, Italic

Formatted: Font: 10 pt, Italic

Formatted: Font: 10 pt, Italic

Formatted: Font: 10 pt, Italic

Formatted: Font: 10 pt, Italic

Formatted: Font: 10 pt, Italic

Formatted: Font: 10 pt, Italic

Formatted: Font: 10 pt, Italic

Formatted: Font: 10 pt, Italic

Formatted: Font: 10 pt, Italic

Formatted: Font: 10 pt, Italic

Formatted: Font: (Default) Arial, Italic,



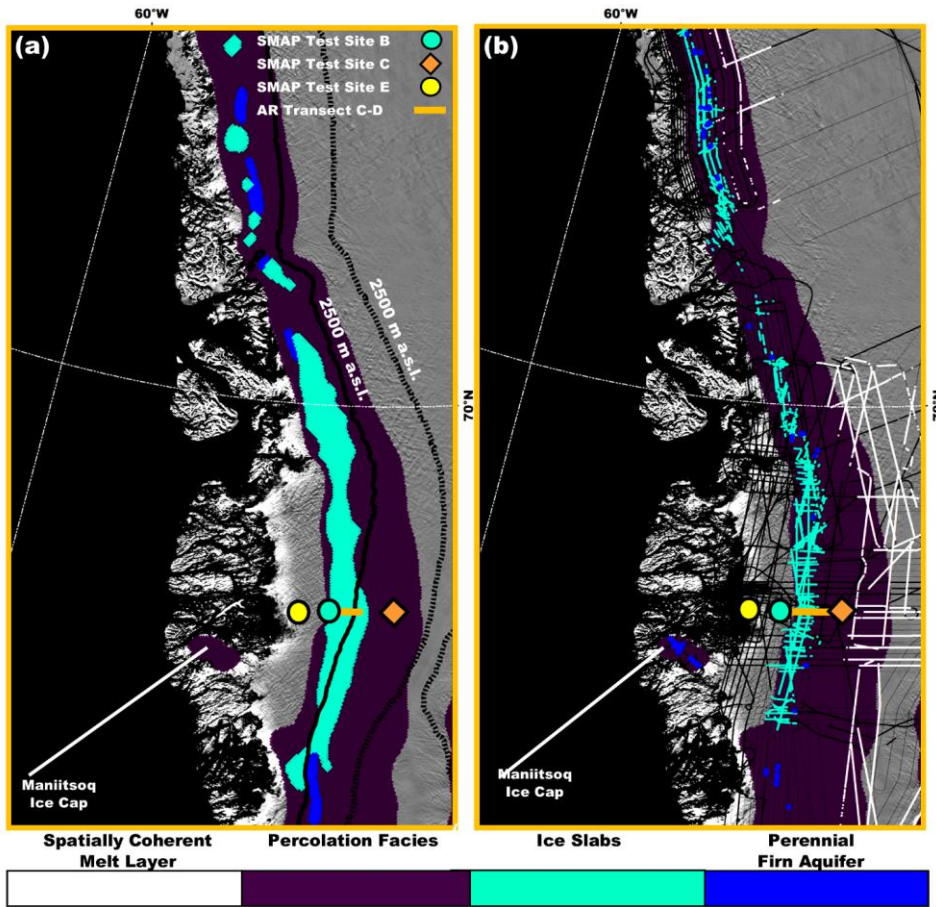


**Figure 9**

(a) SMAP-derived perennial firn aquifer (blue shading), ice slab (cyan shading), and percolation facies (purple shading) extents (2015-2019) generated by the adapted empirical algorithm over south western Greenland (orange box; Fig. 1c); and the 2000 m a.s.l. contour (black line), and the 2500 m a.s.l. contour (black dotted line; Howat et al., 2014) overlaid on the 2015 MODIS MOG image map (Haran et al., 2018). (b) SMAP-derived percolation facies extent is overlaid with AR- and MCoRDS-derived 2010-2017 perennial firn aquifer (blue shading; Miège et al., 2016), 2010-2014 ice slab (cyan shading; MacFerrin et al., 2019), and 2012 spatially coherent melt layer (white shading; Culberg et al., 2021) detections along OIB flight lines (black interior lines); AR transect C-D (orange line; Fig. 3b); and SMAP Test Site B (cyan circle; Fig. 4b), C (orange diamond; Fig. 4c), and E (yellow circle; Fig. 4e).

Formatted: Font: 10 pt

Formatted: Left, Pattern: Clear (White)

Formatted: Font: (Default) Arial, 10 pt.

Formatted: Not Highlight

2073 **Table 1.**  
 2074 *MODIS-derived total number of days in the melting and freezing seasons; SMAP-derived maximum*  
 2075 *vertically-polarized L-band brightness temperature ( $T_{V,max}^B$ ); minimum vertically-polarized L-band brightness*  
 2076 *temperature ( $T_{V,min}^B$ ); time scale scales of exponential decrease following the surface freeze-up date for*  
 2077 *perennial firn aquifer, ice slab, percolation facies, dry snow facies, and wet snow facies areas.*

	<u>Melting Season</u> <u>(days)</u>	<u>Freezing Season</u> <u>(days)</u>	$T_{V,max}^B$ <u>(K)</u>	$T_{V,min}^B$ <u>(K)</u>	<u>Exponential Decrease</u> <u>(time scale)</u>
<u>Perennial</u> <u>Firn Aquifers</u>	75 - 100	265 - 290	200 - 275	180 - 250	weeks - months
<u>Ice</u> <u>Slabs</u>	60 - 90	275 - 305	170 - 260	130 - 240	days - weeks
<u>Percolation</u> <u>Facies</u>	1 - 60	305 - 364	150 - 200	130 - 220	days
<u>Dry Snow</u> <u>Facies</u>	-	365	200 - 240	200 - 240	-
<u>Wet Snow</u> <u>Facies</u>	90 - 120	245 - 275	230 - 250	230 - 250	-

Formatted: Font: 8 pt, Bold

Formatted: Font: 8 pt, Bold

Formatted Table

Formatted: Font: (Default) Arial

Formatted: Font: 8 pt

Formatted: Font: 8 pt

2078



2079  
2080  
2081  
2082  
2083

**Table 23.**

*SMAP-derived calibration parameter threshold-intervals (1 April 2015 - 31 March 2019)-used for mapping perennial firn aquifer and ice slab, and perched firn aquifer extents areas.*

	$\xi$	$T_{V,max}^P$ (K)	$T_{V,min}^P$ (K)	$\zeta$
<u>Perennial Firn Aquifers</u>	<u>0.2 – 4</u>	<u>200 – 275</u>	<u>180 – 250</u>	<u>-0.04 – -0.02</u>
<u>Ice Slabs</u>	<u>0.1 – 2</u>	<u>170 – 260</u>	<u>130 – 240</u>	<u>-0.03 – -0.06</u>
<u>Perched Firn Aquifers</u>	<u>0.2 – 1.2</u>	<u>200 – 260</u>	<u>180 – 240</u>	<u>-0.03 – -0.04</u>

Formatted Table

2084  
2085  
2086

**Table 4.** *The SMAP derived perennial firn aquifer, ice slab, and perched firn aquifer extents (2015-2019) over the percolation facies and the GrIS, and the elevation range at which they are mapped.*

	<u>Percolation Facies Extent</u> (%)	<u>Ice Sheet Extent</u> (%)	<u>Elevation Range</u> (m.a.s.l.)
<u>Perennial Firn Aquifers</u>	<u>11</u>	<u>4</u>	<u>600 – 2600</u>
<u>Ice Slabs</u>	<u>13</u>	<u>4</u>	<u>800 – 2700</u>
<u>Perched Firn Aquifers</u>	<u>5</u>	<u>&lt;1</u>	<u>600 – 2700</u>

- Formatted: Font: 8 pt
- Formatted: Font: 8 pt
- Formatted: Font: 8 pt
- Formatted: Font: 8 pt, Bold
- Formatted: Font: 8 pt
- Formatted: Font: 8 pt
- Formatted: Font: 8 pt, Bold
- Formatted: Font: 8 pt, Bold
- Formatted: Font: 8 pt
- Formatted: Font: 8 pt, Bold
- Formatted: Font: 8 pt
- Formatted: Font: 8 pt
- Formatted: Font: 8 pt
- Formatted: Font: 8 pt
- Formatted: Font: 8 pt

2087

2088  
2089  
2090

**Table 3.**

*Interannual variability in SMAP-derived perennial firn aquifer and ice slab extents.*

	<b>Perennial Firn Aquifers</b>	<b>Ice Slabs</b>
	<b>(km<sup>2</sup>)</b>	<b>(km<sup>2</sup>)</b>
<b>2015-2019</b>	<b>66,000</b>	<b>76,000</b>
<b>2015-2016</b>	<b>63,000</b>	<b>23,000</b>
<b>2016-2017</b>	<b>69,000</b>	<b>48,000</b>
<b>2017-2018</b>	<b>73,000</b>	<b>27,000</b>
<b>2018-2019</b>	<b>70,000</b>	<b>38,000</b>

- Formatted: Font: Italic
- Formatted: Font: Italic
- Formatted: Font: 8 pt
- Formatted Table
- Formatted: Font: 8 pt
- Formatted: Font: 8 pt
- Formatted: Font: 8 pt
- Formatted: Font: 8 pt
- Formatted: Font: 8 pt
- Formatted: Font: Italic
- Formatted: Left, Line spacing: 1.5 lines, Pattern: Clear